NAVIER-STOKES CALCULATIONS OVER SWEPT WINGS

A THESIS SUBMITTED TO
THE GRADUATE SCHOOL OF NATURAL AND APPLIED SCIENCES
OF
MIDDLE EAST TECHNICAL UNIVERSITY

BY

PINAR ŞAHİN

IN PARTIAL FULFILLMENT OF THE REQUIREMENTS FOR

THE DEGREE OF MASTER OF SCIENCE

IN

AEROSPACE ENGINEERING

SEPTEMBER 2006

Approval of the Graduate School of Natural and Applied Sciences

Prof. Dr. Canan ÖZGEN
Director

I certify that this thesis satisfies all the requirements as a thesis for the degree of Master of Science.

Prof. Dr. Nafiz ALEMDAROĞLU
Head of the Department

This is to certify that we have read this thesis and that in our opinion it is fully adequate, in scope and quality, as a thesis for the degree of Master of Science.

Assoc. Prof. Dr. Serkan ÖZGEN
Supervisor

Examining Committee Members:

Prof. Dr. Nafiz ALEMDAROĞLU	(METU, AEE)	
Assoc. Prof. Dr. Serkan ÖZGEN	(METU, AEE)	
Prof. Dr. Zafer DURSUNKAYA	(METU, ME)	
Assoc. Prof. Dr. Sinan EYİ	(METU, AEE)	
Dr. Oğuz UZOL	(METU, AEE)	

I hereby declare that all information in this document has been obtained and presented in accordance with academic rules and ethical conduct. I also declare that, as required by these rules and conduct, I have fully cited and referenced all material and results that are not original to this work.

Pınar ŞAHİN

ABSTRACT

NAVIER-STOKES CALCULATIONS OVER SWEPT WINGS

ŞAHİN, Pınar

M.S., Department of Aerospace Engineering
Supervisor: Assoc. Prof. Dr. Serkan ÖZGEN

September 2006, 83 pages

In this study, the non-equilibrium Johnson and King Turbulence Model (JK model) is implemented in a three-dimensional, Navier-Stokes flow solver. The main program is a structured Euler/Navier-Stokes flow solver in which spatial discretization is accomplished by a finite volume formulation and a multigrid technique is used as a convergence accelerator. The aim is the validation of this in-house developed CFD (Computational Fluid Dynamics) tool with this enhanced enlarged capability in order to obtain a reliable flow solver that can solve flows over swept wings accurately. Various test cases were evaluated against reference solutions in order to demonstrate the accuracy of the newly implemented JK turbulence model. The selected test cases are NACA 0012 airfoil, ONERA M6 wing, DLR-F4 wing and two wings taken from the 3rd Drag Prediction Workshop. The solutions were analyzed and discussed in detail. The results show appreciably good agreement with the experimental data including force coefficients and surface pressure distributions.

Keywords: Swept Wing, Johnson-King Turbulence Model, Finite Volume Formulation, Multigrid Technique.

ÖZ

OK AÇILI KANATLAR ÜZERİNDE NAVIER-STOKES HESAPLAMALARI

ŞAHİN, Pınar
Yüksek Lisans, Havacılık ve Uzay Mühendisliği Bölümü
Tez Yöneticisi : Doç. Dr. Serkan ÖZGEN

Eylül 2006, 83 sayfa

Bu çalışmada, dengede olmayan Johnson ve King Türbülans Modeli, üç boyutlu, Navier-Stokes koduna eklenmiştir. Ana program, yapılı çözüm ağı kullanan uzaysal ayrıştırmanın sonlu hacimler formülasyonuyla yapıldığı ve yakınsamayı hızlandırıcı çoklu çözüm ağı tekniği kullanan Euler/Navier-Stokes akım çözücüsüdür. Amaç, ok açılı kanatlar üzerindeki akışları doğru olarak çözebilecek güvenilir bir akım çözücü elde etmek için bu yeni eklenen yetenekle birlikte ticari olmayan HAD (Hesaplamalı Akışkanlar Dinamiği) aracının doğrulamasının yapılmasıdır. Yeni eklenen türbülans modelinin doğruluğunu göstermek için çeşitli test problemleri referans çözücülere karşı değerlendirilmiştir. Seçilen test problemleri NACA 0012 kanat kesiti, ONERA M6 kanadı, DLR-F4 kanadı ve 3. Sürükleme Tahmin Çalışma Grubundan alınan iki kanattan oluşmaktadır. Çözümler ayrıntılı olarak analiz edilmiş ve tartışılmıştır. Sonuçlar, kuvvet katsayıları ve yüzey basınç dağılımlarını da içeren kapsamlı deneysel verilerle fark edilir derecede iyi uyuşum göstermişlerdir.

Anahtar Kelimeler: Ok Açılı Kanatlar, Johnson-King Türbülans Modeli, Sonlu Hacimler Formülasyonu, Çoklu Çözüm Ağı Tekniği

ACKNOWLEDGEMENTS

I would like first to express my deepest gratitude to my supervisor Assoc. Prof. Dr. S. Özgen for his never ending motivation and guidance. I would also like to thank the rest of my committee, Prof. Dr. N. Alemdaroğlu, Prof. Dr. Z. Dursunkaya, Prof. Dr. S. Eyi, and Dr. O. Uzol. Their contributions are greatly appreciated and are respectfully acknowledged.

I would like to express my sincere gratitude to B. Korkem. A very small amount of his enormous expertise and insight has rubbed off on me, and it is a pleasure to work under his tutelage. I am grateful to my colleagues Y. Ortakaya and E. Tarhan for many enlightening discussions to me pertaining to CFD. I would also like to thank E. Gürdamar for his help, interest and motivation.

I could never have completed this work without unending encouragement and loving support of my dearest friends G. Gözen and B. Karatekin. I am tremendously grateful to my family for believing in me through all my academic pursuits.

I would like to thank TUSAŞ Aerospace Industry Inc. (TAI) for providing hardware support and facilities to research literature.

I extend my appreciation to my friends A. Soysal, M. Yalçın, and Ö. Polat for their support.

This thesis is dedicated to whom I thank.

TABLE OF CONTENTS

LIST OF TABLES

LIST OF FIGURES

LIST OF SYMBOLS

a	Speed of Sound
b	Span
AoA	Angle of Attack
BL	Baldwin-Lomax
CFD	Computational Fluid Dynamics
CFL	Courant-Friedrich-Levy Number
CPU	Central Processing Unit
C_D	Drag Coefficient
C_L	Lift Coefficient
C_P	Pressure Coefficient
D	Dissipative Operator
F	Inviscid Flux Vector
F_v	Viscous Flux Vector
H	Total Enthalpy
l	Mixing Length
JK	Johnson-King
L_m	Dissipation Length Scale
M	Mach Number
N	Node Point
NS	Navier-Stokes
P	Pressure
$\Pr$	Prandtl Number
Re	Reynolds Number
S	Saddle Point
Δt	Time Step
A^+	Streamwise Dependent Pressure Gradient

u_τ	Friction Velocity
y^+	Non-dimensional Wall Distance
Ω	Magnitude of Vorticity
κ	Von Karman Constant
μ	Laminar viscosity
μ_t	Turbulent viscosity
μ_{ti}	Inner Eddy Viscosity
μ_{to}	Outer Eddy Viscosity
η	Spanwise station
δ	Boundary Layer Thickness
ρ	Density
σ	Stress Tensor
$\overline{\sigma}$	Modeling Parameter
γ_K	Klebanoff Intermittency Factor
τ_m	Maximum Reynolds Shear Stress

Subscripts

∞	Free stream
$\max$	Maximum
$Kleb$	Klebanoff
$inner$	Inner Region
$outer$	Outer Region
L	Left State
R	Right State
t	Turbulent
w	Wall
$wake$	Wake

CHAPTER 1

INTRODUCTION

1.1 General Overview

The accurate calculation of separated turbulent compressible flows is a practical need due to its significance in real life applications. The ability to understand, predict, and control these fluid flows are very important especially for aerospace applications. Since flight tests and/or wind tunnel tests can be very time consuming and expensive, the confidence in **C**omputational **F**luid **D**ynamics (CFD) should be improved. Experimental analyses are very effective in getting the information of the surface pressure data at selected points and/or complete lift and drag of the body. However, the detailed pressure and/or velocity information throughout the region surrounding a body is not feasible both in terms of time and cost. In some cases, flight/wind tunnel testing is not possible. Therefore, the computational aerodynamics is preferably used for most of the analysis to gain insight into the nature of these flows.

Thanks to CFD, a model can be investigated faster when compared to any other experimental testing methods, which makes it a valuable aircraft design and analysis tool. Since CFD provides a greater flowfield detail than is possible by experiments alone, it is widely used to complement the experimental investigations.

Validation of the CFD Tool by comparisons wind tunnel data of swept wings, and the implementation of the Johnson and King Turbulence model is the main aim of this thesis. Understanding the flow behavior is particularly cumbersome since the flowfield structure over swept wings, containing the relevant flow physics differ substantially from a conventional wing planform. Analyses of the swept wings are important for most of the aircraft in design process. Flow separation occurs especially at transonic speeds. There is a significant amount of research in this field, which includes particularly swept wings at transonic speeds [1, 2, 3, 4].

1.2 Scope of the Thesis

The purpose of this study is to validate and verify the CFD tool using swept wing test cases. It is known that the aerodynamic characteristics of swept wings are very sensitive to viscous effects, and selection of the turbulence model in numerical codes largely determines the level of success for capturing these effects. A non-equilibrium model, namely the Johnson and King Turbulence Model is implemented to the existing in-house developed flow solver and tested, in order to increase its capability. Besides, the Baldwin-Lomax Turbulence model is already available.

This flow solver will be used to investigate the flow over wings for air vehicle design, in which the extensive aerodynamic data is needed. Continuing advances in CFD provide an attractive means of generating the desired data needed for preliminary and detail design.

Carefully coordinated experiments are needed to validate any CFD tools to improve numerical confidence. In this thesis, swept wing analyses are based upon extensive experimental data sets [1, 5, 6]. Besides, the final test case is taken from the 3^{rd} AIAA Drag Prediction Workshop [7], which provides an opportunity to compare the JK turbulence model results with the results of the other widely known CFD codes.

In this work, the flow fields around the swept wings are computed using xFLOWsvmg. The JK turbulence model results are evaluated and compared against reference solutions. Besides, post-processing of the flowfield is done in terms of surface pressure distributions and surface streamlines.

1.3 Description of Chapters

The structure of this thesis is organized as follows.

In Chapter 2, detailed information about the computational method is given. Governing equations, turbulence modeling, numerical algorithm, computational grids, and numerical boundary conditions are included in this part. This part is followed by a description of test cases and results.

In Chapter 3, test cases and their results are presented. Initially a general overview is given. Then NACA 0012 airfoil, ONERA M6 wing, DLR F4 wing, and wing alone cases taken from the 3^{rd} AIAA Drag Prediction Workshop and their results are investigated. For each test case treated, extensive discussion and evaluation of the results are presented.

In Chapter 4, concluding remarks and future prospects are given.

CHAPTER 2

COMPUTATIONAL METHOD

The present chapter is divided into two main parts. First part describes the grid generation work. Second part describes the solver, which includes the governing equations, turbulence modeling and boundary conditions.

2.1 Grid Generation Description

The computational grid is so called single block C-H type structured grid. The grid wraps as a C mesh around the apex of the wing, whereas it is H-type in the cross-sections. The grids can be generated either externally or using the grid generation module embedded into the code. However, there is a constraint, which is that the dimensions of the grid in each direction should be appropriate to the multigrid level. Since the initial grid is coarsened in each direction by removing alternate points for each multigrid level, the basic rule that has to be followed is that the cell number in each direction has to be a multiple of 2 to the power of the multigrid level.

The automatic hyperbolic grid generator is used, which uses the square root transformation. In this method, Cartesian coordinates are transformed into sheared parabolic coordinates. The wing geometry is provided by a group of x-y coordinates of the airfoil at different constant z span sections. The coordinate axis can be defined as follows: x is in the direction of chord, y is in the direction normal to the chord and span, and z is in the direction of span. After the geometry is given, user should define some parameters in order to control the mesh to be used, such as the number of mesh cells in each direction should be set appropriate to the multigrid level to be applied. Furthermore, some grid clustering parameters should be defined. These are the boundary layer mesh size, grid spacing in y-direction, wing leading/trailing edge and root/tip mesh sizes.

The flow solver can also be used without the multigrid technique. However, multigrid approach provides a faster convergence. Therefore, three levels of multigrid are used for the test cases and the structured type of grids are generated accordingly (Figure 2-1, 2-2, 2-3).

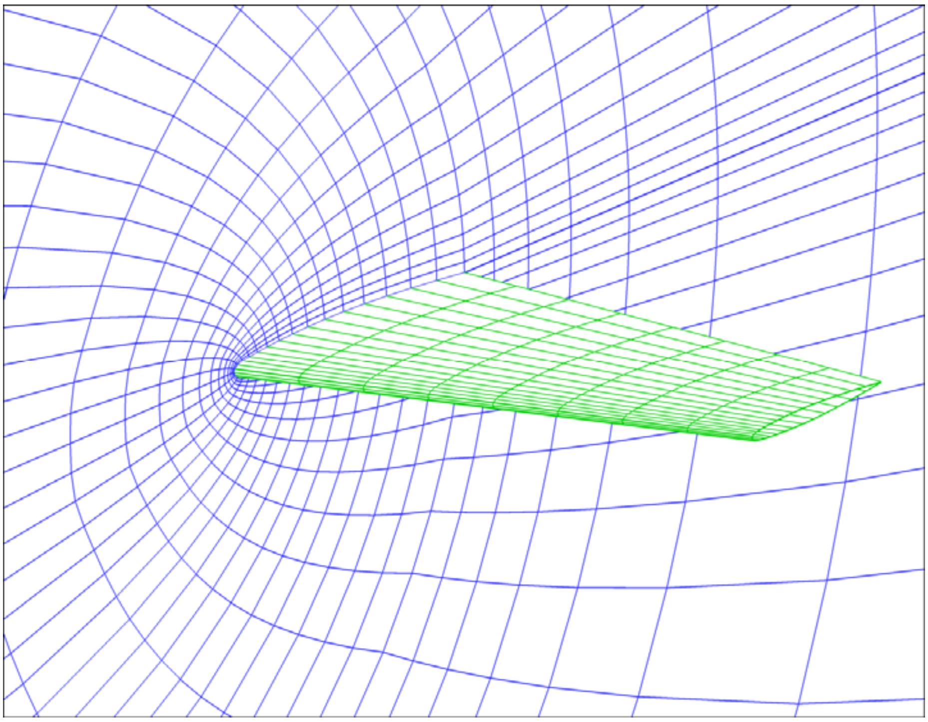

Figure 2-1 Coarse Grid (48x16x12) – Sequence 1 (ONERA M6 Wing)

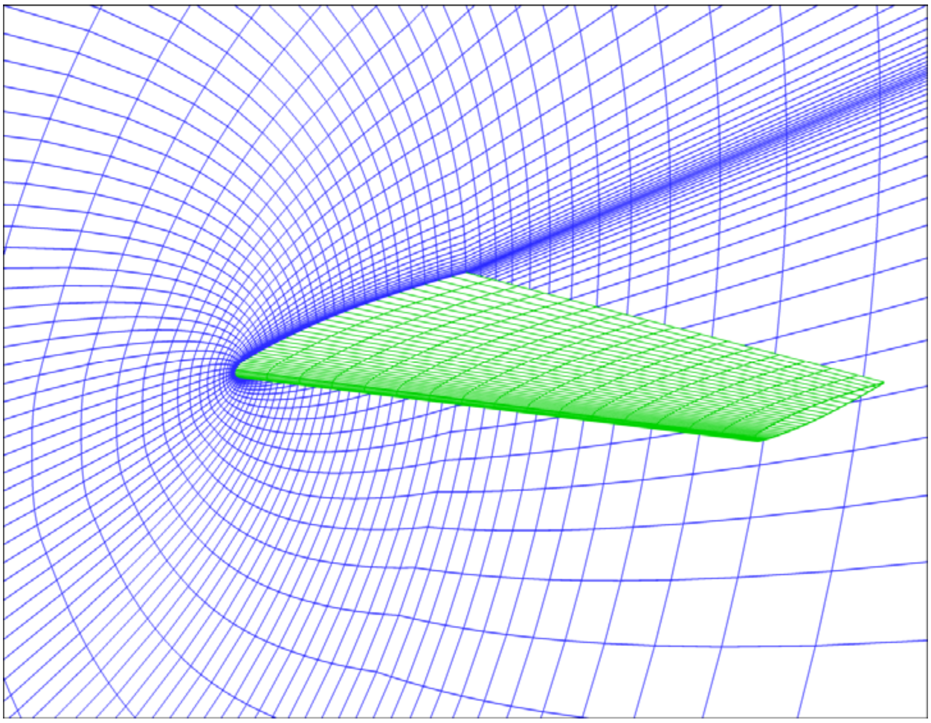

Figure 2-2 Medium Grid (96x32x24) –Sequence 2 (ONERA M6 Wing)

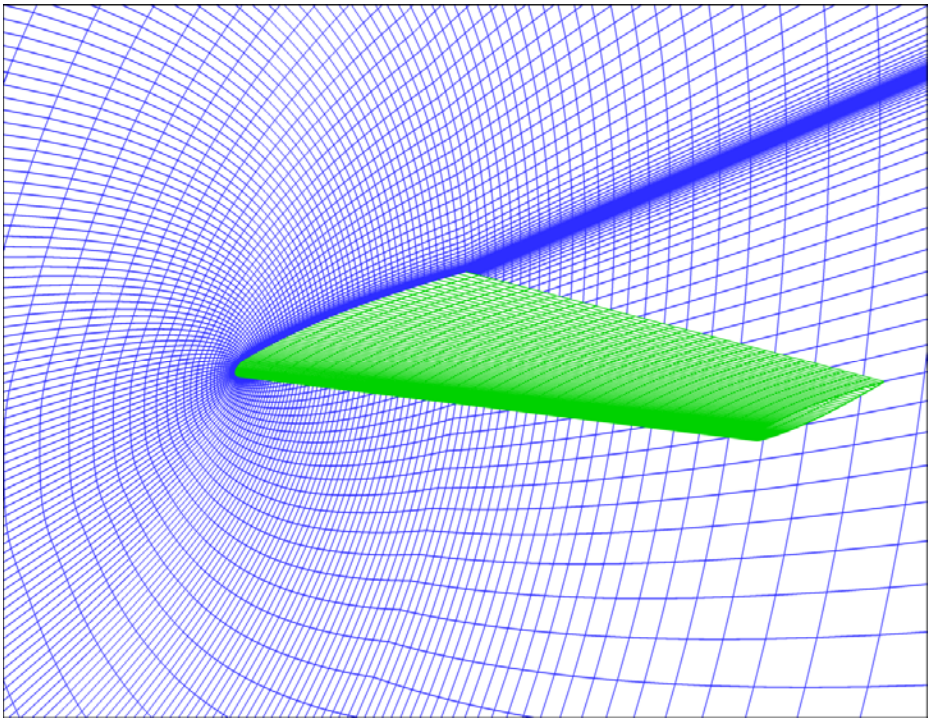

Figure 2-3 Fine Grid (192x64x48) – Sequence 3 (ONERA M6 Wing)

In Figure 2-4 the grid structure and i-, j-, k- directions are demonstrated. The orientation of the coordinate system is as: i-direction wraps the airfoil, j-direction starts from the wing surface and increases towards the far field, and lastly, k-direction is the spanwise direction, which starts at the wing root and increases along the span.

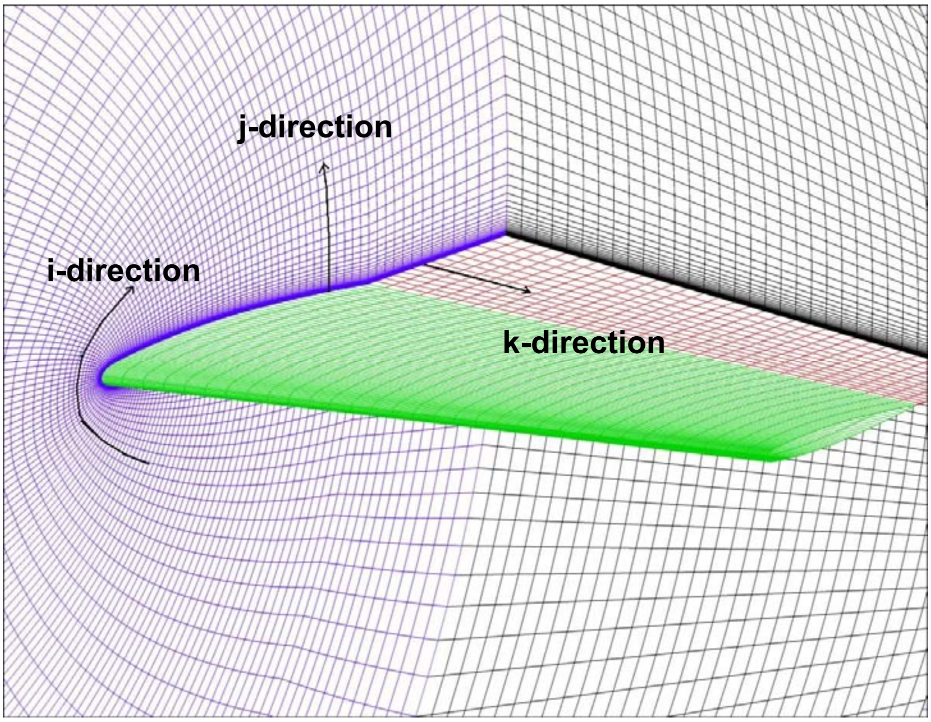

Figure 2-4 3D Grid Structure in Plane of Symmetry (ONERA M6 Wing)

Grid on the surface of the ONERA M6 wing and in the plane of symmetry is shown in Figure 2-3. The structured mesh of 193x65x49 nodes, in the streamwise, spanwise, and the normal direction, is employed. The first grid point of the surface in the normal direction is 1×10^{-4} of the chord length. In Figure 2-5, fine resolution grid around the leading edge is presented. Similar grids are generated for each of the test cases and the pictures are given in Chapter 3.

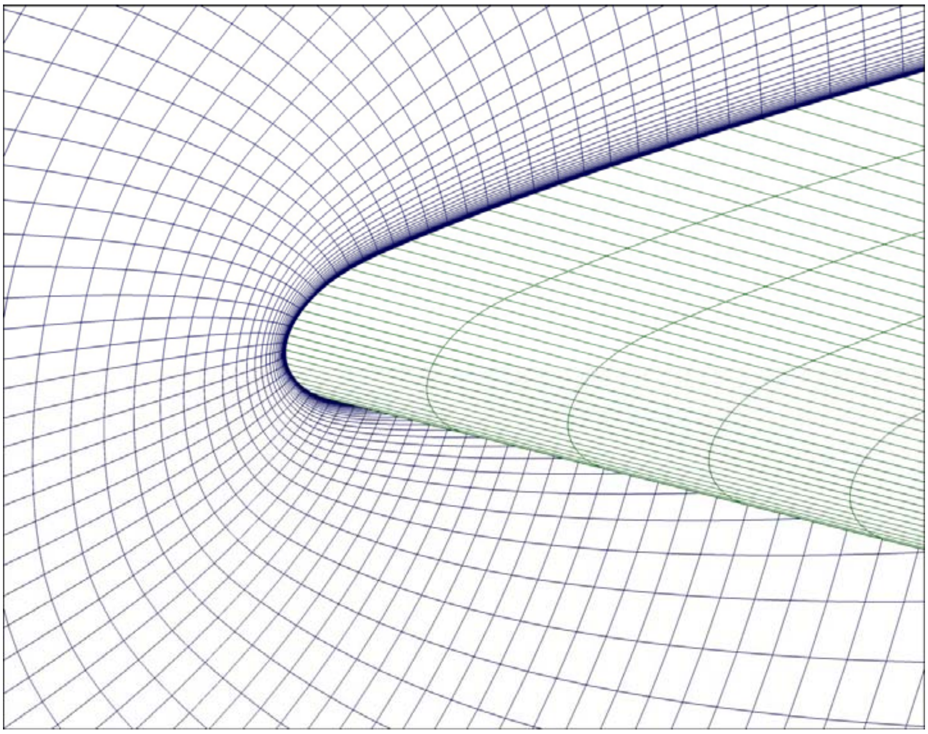

Figure 2-5 Grid Around Leading Edge (ONERA M6 Wing)

2.2 Solver Description

2.2.1 Finite Volume Solver (NS)

The xFLOWsvmg is a finite volume program solving three dimensional Euler/Navier-Stokes equations on structured meshes. Spatial discretization is accomplished by a cell-vertex formulation, in which the control volume for each interior vertex is the union of the eight cells surrounding that vertex. The flux through each side of the control volume is calculated using the values of the flow variables at the center point only. This allows the cancellation of downstream contributions to the fluxes by the diffusive terms, which are calculated from differences along the coordinate lines.

The solution advances using multigrid scheme providing accelerated convergence. The initial grid is coarsened for each multigrid level and the calculations are performed and then the solution continues with proper interpolation.

Turbulence is modeled by the algebraic Baldwin-Lomax [10] and newly implemented Johnson and King Turbulence models [11]. The solution advances in time using a fifth order Runge-Kutta time-stepping scheme with implicit residual smoothing and local time stepping capabilities.

2.2.2 Governing Equations

An integral form of the governing Euler/Navier-Stokes equations for the flow of a compressible gas is as given in the following equation,

$$\frac{\partial}{\partial t}\iiint_{\Omega} w d\Omega + \iint_{S} \vec{F} \bullet d\vec{S} - \iint_{S} \vec{F}_v \bullet d\vec{S} = 0 \qquad (2.1)$$

where, w is the vector for the flow variables in the conservative form, Ω is the control volume element with boundary defined by S. The inviscid and viscous flux vectors are $\vec{F}$ and $\vec{F}_v$, respectively. Note that, $\vec{F}_v = 0$ for Euler equations.

$$w = \begin{bmatrix} \rho \\ \rho u \\ \rho v \\ \rho w \\ \rho E \end{bmatrix} \quad F_i = \begin{bmatrix} \rho u_i \\ \rho u u_i + p\delta_{i1} \\ \rho v u_i + p\delta_{i2} \\ \rho w u_i + p\delta_{i3} \\ \rho H u_i \end{bmatrix} \quad F_{vi} = \begin{bmatrix} 0 \\ \sigma_{ij}\delta_{j1} \\ \sigma_{ij}\delta_{j2} \\ \sigma_{ij}\delta_{j3} \\ u_j\sigma_{ij} + k\dfrac{\partial T}{\partial x_i} \end{bmatrix} \qquad (2.2)$$

For mass conservation,

$$w = \rho \, , \; \vec{F} = (\rho u, \rho v, \rho w) \tag{2.3}$$

For momentum conservation in x-, y- and z-directions,

$$\begin{aligned}
&w = \rho u \, , \; \vec{F} = \left(\rho u^2 + p, \rho uv, \rho uw\right), \; \vec{F}_v = \left(\sigma_{xx} + \sigma_{xy} + \sigma_{xz}\right) \\
&w = \rho v \, , \; \vec{F} = \left(\rho vu, \rho v^2 + p, \rho vw\right), \; \vec{F}_v = \left(\sigma_{yx} + \sigma_{yy} + \sigma_{yz}\right) \\
&w = \rho w \, , \; \vec{F} = \left(\rho wu, \rho wv, \rho w^2 + p\right), \; \vec{F}_v = \left(\sigma_{zx} + \sigma_{zy} + \sigma_{zz}\right)
\end{aligned} \tag{2.4}$$

where σ_{ij} is the stress tensor which is proportional to strain rate tensor and bulk dilatation,

$$\sigma_{ij} = \mu\left(\frac{\partial u_i}{\partial x_j} + \frac{\partial u_j}{\partial x_i}\right) + \lambda \delta ij \frac{\partial u_k}{\partial x_k} \tag{2.5}$$

and μ and λ are the coefficient of viscosity and bulk viscosity respectively. Using the Stokes' hypothesis λ is taken as,

$$\lambda = -\frac{2}{3}\mu \tag{2.6}$$

For the energy conservation equation,

$$w = \rho E \, , \; \vec{F} = (\rho Hu, \rho Hv, \rho Hw) \tag{2.7}$$

where *E* is the total energy and *H* is the total enthalpy. For a prefect gas the following relation for E is used:

$$E = \frac{P}{\rho(\gamma - 1)} + \frac{1}{2}V^2$$

$$V = \sqrt{u^2 + v^2 + w^2} \tag{2.8}$$

$$H = E + \frac{P}{\rho}$$

Above definitions, P is used for pressure, ρ is for density; u, v and w are the velocity components in an orthogonal coordinate system with x, y and z coordinate axis.

The Euler equations are a simpler version of the Navier-Stokes equations being the system of inviscid conservation laws. Its physical basis is the expression of the mass, momentum and energy conservation laws and from a mathematical point of view, the viscous flux vectors (diffusive terms) are ignored in Euler equations.

Finite volume with cell-vertex scheme approach is used for the evaluation of integrals for a hexahedron control volume element for which Equation (2.1) assumes the following form:

$$\frac{d}{dt}(wVol) + Q(w) = 0 \tag{2.9}$$

where *Q* denotes the operator for approximation to the boundary integrals over S of the control volume element Ω whose volume is represented by *Vol* and where the flux balance is carried out.

It is necessary to augment the finite volume scheme with the addition of dissipation terms to prevent the appearance of wiggles in regions near the high pressure gradients such as shock waves or stagnation points. With the addition of dissipative terms, the Equation (2.9) is replaced by the following, where *D* stands for the dissipative operator.

$$\frac{d}{dt}\left(wVol\right)+Q(w)-D(w)=0 \qquad (2.10)$$

In order to design the scheme to have high accuracy in smooth regions of the flow field, well resolved shock waves and contact discontinuities, Jameson's "Symmetric Limited Positive (SLIP) Scheme" [8] is applied. In this scheme, a third order artificial dissipation term is modified by inserting limiters. Since the limiters tend to reduce the accuracy of the solutions, particularly in regions containing smooth extrema [9], an alternative formulation is used by forming the diffusive fluxes from left and right states at the cell interface. According to the Jameson's base limiter function,

$$R(u,v)=1-\left|\frac{u-v}{|u|+|v|+\varepsilon}\right|^{q} \qquad (2.11)$$

where *u* and *v* here represents the differences for each flow variable at right and left states of the cell interface and *q* is an integer. $R(u,v)\approx 0$ when *u* and *v* have the opposite sign in the neighborhood of shock waves resulting first order scheme for the artificial viscosity and $R(u,v)=1$ in the smooth flow regions resulting in third order accuracy [9]. In the scheme, the following form of the limiter function is applied for each flow variable;

$$L(u,v) = R(u,v)\frac{u+v}{2} \tag{2.12}$$

Therefore limiting of each dependent variable in each coordinate direction is enhanced [9].

Left and right states for each dependent variable are separately defined.

$$\begin{aligned}
w_L &= w_{j-1} + \frac{1}{2}L\left(\Delta w_{j+1/2}, \Delta w_{j-3/2}\right) \\
w_R &= w_j - \frac{1}{2}L\left(\Delta w_{j+1/2}, \Delta w_{j-3/2}\right) \\
\Delta w_{j+1/2} &= w_{j+1} - w_j
\end{aligned} \tag{2.13}$$

The flux terms are obtained by the following;

$$w_R - w_L = w_{j-1/2} - \frac{1}{2}L\left(\Delta w_{j+1/2}, \Delta w_{j-3/2}\right) \tag{2.14}$$

Left and right state pressure (P_L and P_R) terms are evaluated by using the w_R and w_L definitions. Also, in order to preserve the total enthalpy, energy terms are replaced by the definition of total enthalpy, which is the equation of H in Equation (2.8).

For the time integration of the linear system given by the Equation (2.15), multi-stage Runge-Kutta method is applied.

$$\frac{dw}{dt} + R(w) = 0$$

$$R(w) = Q(w) + D(w) \qquad (2.15)$$

w represents the vector of flow variables at the mesh points and $R(w)$ is the vector of the residuals. The residual is split as given in Equation (2.15) with the convective and dissipative terms. Let w^n be the result after n steps. To advance one step Δt with an k-stage it is set as;

$$\begin{aligned} & w^{(n+1,0)} = w^n \\ & .... \\ & w^{(n+1,k)} = w^{(n)} - \alpha_k \Delta t\left(Q^{(k-1)} + D^{(k-1)}\right) \\ & .... \\ & w^{(n+1)} = w^{(n+1,m)} \end{aligned} \qquad (2.16)$$

where the superscript k denotes the k-th stage, $\alpha_m = 1$, and,

$$\begin{aligned} & Q^{(0)} = Q(w^n), D^{(0)} = D(w^n) \\ & ..... \\ & Q^{(k)} = Q(w^{(n+1,k)}) \\ & D^{(k)} = \beta_k D(w^{(n+1,k)}) + (1-\beta_k) D^{(k-1)} \end{aligned} \qquad (2.17)$$

The coefficients α_k are chosen to maximize the stability interval along the imaginary axis, and the coefficients β_k are chosen to increase the stability interval along the negative real axis [8]. These coefficients for the five-stage scheme with three evaluations of dissipation are given in Equation (2.18).

$$\begin{aligned} & \alpha_1 = 1/4 && \beta_1 = 1 \\ & \alpha_2 = 1/6 && \beta_2 = 0 \\ & \alpha_3 = 3/8 && \beta_3 = 0.56 \\ & \alpha_4 = 1/2 && \beta_4 = 0 \\ & \alpha_5 = 1 && \beta_5 = 0.44 \end{aligned} \qquad (2.18)$$

For the computations of test cases, this five-stage scheme is employed. Convergence to the steady state is accelerated by using variable time step close to the stability limits for each mesh point. Also, utilizing the residual averaging, the scheme is further accelerated. The residual smoothing is a technique in which the residuals are implicitly averaged in order to increase the stability limit of the discretized equations and enable the use of larger time steps or larger CFL number.

Local time stepping and implicit residual smoothing techniques are employed in order to accelerate convergence to steady state. All cells do not march in time to steady state at the same rate. For viscous flows, the time step is smaller in the boundary layer compared to the farfield. The idea of local time stepping is to advance the equations at each grid point by the maximum permissible time step at that point, which ensures stability as calculated from local grid and flow properties. Therefore, the local time step is made function of the local velocity, speed of sound and cell characteristic length, multiplied by the CFL number, shown in Equation (2.19) .

$$\Delta t = CFL \cdot \Delta t_{stab} \qquad (2.19)$$

Residual smoothing is a technique whereby residuals are implicitly averaged in order to increase the stability limit of the discretized equations, and thus enable the use of larger time steps, or larger values of CFL number. Implicit residual smoothing operation, with a standard second-difference operator, is performed at each Runge-Kutta stage k.

The multigrid technique is employed to accelerate the convergence of the flow solver. The level of the multigrid determines the number of grid coarsening cycle. The cell numbers in i-, j-, and k- directions have to be appropriate with the multigrid cycle. The underlying idea of a multigrid time stepping scheme is to transfer some of the task tracking the evaluation of the system to a sequence of coarser meshes. The advantage of this is that, the computational effort per time step is reduced on coarser mesh. The whole set of grids is traversed in which time steps are only performed when moving down the cycle. First order numerical diffusion is always used on the coarser grids and in cases when characteristic splitting is used on the fine grid, simple scalar diffusion is used on the coarser grids.

For the solution of Euler equations and in the absence of shock waves, a forcing term proportional to the difference between the total enthalpy and its freestream value H_∞ is introduced for the convergence acceleration.

2.2.3 Turbulence Modeling

In real life, it is very difficult to determine the turbulent motion of the fluid flow. Physical considerations and statistical approaches continue on turbulent flows. Also, there are numerous turbulence models trying to make the life easier by making some approximations for these flows. From an engineering point of view, turbulence is a significant phenomenon for many flows. Therefore, engineers need computational procedures which can supply adequate information about these flows. A turbulence model is a semi-empirical equation relating the fluctuating correlation to mean flow variables with various constants provided from experimental investigations [12]. It is used to understand the behaviour of the turbulent flows with a sufficient accuracy and generality. The turbulence models can be analyzed in four different groups which are zero-equation, one-equation, two-equation and half equation models.

If a turbulence model is described by algebraic equations alone, then it is a zero-equation model. The advantage of this is that, it is easy to adapt to a Navier-Stokes code and fast to solve. The other type is the half equation model, when the turbulence model is reduced to an ordinary differential equation. The half-equation model is known as an interesting replacement for algebraic models for separated flows. Because it improves the agreement between computed and measured flow properties.

The main task of the thesis is to adapt the non-equilibrium type of Johnson-King model into the existing flow solver so as to solve the aerodynamic flows of interest. Besides, the Baldwin-Lomax turbulence model is already available in the current solver. With these turbulence models, the solution time is shorter with faster convergence and the results are convenient, which yield favorable results in three dimensional aerodynamic flows.

There has been always lots of activity to surpass the standards set by algebraic models with newer ones. In the analysis of aerodynamic flows the most notable ones are the Johnson-King model, the one-equation model proposed by Spalart-Allmaras and the $k-\omega$ two-equation model. In the following parts, the governing equations of the JK and BL models are given. The BL model is also used as a baseline model in JK calculations. In addition to this, their references to the original publications are given for the precise meaning of all the terms and details related to implementation are also granted. Since at each time step, the equation for the turbulent viscosity is solved separately from the flow equations, resulting in a loosely coupled solution process which allows interchange of new turbulence models to be made easily.

2.2.3.1 The Baldwin-Lomax Model

This model contains the algebraic relations between the fluctuating components and the mean flow values. In zero equation models, though the local rate of turbulence is equal to the rate of dissipation of turbulence, since the convection of turbulence is not considered, it is not a physically correct description of the turbulent flow. On the other hand, undoubtedly it is the easiest turbulence model type to apply and fast to solve. The Baldwin-Lomax model is one of the important and popular algebraic turbulence models. The turbulent boundary layer is considered to be formed by two regions, an inner and an outer region, with different expressions for the eddy viscosity coefficient. The distinguishing property of the model is that the model is not written in terms of the boundary layer quantities. The Baldwin-Lomax model establishes the outer layer length scale in terms of the vorticity in the layer.

The term in the equations of motion that is to be modeled is the eddy viscosity coefficient, μ_t. Thereby, the molecular coefficient, μ in the stress terms of the Navier-Stokes equations is replaced by $\mu + \mu_t$. The Baldwin-Lomax [10] model is the two layer algebraic eddy viscosity model in which the turbulent viscosity is given by,

$$\mu_t = \begin{cases} (\mu_t)_{inner} \; y \le y_{crossover} \\ (\mu_t)_{outer} \; y \ge y_{crossover} \end{cases} \tag{2.20}$$

where y is the normal distance from the wall and $y_{crossover}$ is the smallest value of y at which values from the inner and outer formulas are equal. In the inner region, the model utilizes the exponential function and for the outer region it is proportional to the boundary layer thickness. The inner region is defined by the Prandtl-Van Driest formulation in Equation (2.21).

$$(\mu_t)_{inner} = \rho l^2 \Omega \qquad (2.21)$$

The term l is the mixing-length (Van Driest function) and it is formulated in Equation (2.22) using the non-dimensional wall distance y^+, the Von-Karman Constant $\kappa = 0.4$ and the streamwise dependent pressure gradient A^+, which is nearly 26 for zero pressure gradient.

$$l = \kappa y\left[1 - \exp\left(-y^+ / A^+\right)\right] \qquad (2.22)$$

The magnitude of the vorticity, Ω and the non-dimensional wall distance y^+ are,

$$\Omega = \sqrt{\left(\frac{\partial u}{\partial y} - \frac{\partial v}{\partial x}\right)^2 + \left(\frac{\partial v}{\partial z} - \frac{\partial w}{\partial y}\right)^2 + \left(\frac{\partial w}{\partial x} - \frac{\partial u}{\partial z}\right)^2}$$

$$y^+ = \frac{\rho_w u_\tau y}{\mu_w} = \frac{\sqrt{\rho_w \tau_w}\, y}{\mu_w} \qquad (2.23)$$

The friction velocity is defined as $u_\tau = \sqrt{\tau_w / \rho_w}$ and the subscript 'w' denotes the 'wall' quantities. The eddy viscosity in the outer region is formulated as follows,

$$(\mu_t)_{outer} = K C_{CP} \rho F_{wake} F_{Kleb}(y) \qquad (2.24)$$

The constants of above formula are $C_{CP} = 1.6$ and the Clauser constant, $K = 0.0168$. The wake parameter is determined from the Equation (2.25), in which the constant $C_{WK} = 1.0$.

$$F_{wake} = \min\begin{cases} y_{\max} F_{\max} \\ C_{WK}\, y_{\max} u_{diff}^{2} / F_{\max} \end{cases} \tag{2.25}$$

The maximum value of F and y are calculated from the function $F(y)$, refer to the Equation (2.26), by setting the exponential term equal to zero.

$$F(y) = y\Omega\left(1 - \exp(-y^{+} / A^{+})\right) \tag{2.26}$$

Using the $y_{\max}$ value and the Klebanoff intermittency factor, $\gamma_k = 0.3$, the function $F_{Kleb}(y)$ is calculated in Equation (2.27).

$$F_{Kleb}(y) = \left[1 + 5.5\left(\frac{\gamma_k y}{y_{\max}}\right)^{6}\right]^{-1} \tag{2.27}$$

The maximum velocity and the minimum velocity (which is zero except in the wake) are calculated, then their difference is computed to determine the value of u_{diff} in Equation (2.28).

$$u_{diff} = (u_{total})_{\max} - (u_{total})_{\min} \tag{2.28}$$

For more details see [10]. After doing all these calculation, these turbulence effects are added into Navier-Stokes equations via replacing the molecular viscosity coefficient in the stress terms with the total of the eddy viscosity and molecular viscosity coefficients. The heat flux term is also replaced in the energy Equation (2.29).

$$\frac{k}{c_p} = \frac{\mu}{\mathrm{Pr}} \Rightarrow \frac{k}{c_p} = \frac{\mu}{\mathrm{Pr}} + \frac{\mu_t}{\mathrm{Pr}_t} \tag{2.29}$$

where Pr is the Prandtl number and taken as a constant; $\mathrm{Pr} = 0.725$ and $\mathrm{Pr}_t = 0.9$. This model is appropriate for the structured grid, and extensively used for thin, attached, shear layers at moderate Mach numbers with very acceptable results. However, it is not able to take into account the transport and diffusion of turbulence and thus history effects can not be simulated. This deficiency will mainly appear in complex flow configurations, such as separated flows.

2.2.3.2 The Johnson-King Model

The starting point of the half-equation model is a so called ‘equilibrium’ algebraic model. The most powerful part of the Johnson-King turbulence model is that, it offers a promising modification that removes much of the inadequacy of algebraic models for separated flows. In this study, the non-equilibrium type of Johnson-King model [11] is implemented into three-dimensional Navier-Stokes flow solver. Turbulence transport the history, therefore it is not a local phenomena. In order to obtain more realistic results, the convection of turbulence should be added in eddies while modeling turbulence. In this model the history effects of turbulence are modeled for maximum Reynolds shear stress via solving a partial differential equation. Then the eddy viscosity of the model is scaled using this maximum.

"Algebraic turbulence models are not suitable for separated flows, because these models assume that the turbulent production and dissipation rates are locally in balance. To capture the correct physics of separated flow, non-equilibrium effects such as convection and diffusion for turbulence have to be taken into account", [11]. The turbulent eddy viscosity in the Johnson-King model is,

$$\mu_t = \mu_{to}\left[1 - \exp\left(-\mu_{ti} / \mu_{to}\right)\right] \quad (2.30)$$

μ_{ti} is the inner viscosity which is defined as follows,

$$\mu_{ti} = \rho D^2 \kappa N \sqrt{\tau_m} \quad (2.31)$$

The von Karman constant is $\kappa = 0.4$. τ_m is the maximum Reynolds shear stress and is derived from the turbulent kinetic energy in the form of partial differential equation [16]. N is the local normal distance from the wall. The damping factor, D is formulated in Equation (2.32).

$$D = 1 - \exp\left(-\rho_w N u_\tau / \mu_w A^+\right) \quad (2.32)$$

where, $A^+ = 17$ and the conventional friction velocity u_τ is given by the Equation (2.33).

$$u_\tau = \max\left(\frac{\tau_m}{\rho_m}, \frac{\tau_w}{\rho_w}\right) \tag{2.33}$$

τ_w is the wall shear stress, τ_m is invariant to the coordinate system and will be calculated later on. The Reynolds shear stress is defined as,

$$\tau = \frac{\mu_t \Omega}{\rho} \tag{2.34}$$

where Ω is the magnitude of the vorticity. The Baldwin-Lomax wake model is used to determine the outer eddy viscosity (Equation (2.35)). Here, the 'non-equilibrium' feature of the model comes in through the appearance of a 'non-equilibrium (or modeling) parameter', $\bar{\sigma}$.

$$\mu_{to} = \bar{\sigma}\rho K C_c F_w \gamma_k \tag{2.35}$$

The constants are the Clauser constant, $K = 0.0168$ and $C_c = 1.6$. $F_w = N_{\max} F_{\max}$, and $F_{\max}$ is determined from the function Equation (2.36) by locating the N value where $F(N)$ is a maximum.

$$F(N) = N\Omega D \tag{2.36}$$

In the separated flow, there is usually more than one peak. Therefore, the farthest peak away from the wall should be chosen [11]. The Klebanoff intermittency factor (Equation (2.37)) takes care of the intermittency effects.

$$\gamma_k = \left[1 + 5.5(N/\delta)^6\right]^{-1} \tag{2.37}$$

The modeling parameter $\bar{\sigma}$ provides a relation between the assumed eddy viscosity distribution and the rate equation for the streamwise development of the maximum Reynolds shear stress. According to the Equation (2.38), $\bar{\sigma}$ is updated at each time level.

$$\bar{\sigma}^{t+dt} = \bar{\sigma}^{t} \frac{\rho_{\max}\tau_m}{(\mu\Omega)_{\max}} \tag{2.38}$$

The rate equation, mentioned above, is given in the following Equation (2.39),

$$\frac{\partial \tau_m}{\partial t} + u_m \frac{\partial \tau_m}{\partial x} + v_m \frac{\partial \tau_m}{\partial y} + w_m \frac{\partial \tau_m}{\partial z} = \frac{a_1}{L_m}\tau_m\left[(\tau_{m,eq}{}^{1/2} - \tau_m{}^{1/2})\right] - a_1 D_m \tag{2.39}$$

where the dissipation length scale, L_m is defined in Equation (2.40).

$$L_m = \min\left(0.4N_m, 0.09\delta\right) \tag{2.40}$$

The boundary layer thickness, $\delta = 1.9N_{\max}$. The subscript 'eq' denotes the equilibrium condition, in which the modeling parameter $\bar{\sigma}$ equal to unity. D_m is the turbulent diffusion term given in Equation (2.41) and $\tau_{m,eq}$ is the resultant maximum Reynolds shear stress when convection and diffusion effects are small.

$$D_m = \frac{C_D \tau_m^{3/2} \left| 1 - \overline{\sigma}^{1/2} \right|}{a_1 \left[0.7\delta - N_m \right]} \quad (2.41)$$

The constants of the above equation are $a_1 = 0.25$ and $C_D = 0.5$. The turbulent diffusion term has a negligible effect when the modeling parameter $\overline{\sigma}$ is less than unity. Therefore, initial runs obtained from the equilibrium model are required. In this thesis, Baldwin-Lomax is used to obtain initial steady state solutions at two cycles of the multigrid. It is also possible to activate the Johnson-King model at the second cycle, but this increases the runtime noticeably. Therefore the JK model is activated at the last cycle, which solves the finest grid. At each time advance, the maximum shear stresses are determined and then modeling parameter is updated at the next time level.

2.2.4 Boundary Conditions

Improper treatment of the boundary conditions can lead to serious errors and perhaps instability. In the present computations, flow tangency or no-slip boundary condition is applied at the wing surface according to the inviscid or viscous flows as represented in Equation (2.42).

$$\begin{aligned} &\vec{V} \cdot \vec{n} = 0 \ \text{(flow tangency condition)} \\ &V\big|_{y=wall} = 0 \ \text{(no-slip condition)} \end{aligned} \quad (2.42)$$

Density and pressure is calculated on the surface by utilizing the ghost cells in where the pressure and density is extrapolated using the one step lagging values on the wall and neighbor cells. In the following Equation (2.43), the variable X represents either density, pressure or the velocities, u, v, w. At the wake cut planes, the flow variables are averaged using the values of first upper and lower cells at the two sides of the plane.

$$X_i^{n+1} = 2X_{i-1}^{n} - X_{i-2}^{n-1} \qquad (2.43)$$

For the farfield boundary plane, characteristic type of boundary condition is applied using the one dimensional Riemann invariants, where R^+ is associated with $u+a$ and R^- is associated with $u-a$.

$$R^{\pm} = V \pm \frac{2a}{\gamma - 1} \qquad (2.44)$$

CHAPTER 3

RESULTS AND DISCUSSIONS

3.1 General Overview

In this chapter, investigation of four different test cases is discussed. The results and discussions presented here are also used to compare and evaluate the performance of Johnson-King turbulence model for selected flow fields. Three dimensional compressible Euler/Navier-Stokes flow solver is used for these numerical computations. The convergence of the initial solutions is accelerated with mesh sequencing and multigrid. Subsequent solutions are restarted from a related solution.

The grids generated for all test cases are similar. The automatic hyperbolic grid generator is used which is embedded into the flow solver. Initially, wing geometries are analytically defined. Then some parameters, such as the number of mesh cells in each direction, boundary layer mesh size, etc., are defined. For all test cases, structured, C-H type and composed of 193x65x49 points, grids are generated.

Results presented here is computed on PC (Intel Pentium 4CPU 2.80 GHz, 1GB of RAM). The flow solver is iterated on the solution until a certain convergence criteria is met. In general, the convergence criteria may depend on the conditions of the flow solution. For the following test cases, it is desired to reduce the residuals by 3 or 4 orders, which is typical for steady state calculations. Besides, the convergence of force coefficients is also observed.

Tecplot tool is used for the post processing. This step is crucial in the inspection of the unanticipated flow feature or the grid defects. In addition, all of the analysis pictures, including grids, pressure contours and force coefficients, are prepared using Tecplot.

3.2 Test Case I: NACA 0012 Airfoil

NACA 0012 is selected as a first test case in order to show the accuracy and convergence for the implemented algorithm of the Johnson-King turbulence model. The experimental data belongs to the airfoil, which is two dimensional. But, the flow solver is three dimensional. Therefore, a constant cross-section wing model of large aspect ratio, which is 20, is generated. The experimental data available for the airfoil was obtained with a similar geometry in the Langley 8-foot transonic pressure tunnel [5]. The employed grid for present calculations is C-H type and composed of 193x65x49 points. Investigations are performed on the slice extracted from the mid-span of the wing (see Figure 3-1). The surface pressure distribution calculated on this slice is compared with the experimental results.

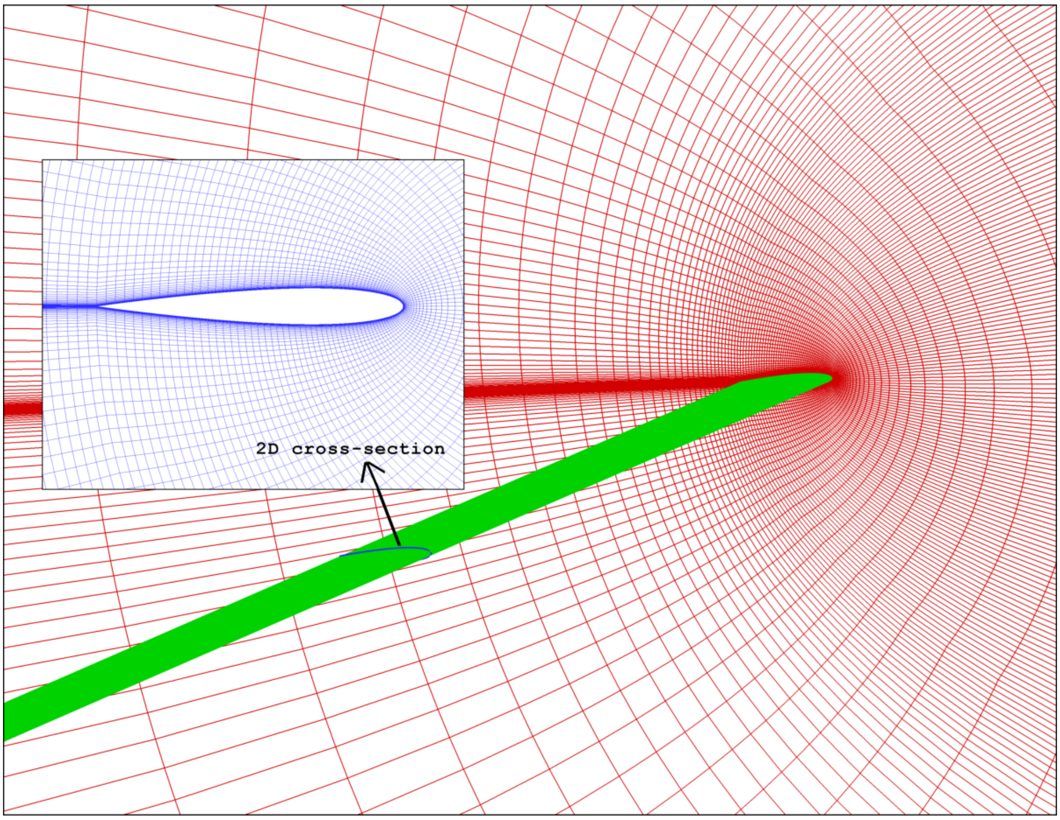

Figure 3-1   Mesh around the NACA 0012 airfoil

Two separate flow conditions are considered. These are, M_∞ = 0.702, α=1.49 degrees, and M_∞ = 0.799, α=2.26 degrees, both cases with Re=6x10^6. Calculations were performed using three-level multigrid scheme.

In Figure 3-2, the convergence characteristics of the NS solver for the first problem (M=0.702, α=1.49 deg.) with the log of the residual and lift/drag are shown. The 3 levels of mesh sequencing are shown: 250 coarse-grid iterations, 250 medium level iterations, and 500 fine grid iterations. The residual drops approximately 5 orders of magnitude. This solution took just under 2 hours (wall time) on PC (Intel Pentium 4CPU 2.80 GHz, 1GB of RAM).

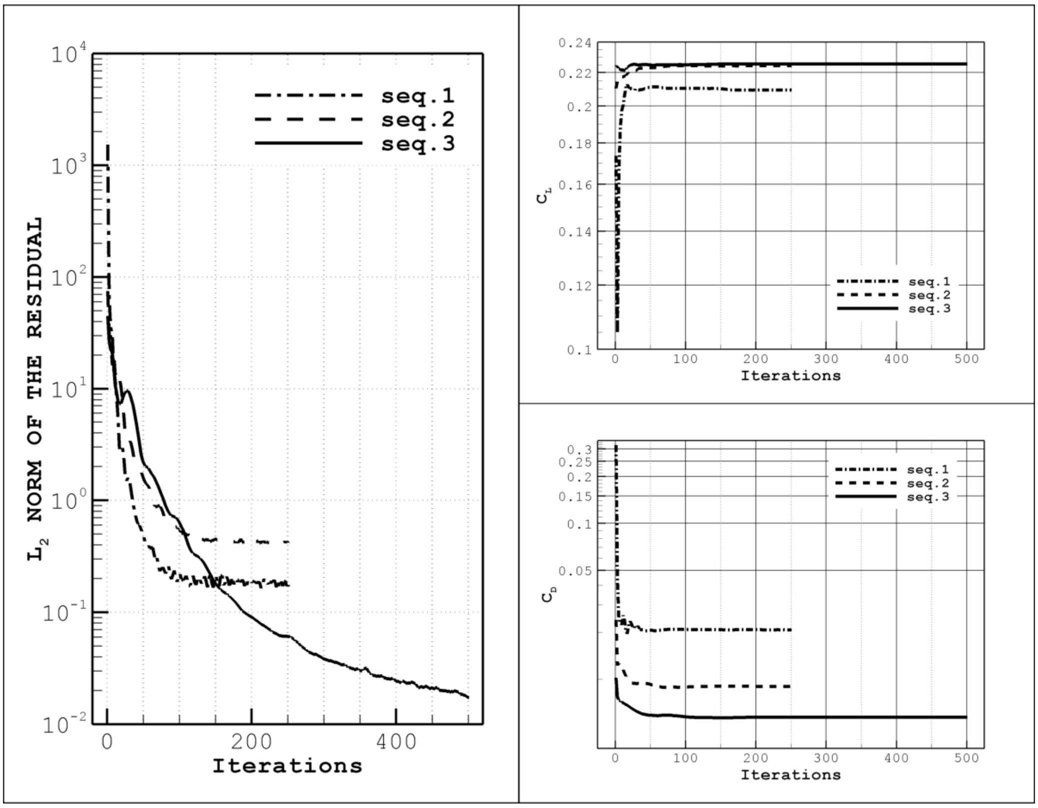

Figure 3-2 Convergence Histories of NACA 0012 airfoil (M_∞=0.702, α=1.49^o)

The solutions of the JK computation are presented with surface pressure contours in Figure 3-3. Following this figure, both inviscid and viscous numerical results are compared against the experimental data (Figure 3-4).

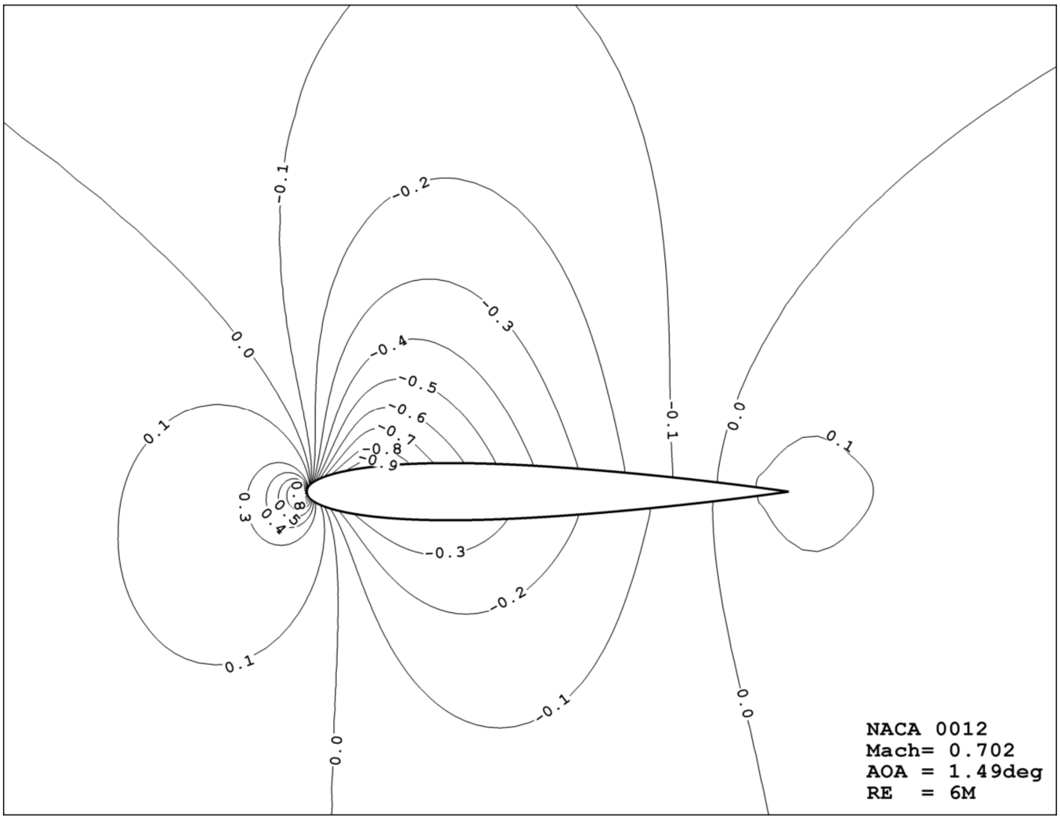

Figure 3-3 Pressure contours around the NACA 0012 airfoil (M_∞=0.702, α=1.49^o)

At this freestream Mach number and the angle of attack value, both of the BL and JK models capture the flow field very accurately. Euler solution has a slight difference. Since the dissipation is neglected in Euler equations, it predicts a weak shock. The differences between the viscous and inviscid results are already expected. This test case shows that the solution procedure of the JK equations works. But, still it needs to be known that if this solution procedure works for more complicated cases. The second test condition is at a higher freestream Mach number and angle of attack.

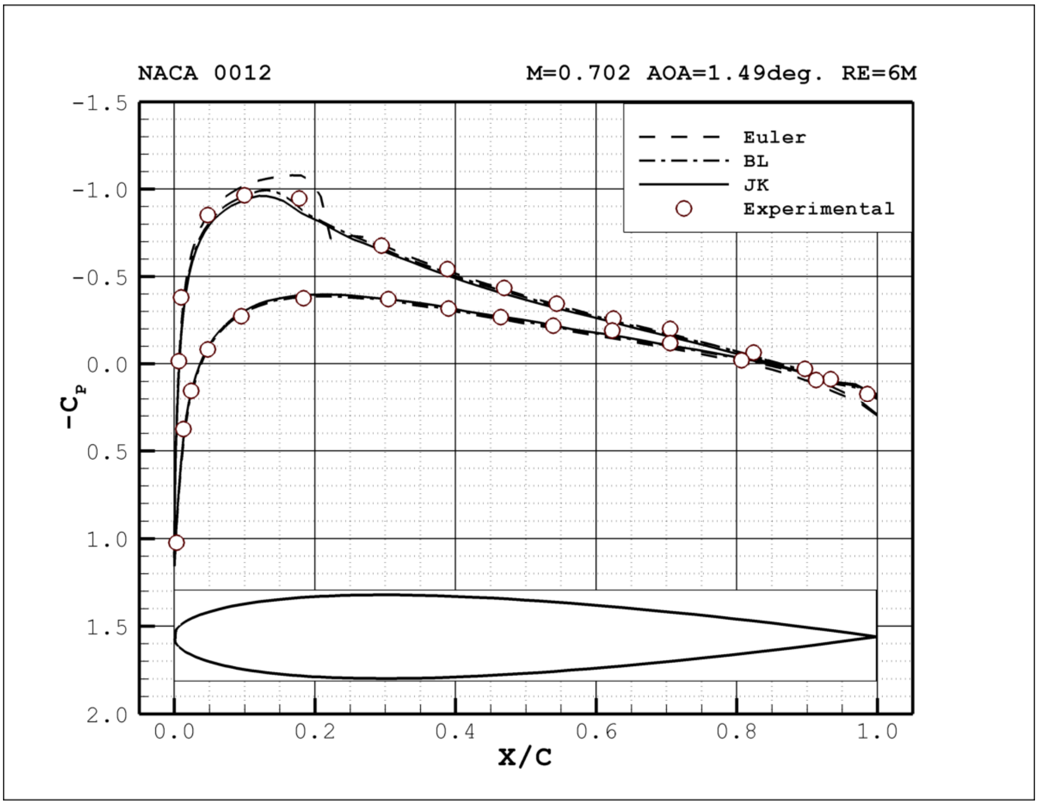

Figure 3-4 C_P distribution at M_∞ = 0.702 and α=1.49^o

Similar convergence characteristics with the first test case is observed for the following case also (M=0.799, α=2.26 deg.). In Figure 3-5, the log of the residual and lift/drag convergences are illustrated. The number of iterations used at each multigrid sequence is same. But, this time the residual drops approximately 4 orders of magnitude. The solution time does not change.

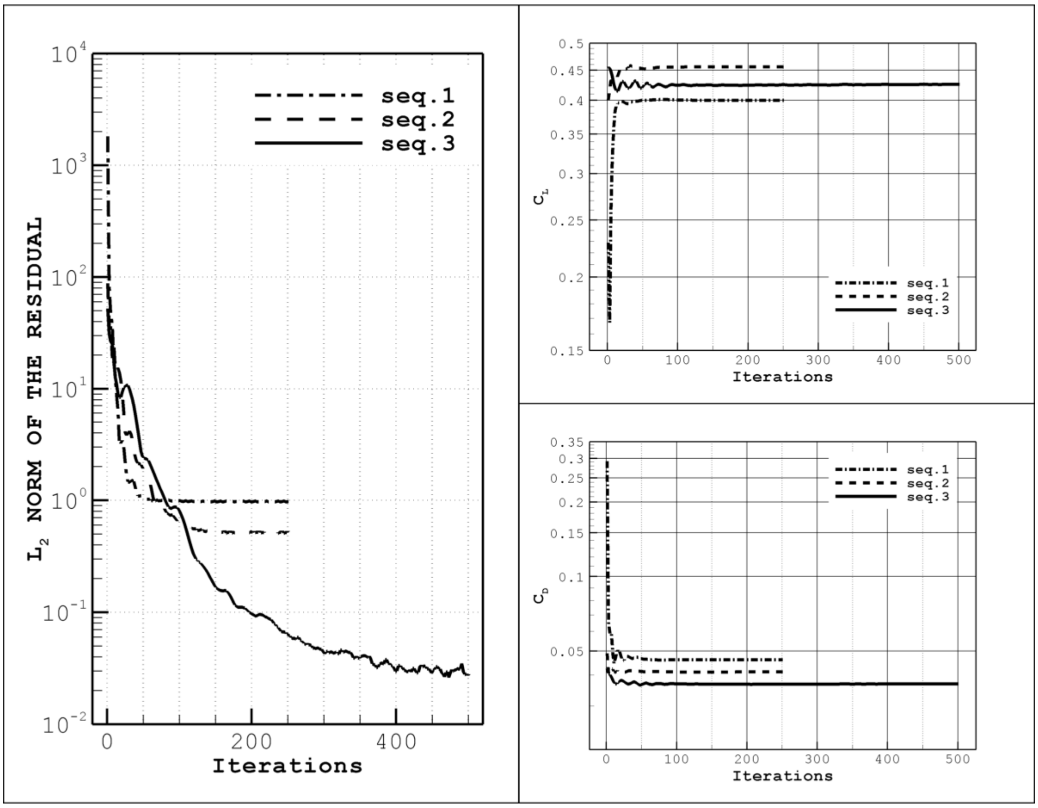

Figure 3-5 Convergence Histories of NACA 0012 airfoil (M_∞=0.799, α=2.26^o)

In Figure 3-6, pressure contours at freestream Mach number, M_∞=0.799 and the angle of attack, α=2.26 deg. is drawn, in which a shock is observed. The results belong to Euler, BL and JK turbulence models are compared with the experimental data in Figure 3-7.

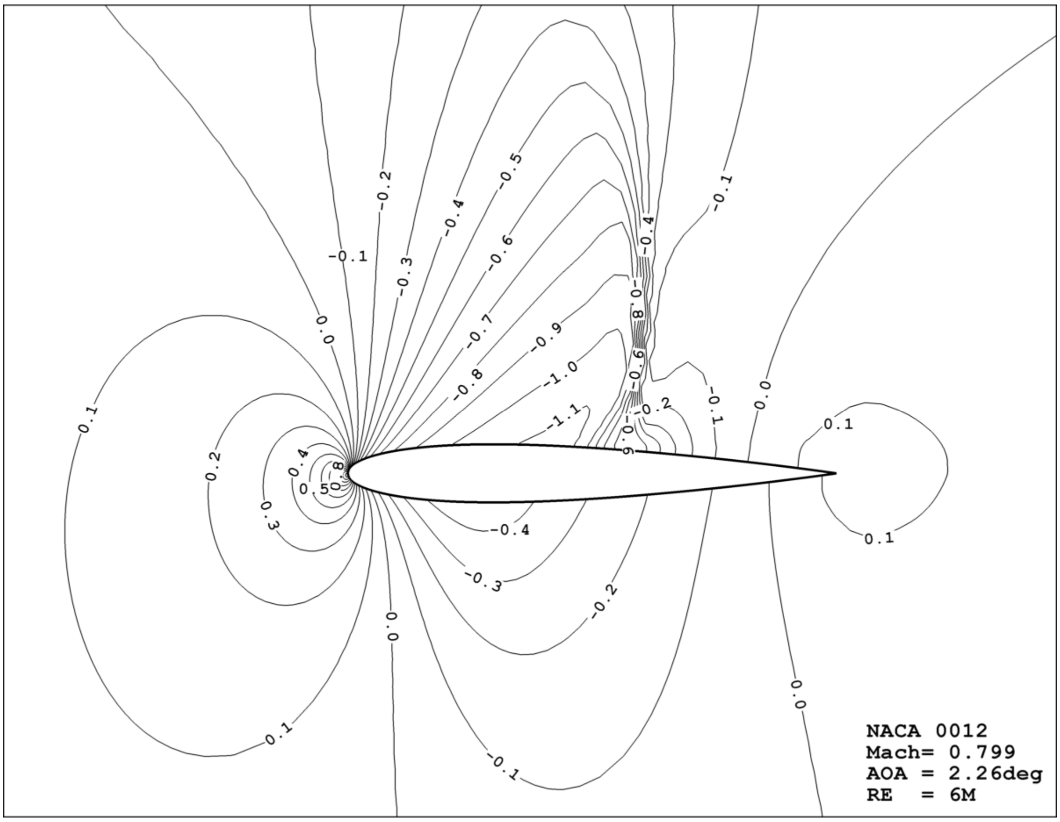

Figure 3-6 Pressure contours around the NACA 0012 airfoil (M_∞=0.799, α=2.26^o)

Since Euler solutions do not consider the viscous effects and besides, the momentum dissipation due to the boundary layer effects is neglected, the differences in the surface pressures occur between the experimental data and the Euler results is as expected. The BL turbulence model predicts separation much farther aft. Overall agreement of the JK computation with the experimental data is much more reasonable.

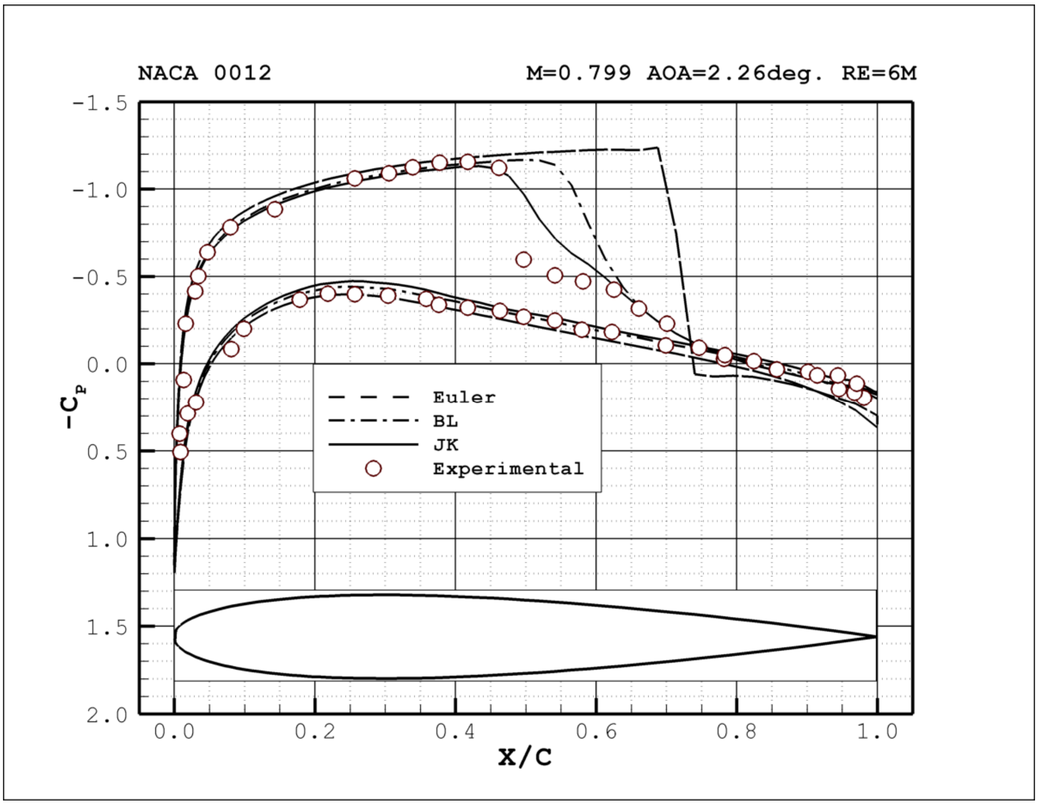

Figure 3-7 C_P distribution at M_∞ = 0.799 and α=2.26^o

At M_∞ = 0.799, the flow produces a transonic shock on the upper surface at approximately, x/c= 0.456. In Figure 3-8, velocity contours near the reverse flow region and streamlines of the recirculating flow over the airfoil is shown. The boundary layer separates due to the adverse pressure gradient immediately downstream of the shock, causing a great increase in the pressure distribution over the surface, then the flow reattaches.

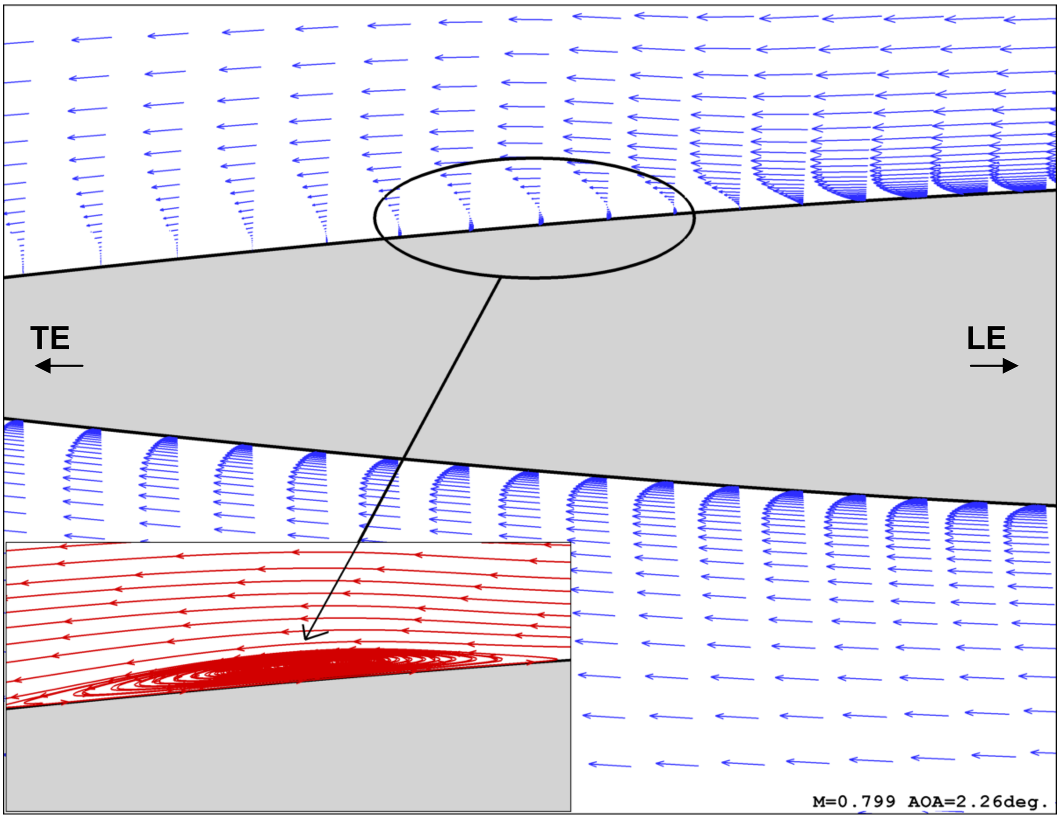

Figure 3-8 Velocity contours & streamlines around NACA 0012 (M_∞ = 0.799, α=2.26^o)

NACA 0012 test case helps establishing the validity of the JK turbulence model. However, the following test cases are more important since they are three dimensional flow cases.

3.3 Test Case II: ONERA M6 Wing

The reason of selecting ONERA M6 wing as a test case is that, it is a simple swept wing with local supersonic flow, shocks, turbulent boundary layers and flow separation. It is a classic CFD validation case for external flows. The wind tunnel model is shown in Figure 3-9. The experimental test results [1] were obtained at transonic Mach number and various angles-of-attacks with a Reynolds number of $11x10^6$ based on the mean aerodynamic chord. These results are used for the validation of the JK turbulence model, while comparing with the other solutions.

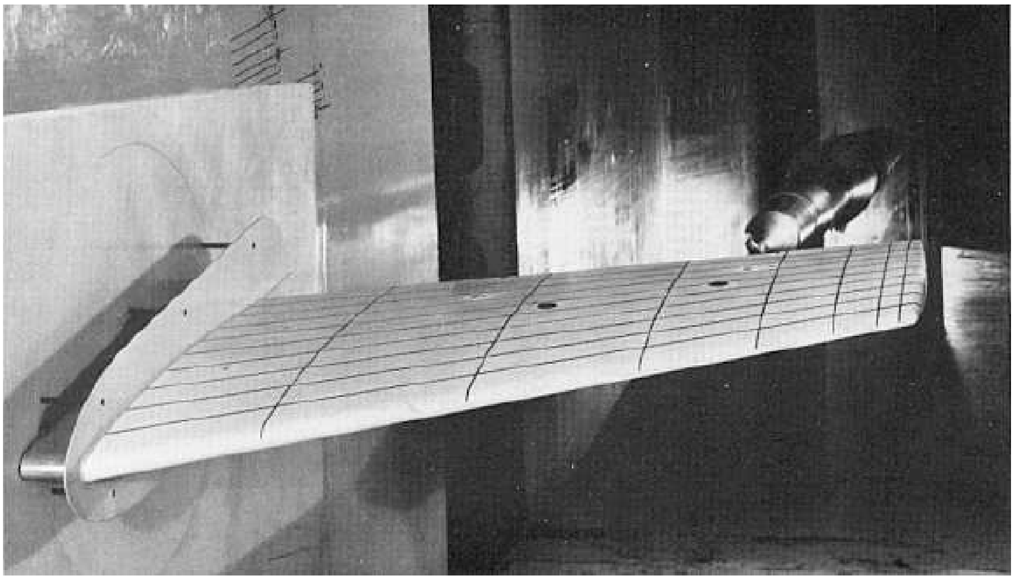

Figure 3-9 Wind Tunnel Model of the ONERA M6 Wing

ONERA M6 wing has an aspect ratio of 3.8 and the taper ratio is 0.562. Its leading edge sweep angle is 30 degrees and the quarter chord sweep is 26.7 degrees [1]. The five spanwise stations, where the surface pressure distributions are investigated, are as shown in Figure 3-10. The spanwise stations in percent are represented by η.

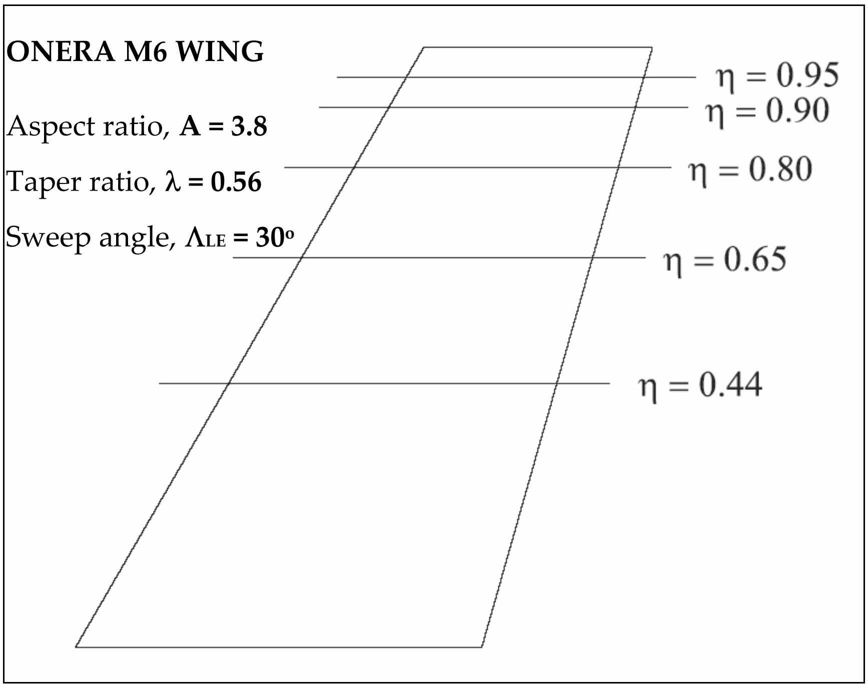

Figure 3-10 Geometric layout of the ONERA M6 Wing

The computations were performed at the transonic separated flow conditions of Mach number 0.84, the angles of attack are 5.06 degrees and 6.06 degrees, and the Reynolds number is set at 11×10^6. The angle of attack value of 6.06 degree is the case which is pointed as the most difficult flow condition by different authors [13, 14]. Nevertheless, there are also remarkably good earlier solutions [2, 4]. For this thesis, it is concluded that the flow at these angles of attack is a challenging task and therefore chosen as a second test case.

The grid is C-H type with dimensions 193x65x49 points in the streamwise, spanwise and the normal directions respectively (Figure 3-11). The first point off the surface in the normal direction was at 1×10^{-5} chord lengths distance in order to resolve the wall gradients, and there were 30 points inside the boundary layer. The region between the viscous sublayer ($y^+ \leq 5$) and the log-law region ($y^+ \geq 30$) is called the buffer layer. It is the transition region between the viscosity dominated and the turbulence dominated parts of the flow [15]. Therefore, it is important to capture the flow physics accurately by insertion of enough points in the boundary layer for the viscous flow calculations.

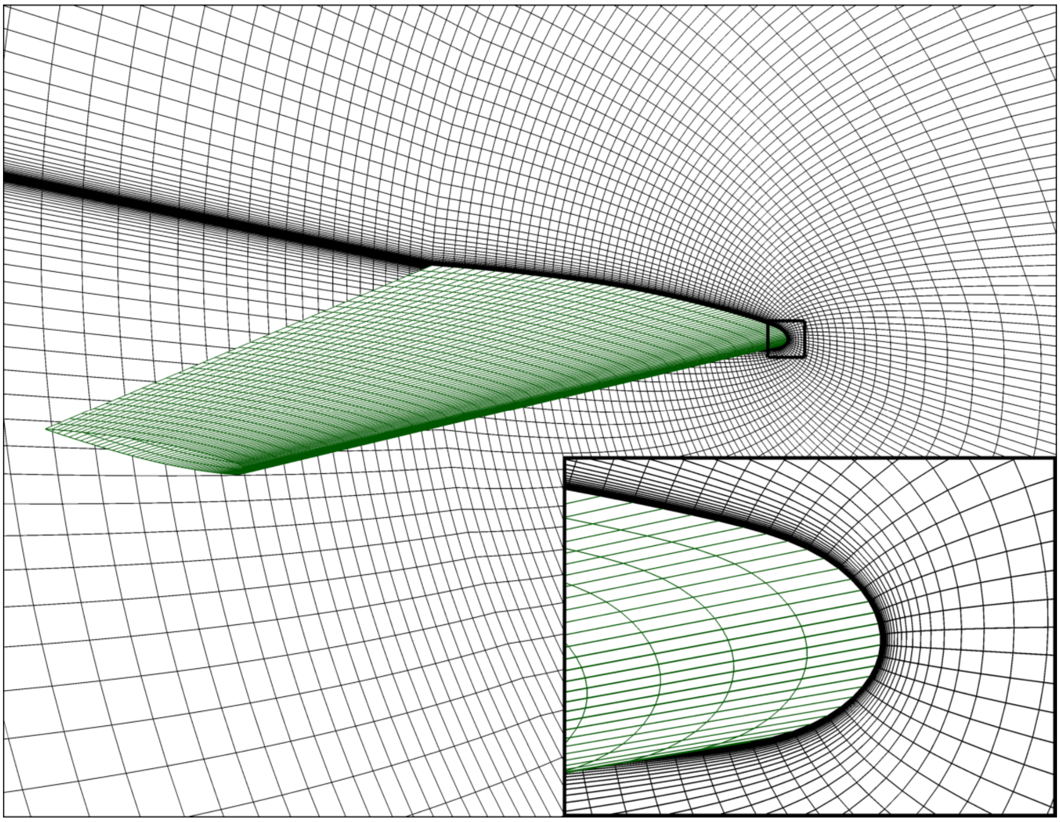

Figure 3-11 Mesh around the ONERA M6 Wing

The convergence characteristics are given in Figure 3-12 for the initial flow condition (M_∞=0.86 and α=5.06 degrees) with the log of the residual and force coefficients. The 3 levels of multigrid were used. In order to determine the numbers for each iterations, the convergence of the initial long run is investigated for each test case. For this case the number of iterations for initial two sequences are chosen as 4000 and for the fine grid sequence, it is 5000. The residual dropped approximately 4 orders of magnitude. This solution took just over 1 day (wall time) on PC.

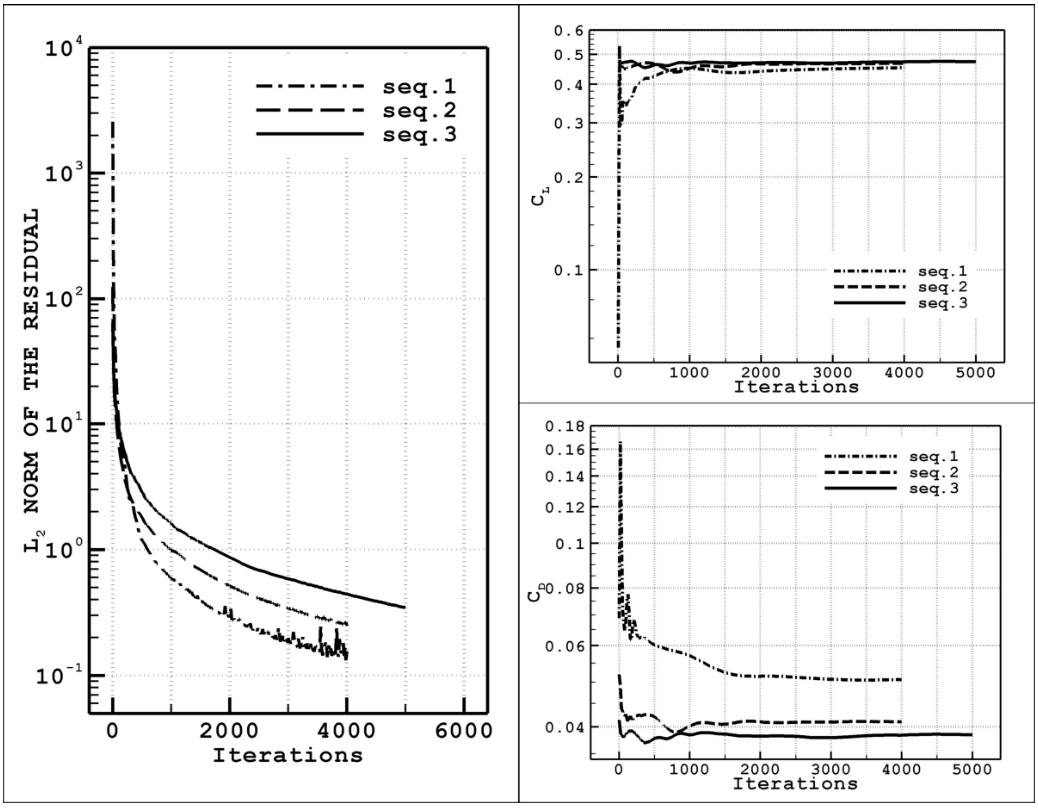

Figure 3-12 Convergence Histories of ONERA M6 wing (M_∞=0.86, α=5.06^o)

Figure 3-13, 3-14, and 3-15 depicts the surface pressure distributions and “oilflow” patterns obtained from the Euler, BL and JK calculations at the angle of attack of 5.06 degrees. In these pictures, lambda type shock pattern, which is typical of this wing and can be recognized easily by resembling the Greek symbol λ, is captured for all solution techniques. The shock-induced separated flow region is observed only for viscous solutions. It can be seen that this separation region is significant only at the outboard portion of the wing for BL solution. However, the JK model produces larger reverse flow region and there is also a slight separation in the middle portion of the wing. Two regions of counter-rotating flows, one emanating from and the other terminating in a node, are as shown by the letter ‘N’. The saddle points, S, are also seen in figures.

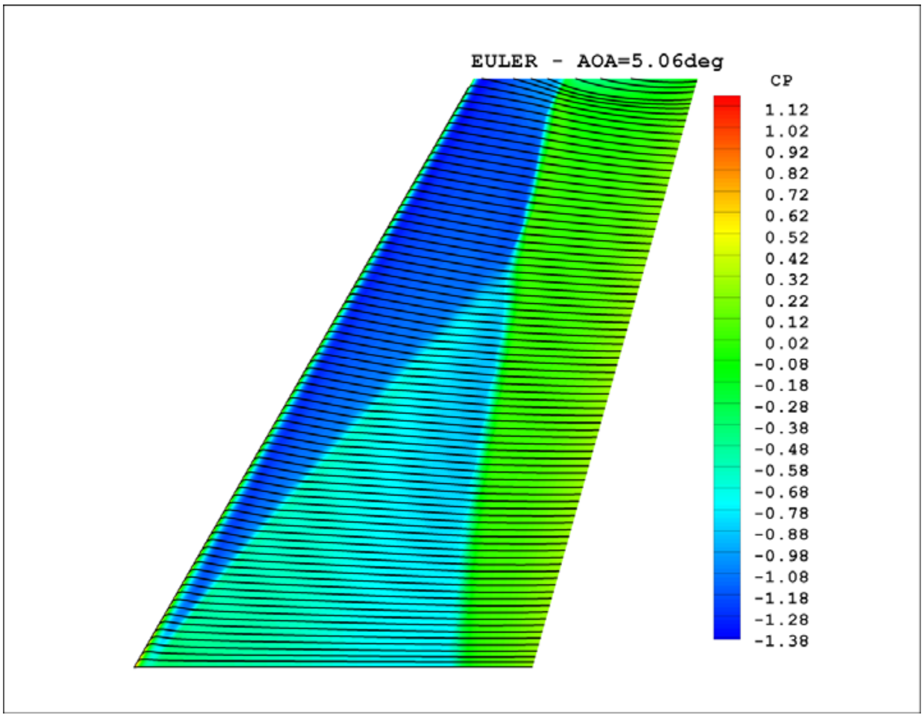

Figure 3-13 "Oilflow" patterns over ONERA M6 Wing – Euler (M_∞ = 0.86, α=5.06°)

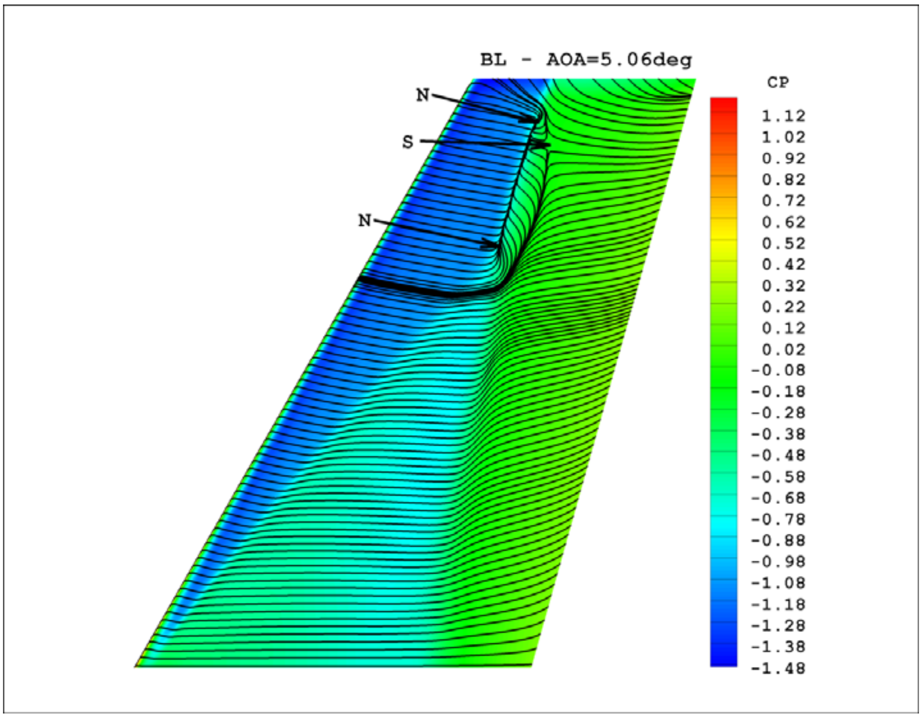

Figure 3-14 "Oilflow" patterns over ONERA M6 Wing – BL (M_∞ = 0.86, α=5.06°, N: node point, S: saddle point)

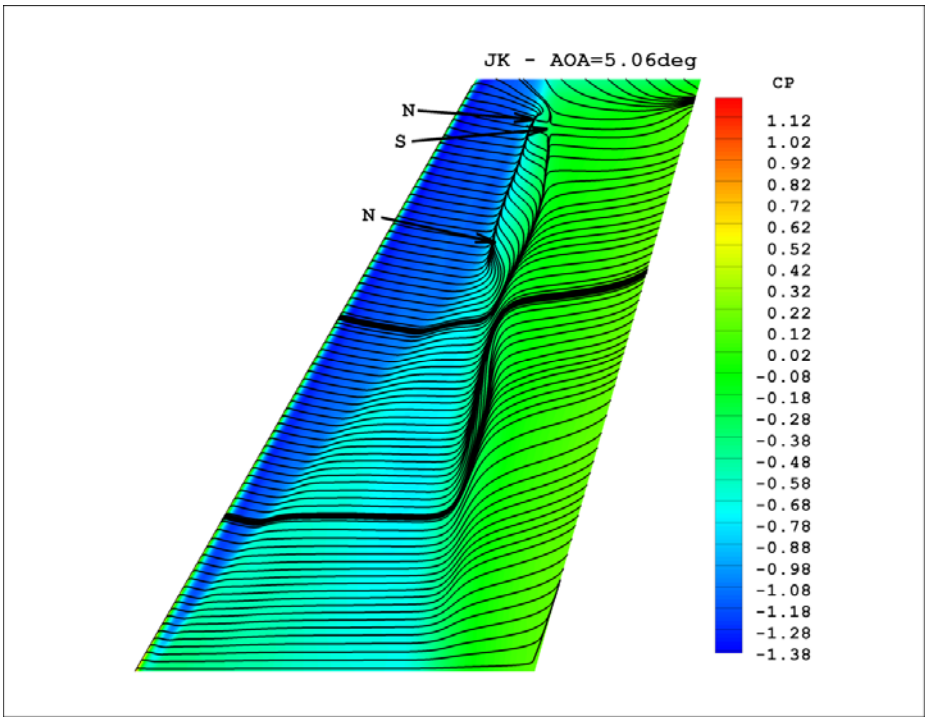

Figure 3-15 "Oilflow" patterns over ONERA M6 Wing – JK (M_∞ = 0.86, α=5.06^o, N: node point, S: saddle point)

The surface pressure coefficient distribution along five spanwise stations at 44-, 65-, 80-, 90-, 95- percent fractional semi span of the solution obtained at first flow condition, which is Mach number is 0.86 and the angle of attack is 5.06 degrees, is presented in Figure 3-16, 3-17, 3-18, 3-19, and 3-20. In general, the BL model has a downstream shock wave compared with the JK model. The results of the JK model are much more close to the experimental data as the cross sectional station moves towards wing tip, where the separation is dominated. Although the overall agreement of the JK results with the experiment is good, it may still need some tuning of the model or the grid convergence study.

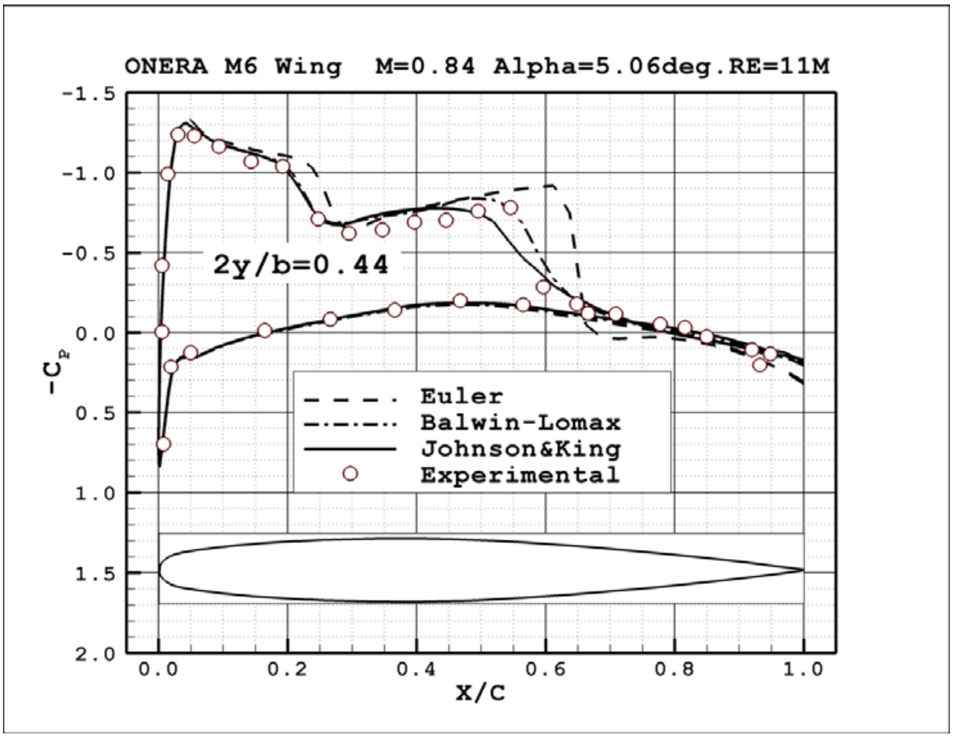

Figure 3-16 C_P distribution at M_∞ = 0.86 and α=5.06^o (at 2y/b=0.44)

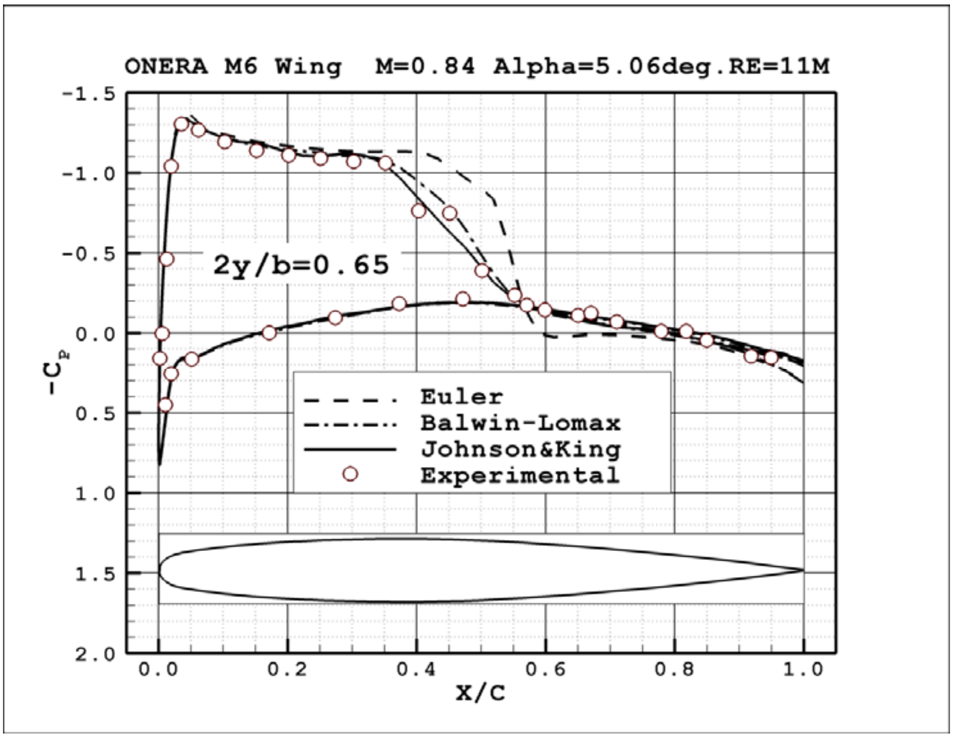

Figure 3-17 C_P distribution at M_∞ = 0.86 and α=5.06^o (at 2y/b=0.65)

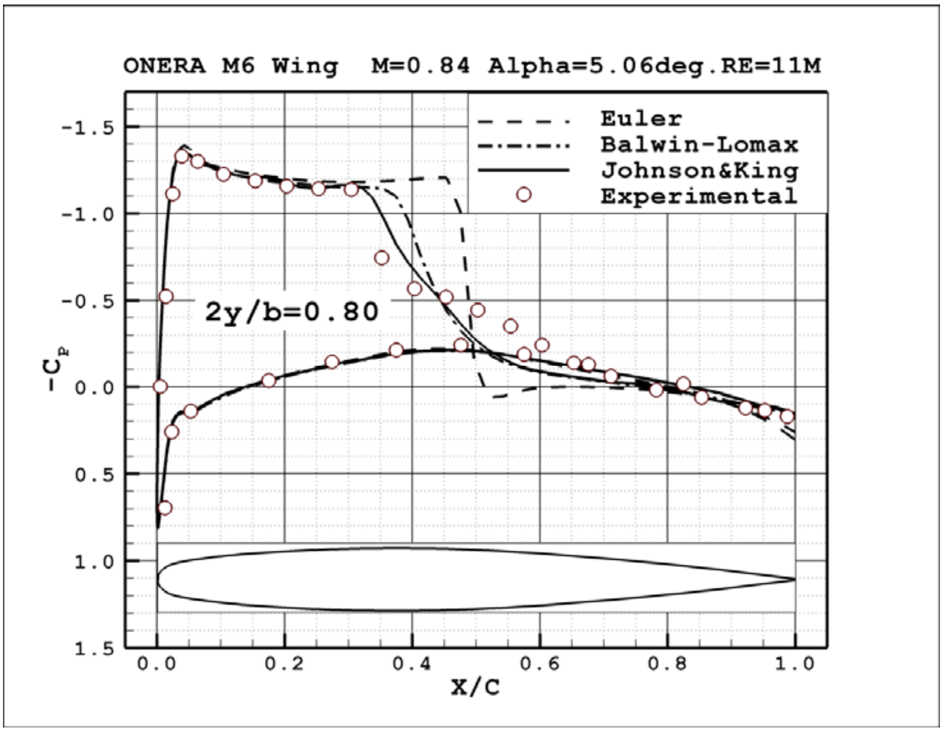

Figure 3-18 C_P distribution at M_∞ = 0.86 and α=5.06^o (at 2y/b=0.80)

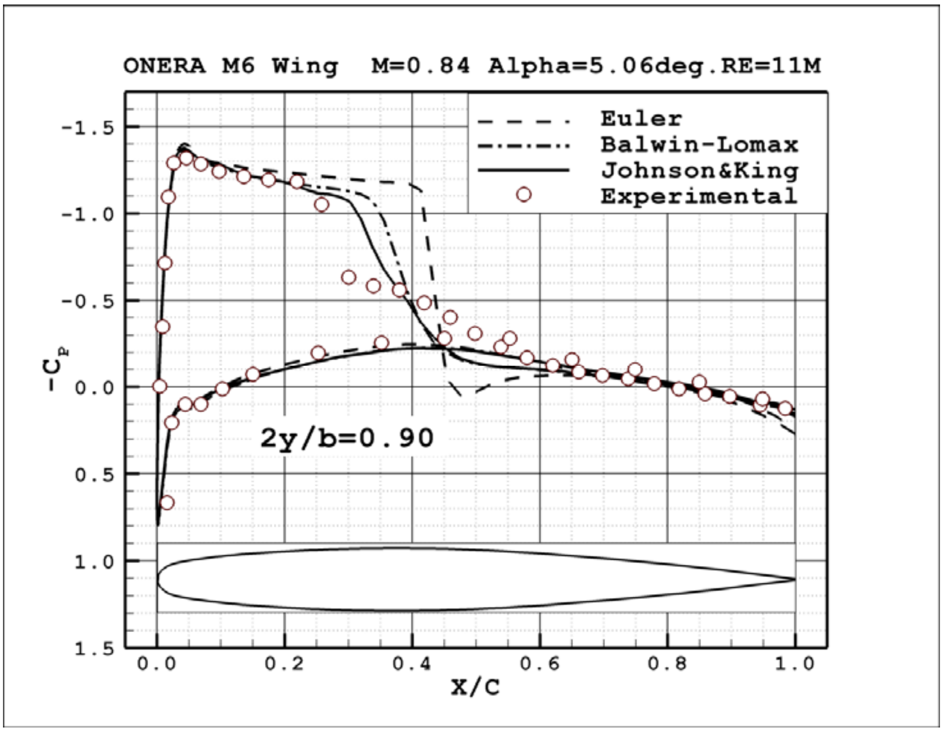

Figure 3-19 C_P distribution at M_∞ = 0.86 and α=5.06^o (at 2y/b=0.90)

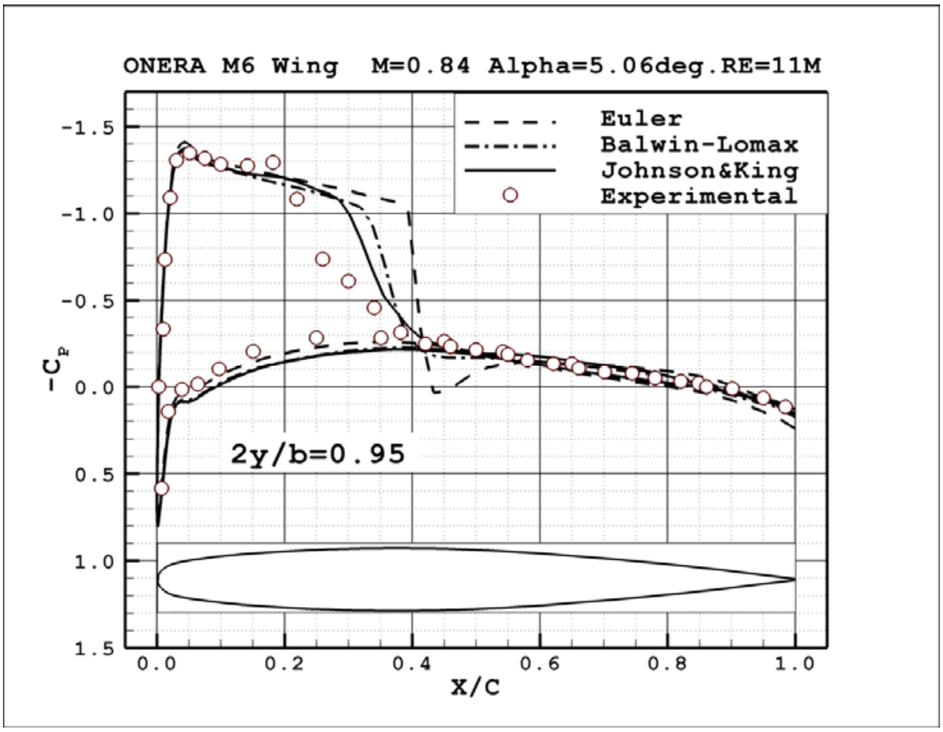

Figure 3-20 C_P distribution at M_∞ = 0.86 and α=5.06^o. (at 2y/b=0.95)

The second case is at the same Mach number but at higher angle of attack, 6.06 degrees. This test condition is difficult having a stronger lambda type of shock pattern with a large separated flow region. Therefore, keeping the iteration numbers constant at 4000 for the first two cycles, the number of iterations at fine grid level is increased to 8000 to obtain a converged solution. The convergence characteristics are illustrated in Figure 3-21. The residual dropped about 4 orders of magnitude. Besides, the solution time is increased to approximately 11 hours, which makes in total 1.5 days (wall time) on PC.

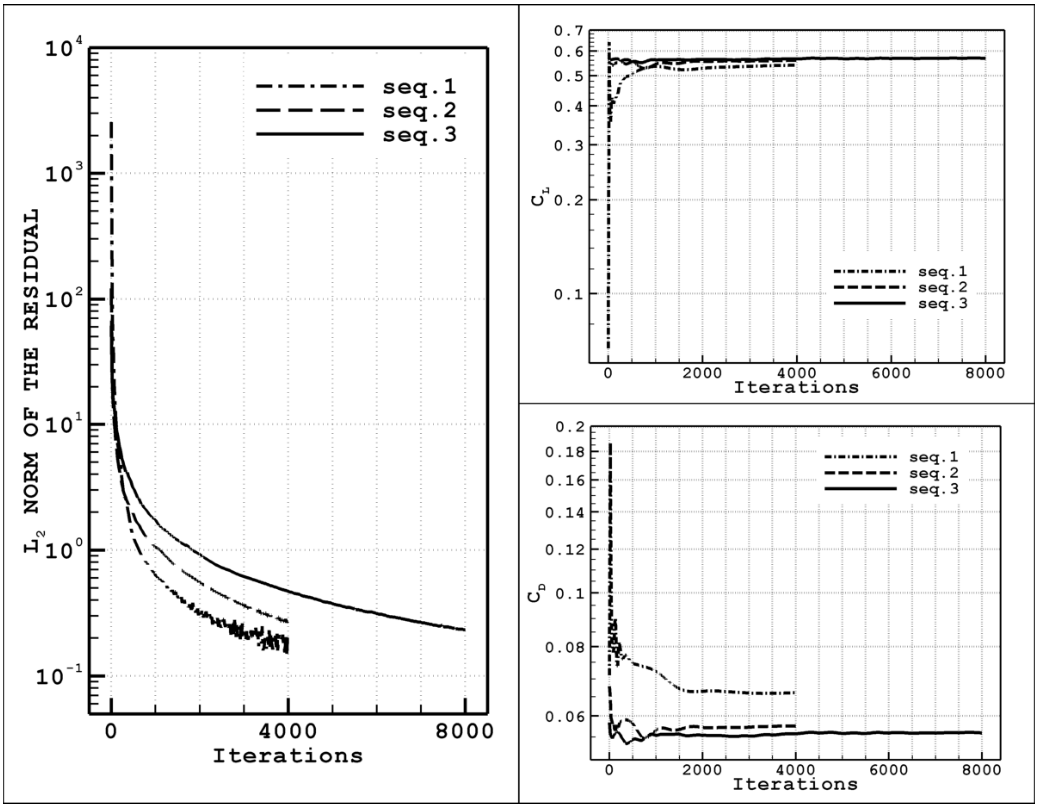

Figure 3-21 Convergence Histories of ONERA M6 wing (M_∞=0.86, α=6.06^o)

The surface pressure distributions and "oilflow" patterns on the upper surface of the Euler, BL and JK calculations at the angle of attack of 6.06 degrees are demonstrated in Figures 3-22, 3-23, and 3-24. Although there is no surface flow visualization data available for comparison, the overall flow pattern is observed for different solution methods. It is observed that the extent of the separated flow region predicted with the JK model is much larger compared to the BL results.

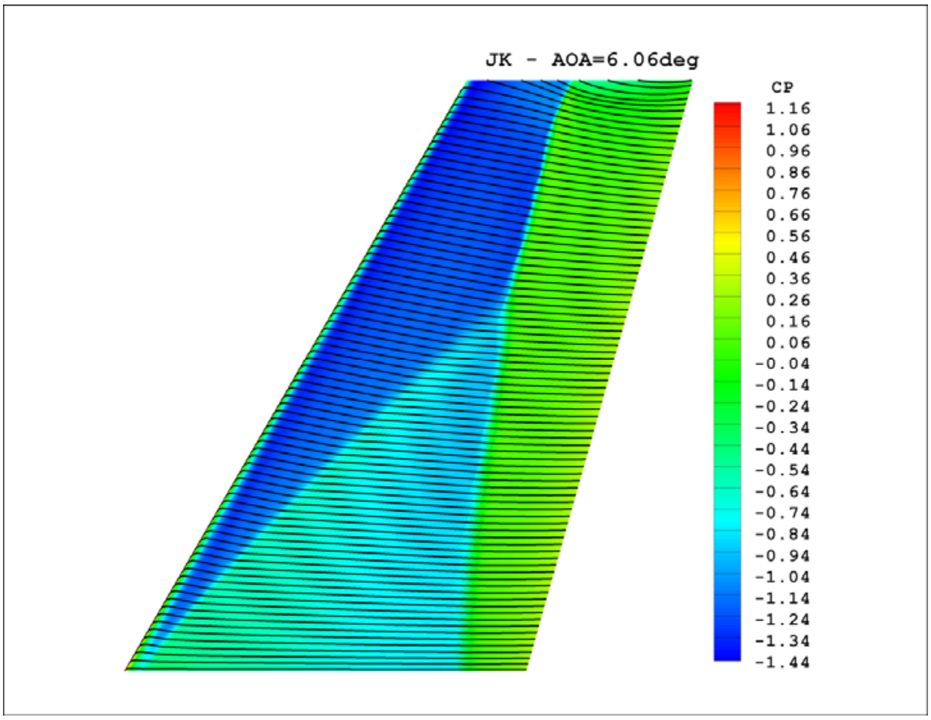

Figure 3-22 “Oilflow” patterns over ONERA M6 Wing – Euler (M_∞ = 0.86, α=6.06^o)

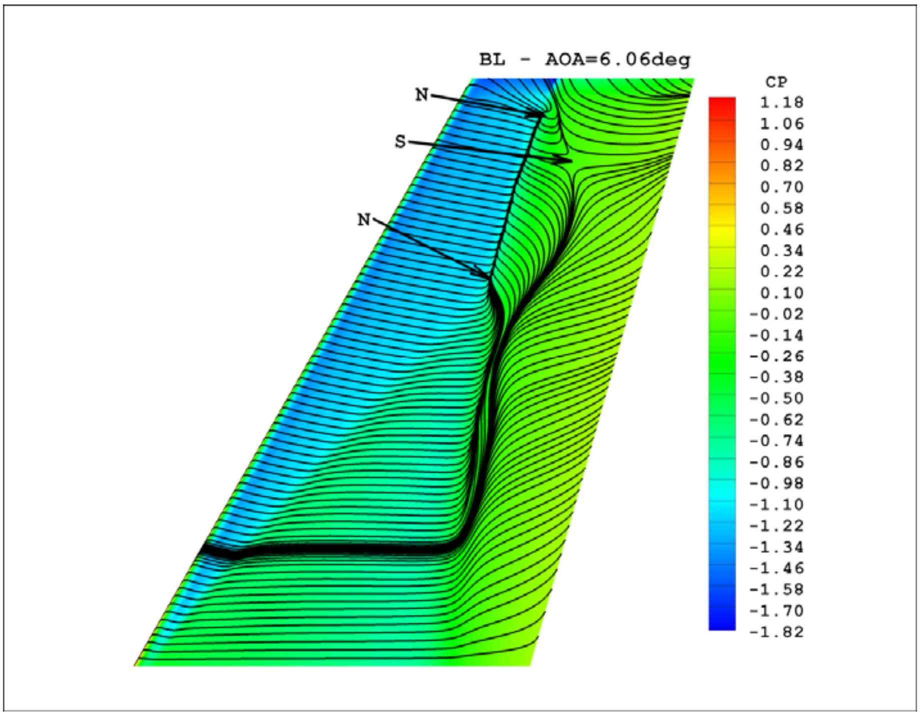

Figure 3-23 “Oilflow” patterns over ONERA M6 Wing – BL (M_∞ = 0.86, α=6.06^o, N: node point, S: saddle point)

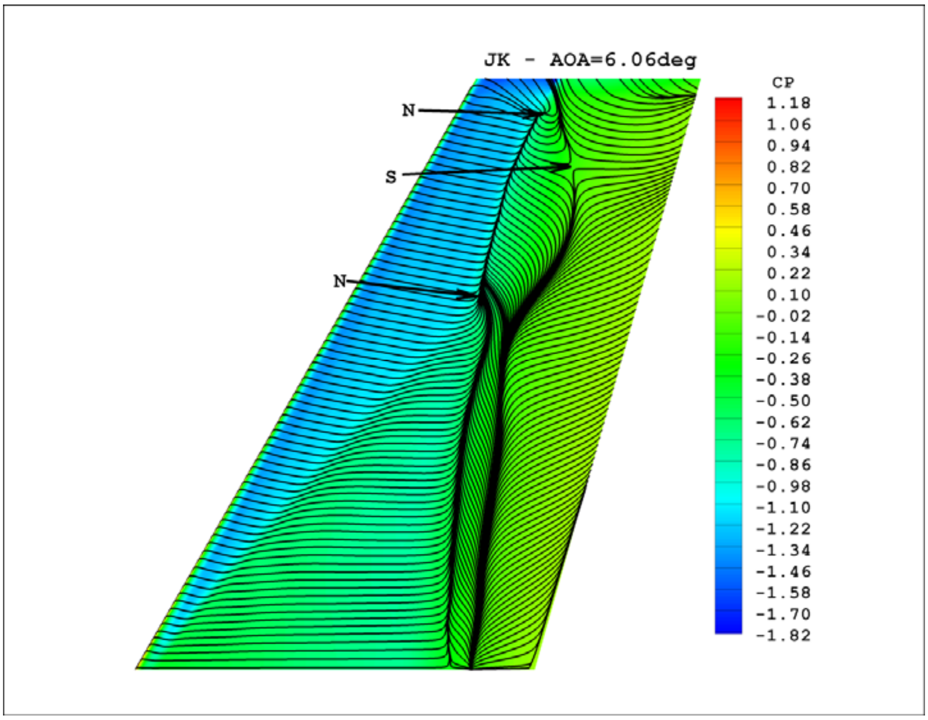

Figure 3-24 "Oilflow" patterns over ONERA M6 Wing – JK (M_∞ = 0.86, α=6.06^o, N: node point, S: saddle point)

In the following figures (Figure 3-25, 3-26, 3-27, 3-28, and 3-29), the calculated surface pressure distributions along five spanwise stations at 44-, 65-, 80-, 90-, 95- percent fractional of the semi span are compared with the experimental data at freestream Mach number of 0.86 and at the angle of attack 6.06degrees. The BL model captured the shock wave downstream of the experiment, while the JK model predicts quite satisfactorily. The reason of predicting the shock position much further upstream is explained as stating that the JK model produces lower values of eddy viscosity in adverse pressure gradient regions causing a thicker boundary layer and the upstream movement of the shock [11]. At 44% and 65% stations, shock locations are remarkably correlated with the experimental results, whereas at outer stations (80%, 90% and 95%), predicted shock locations are far from the experimental data.

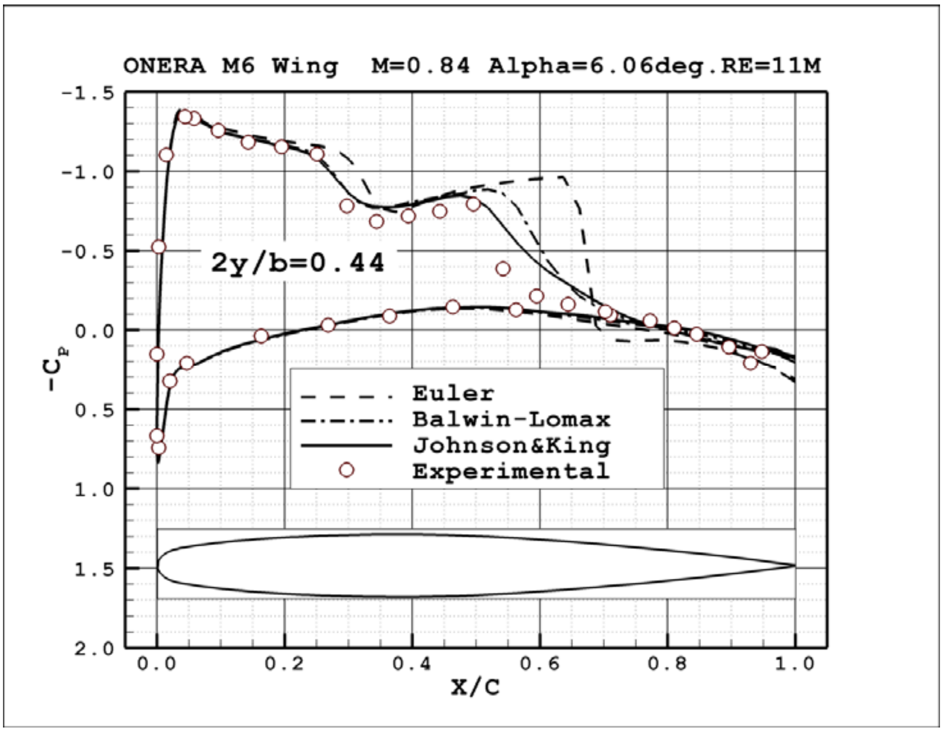

Figure 3-25 C_P distribution at M_∞ = 0.86 and α=6.06^o (at 2y/b=0.44)

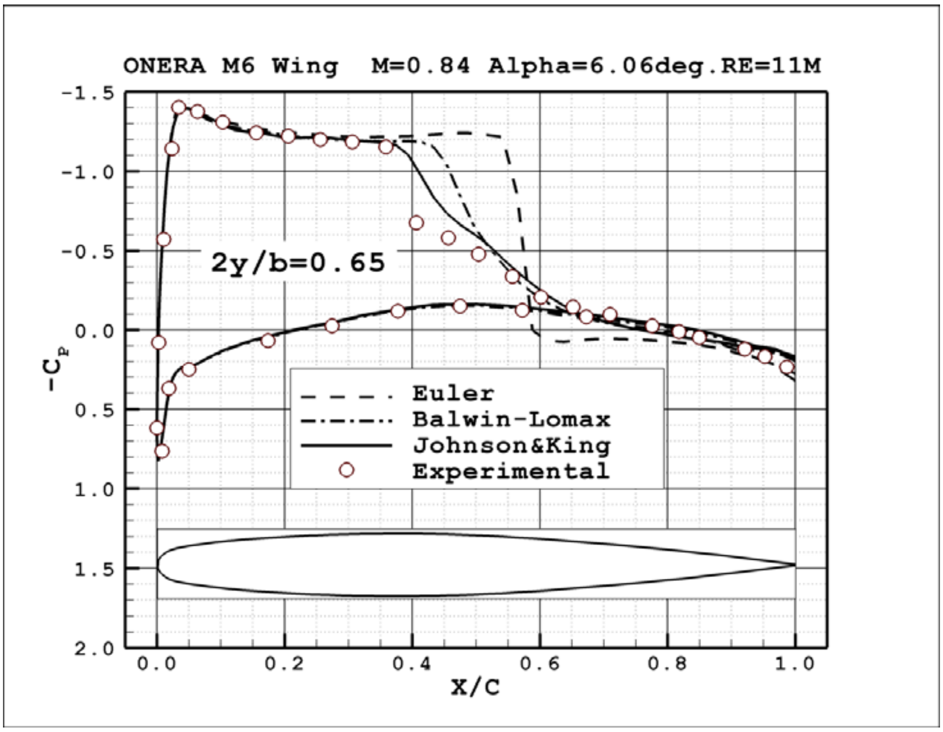

Figure 3-26 C_P distribution at M_∞ = 0.86 and α=6.06^o (at 2y/b=0.65)

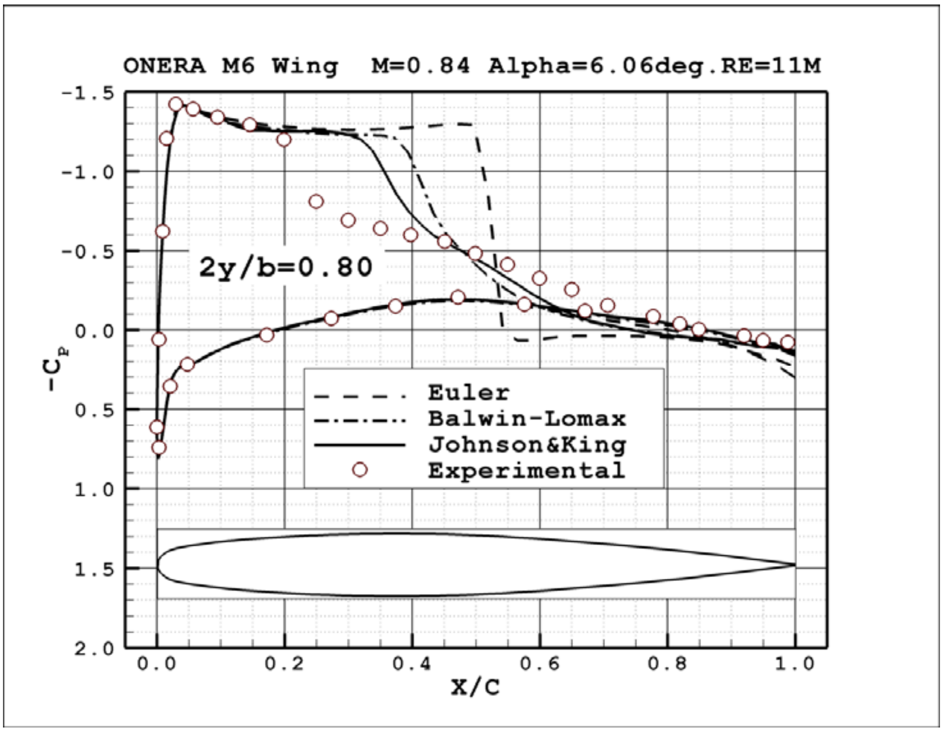

Figure 3-27 C_P distribution at M_∞ = 0.86 and α=6.06^o (at 2y/b=0.80)

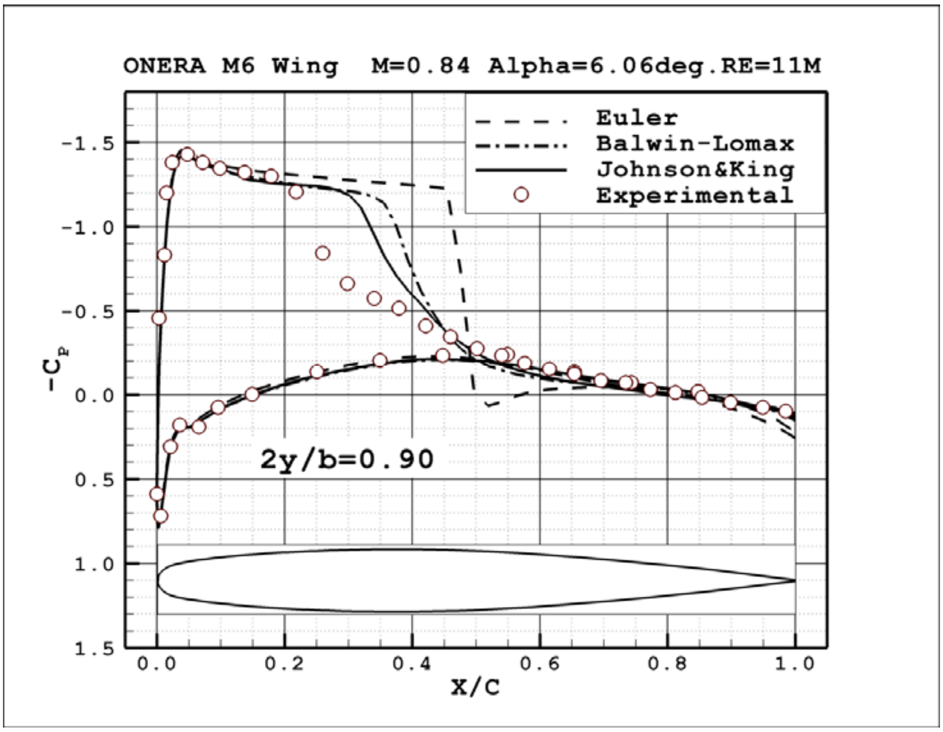

Figure 3-28 C_P distribution at M_∞ = 0.86 and α=6.06^o (at 2y/b=0.90)

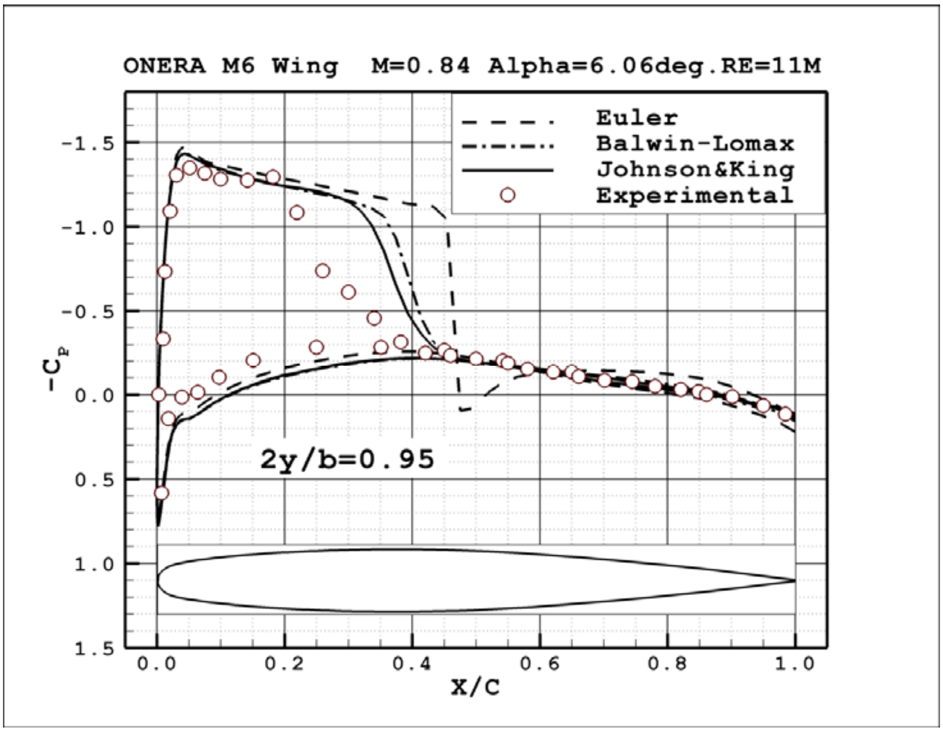

Figure 3-29 C_P distribution at M_∞ = 0.86 and α=6.06^o (at 2y/b=0.95)

Until now, the numerical results are only compared with surface pressure distribution on some stations along the wing. In the following test case, however, aerodynamic coefficients are also investigated.

3.4 Test Case III: DLR-F4 Wing

DLR-F4 model is actually a wing/body configuration of a transonic transport aircraft. However, the three dimensional transonic swept wing is modeled and the flow is investigated using this model. There are two leading reasons for selecting this test case. Firstly, the model has been extensively tested in three different European wind tunnels including the High-Speed Wind Tunnel of the National Aerospace Laboratory (NLR-HST), the ONERA-S2MA wind tunnel, and 8ft x 8ft Pressurized Subsonic/Supersonic Wind Tunnel of the Defense Research Agency (DRA), the details of which can be found in [6]. Secondly, the model also has extensive experimental data, including aerodynamic coefficients, providing a good candidate database for the CFD comparisons.

DLR-F4 wing has an aspect ratio of 9.5 and the taper ratio is 0.3. Its leading edge sweep angle is 27.1 degrees and the quarter chord sweep is 25 degrees. Twist distribution is incorporated in wing sections [6]. The six spanwise stations, in which the surface pressure distribution was investigated, are as shown in Figure 3-30.

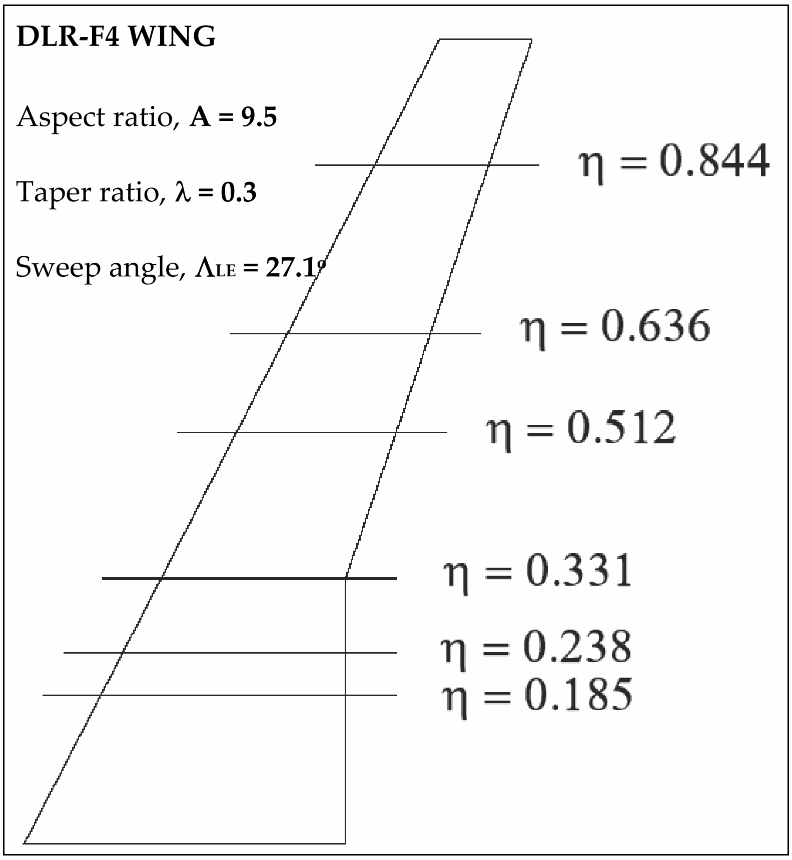

Figure 3-30 Geometric layout of the DLR-F4 Wing

The grid for the present calculations is C-H type. Three-level multigrid is employed, and accordingly the mesh is composed of 193x65x49 points (Figure 3-31).

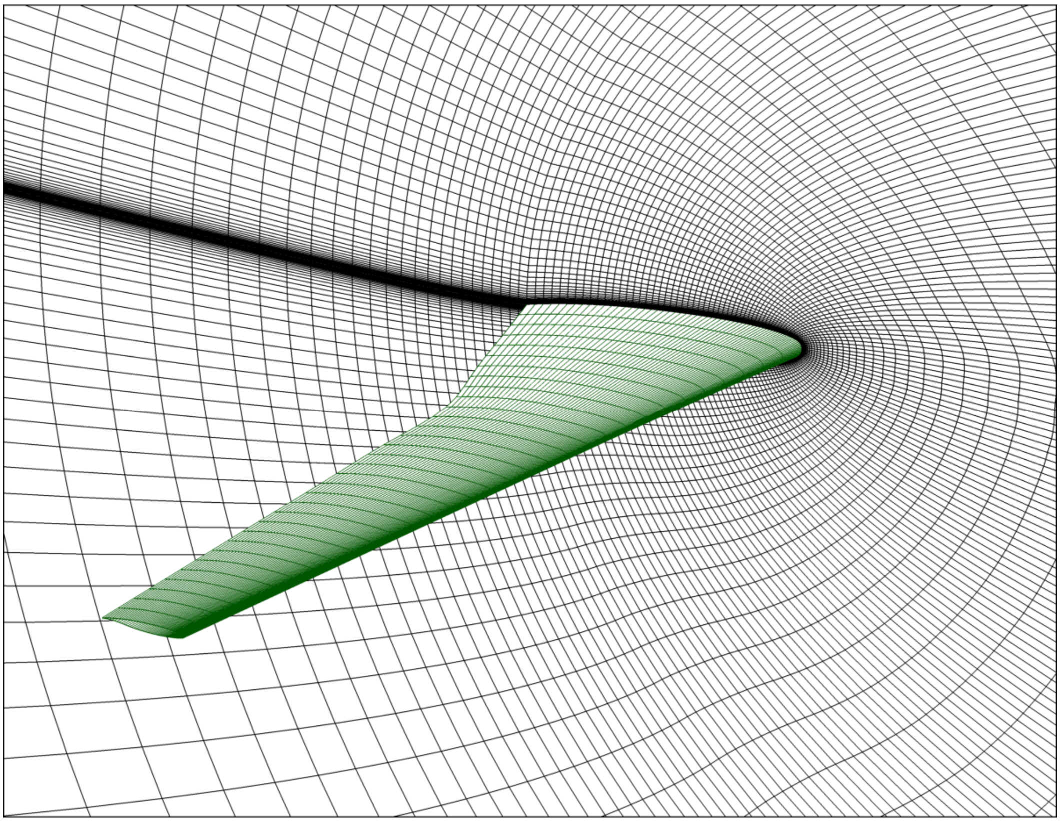

Figure 3-31   Mesh around the DLR-F4 Wing

For three different Mach numbers, wide ranges of angles of attack computations are performed. Resulting lift curve and drag polar of the wing are compared with the experimental wing/body data. The surface pressure comparisons on the wing are pursued, at the freestream condition of M_∞ = 0.6, the angle of attack α=1.0 degrees, and at a Reynolds number of 3 $x10^6$.

Figure 3-32 presents the characteristics of the convergence for a representative run (M=0.6, α=1.0 deg.) by including the log of the residual and lift/drag convergences. The number of iterations is: 200 for coarse-grid, 400 for medium-grid, and 800 for fine-grid. The residual dropped 5 orders of magnitude. Each solution took less than 4 hours (wall time) on PC.

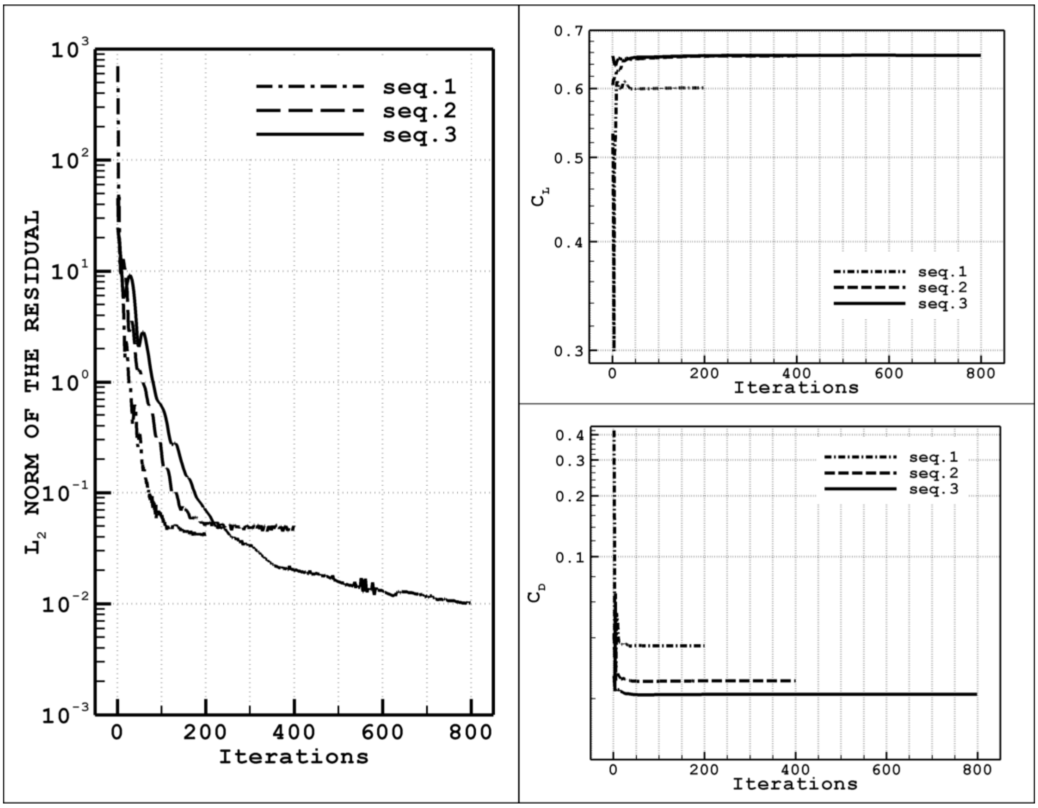

Figure 3-32 Convergence Histories of the DLR-F4 wing (M_∞=0.6, α=1.0^o)

Next two figures (Figure 3-33 and Figure 3-34) show pressure contours and streamlines on the wing. The color bands basically represent the shock as the colors change from blue to green. In other words, attached transonic flow over this sweptback wing with pockets of supersonic flow on the upper surface is terminated by weak shock waves. A small trailing edge separation is observed in the kink region of the trailing edge. Also, there is a slight outboard turning of the flow near the trailing edge in sections close to the wing tip.

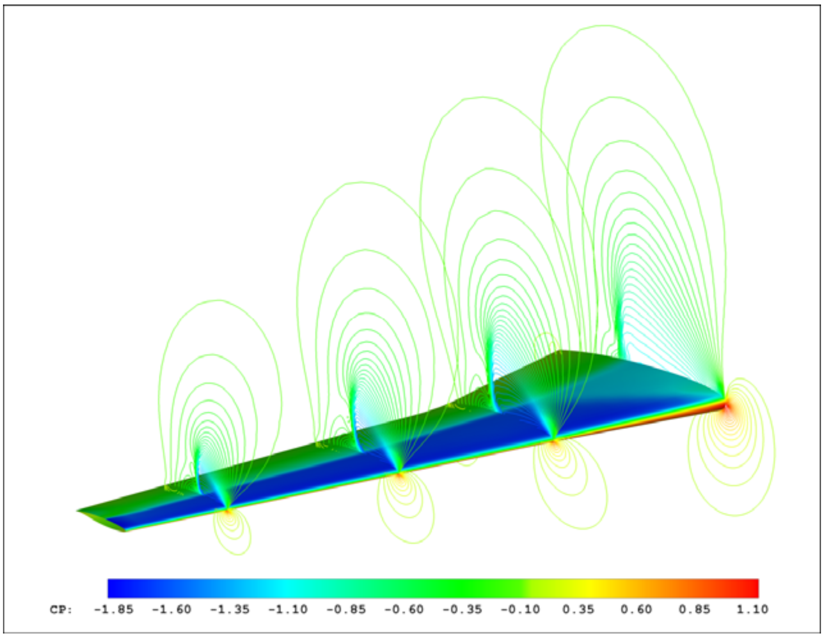

Figure 3-33 Surface pressure distribution at transonic regime (M=0.75, AOA=4.24^{o})

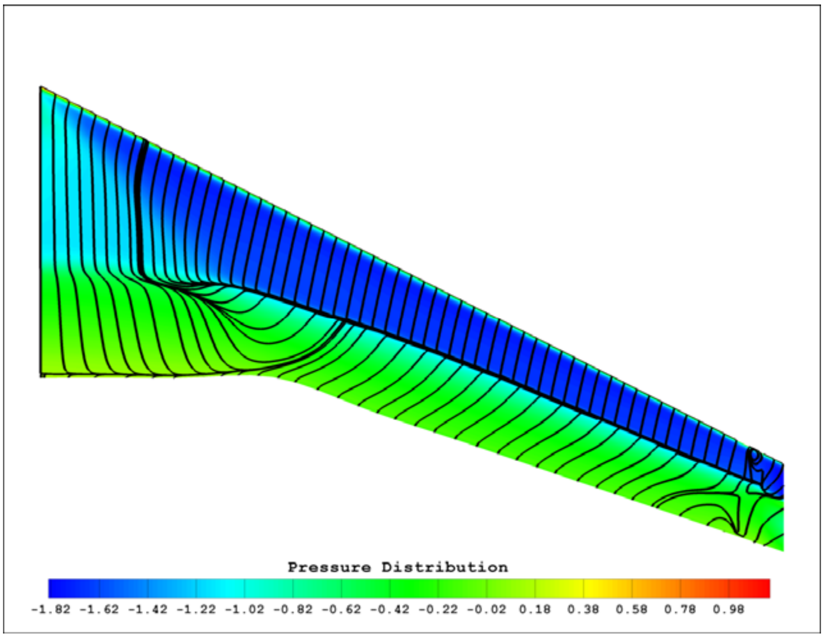

Figure 3-34 “Oilflow” patterns over DLR-F4 wing (M=0.75, AOA=4.24^{o})

In order to obtain lift curve and drag polar, the entire range of angle of attack is investigated for three different Mach numbers (0.60, 0.75, and 0.80). The

Reynolds number of $3x10^6$ was used. The computed aerodynamic characteristics were compared with the experimental data in Figure 3-35, 3-36, 3-37, 3-38, 3-39, and 3-40. Both the Baldwin-Lomax and the Johnson-King Turbulence models over-predict the lift coefficient (C_L) and under-predict the drag coefficient (C_D). Since the experimental data belongs to wing/body configuration and the numerical results are calculated from wing alone, this difference could be caused by the negative influence of the fuselage. Besides, the overall trends of the turbulence models have some differences, especially at higher angles of attack. The resulting curve of the JK model has a kink on the curve. This nonlinearity in the data may correspond to separation condition. Additionally, the lift curve characteristics of the wind-tunnel data shows a similar small break in the linearity of the curve. However, BL predictions do not capture this feature. At high angle of attack values, the pressure drag due to the flow separation begins to dominate. This may be the reason, why drag coefficient initially increases similarly for both turbulence models and then at one point it starts to increase steeply for JK model. The mesh quality may be reconsidered for the differences in lift curve and drag polar. Insufficient resolution of the trailing edge and/or wake, may be affect the way circulation (if exists) and lift as well. Over prediction in lift will also affect lift dependent drag.

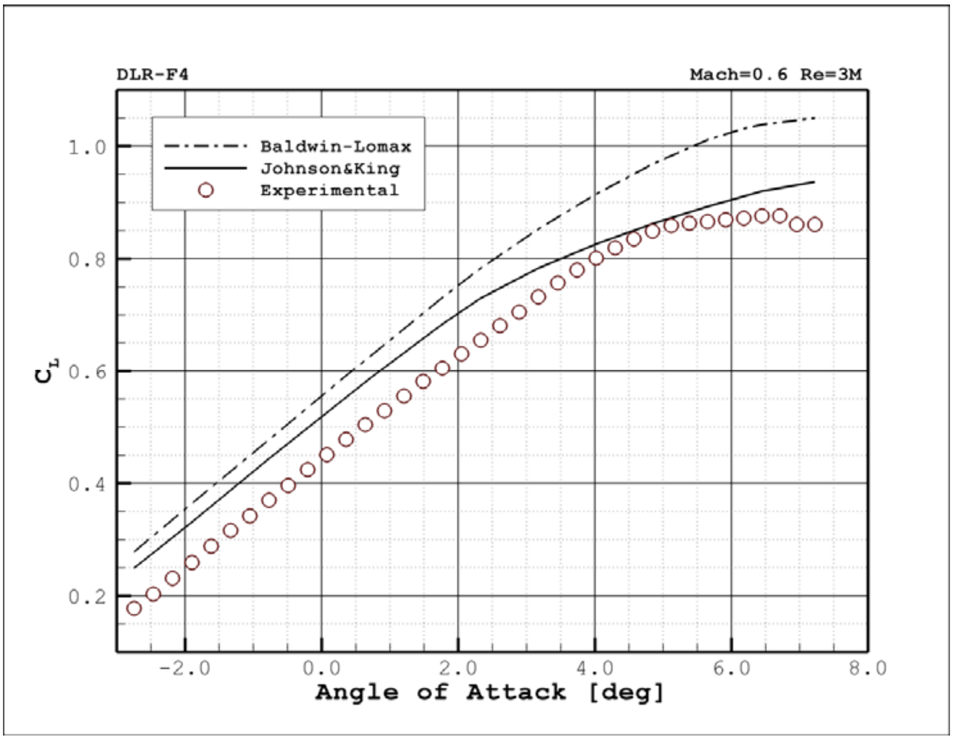

Figure 3-35 Lift Curve (M=0.60)

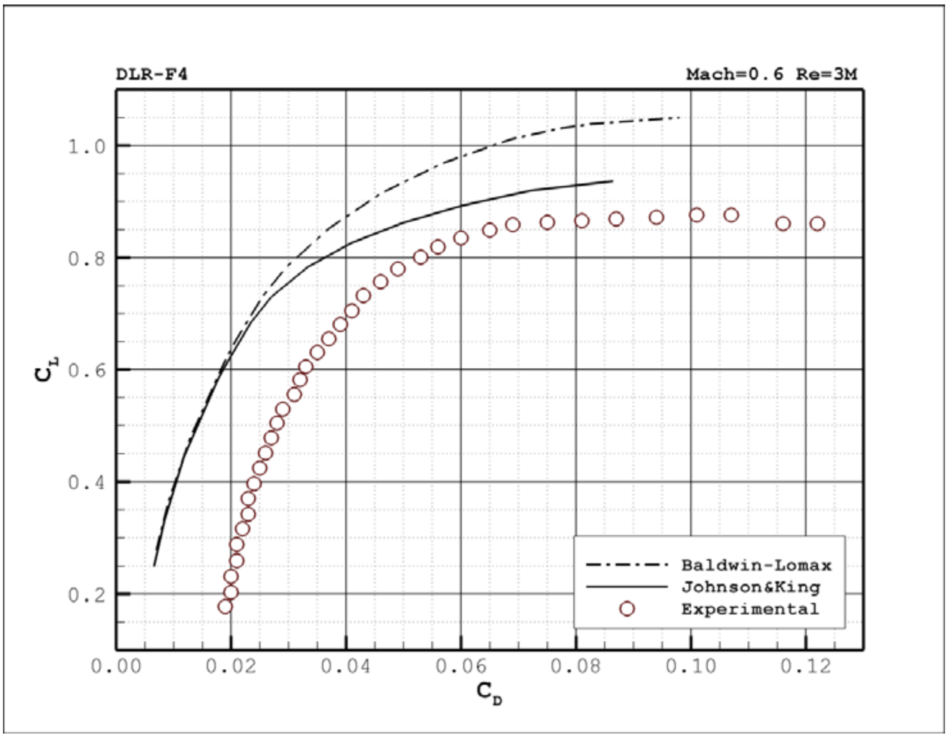

Figure 3-36 Drag Polar (M=0.60)

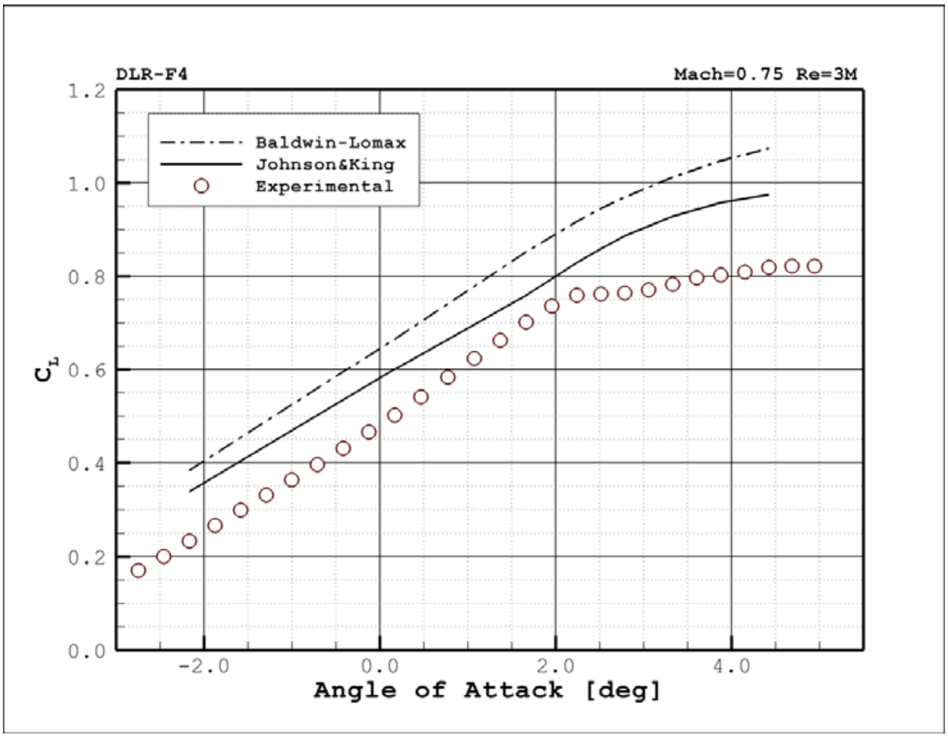

Figure 3-37 Lift Curve (M=0.75)

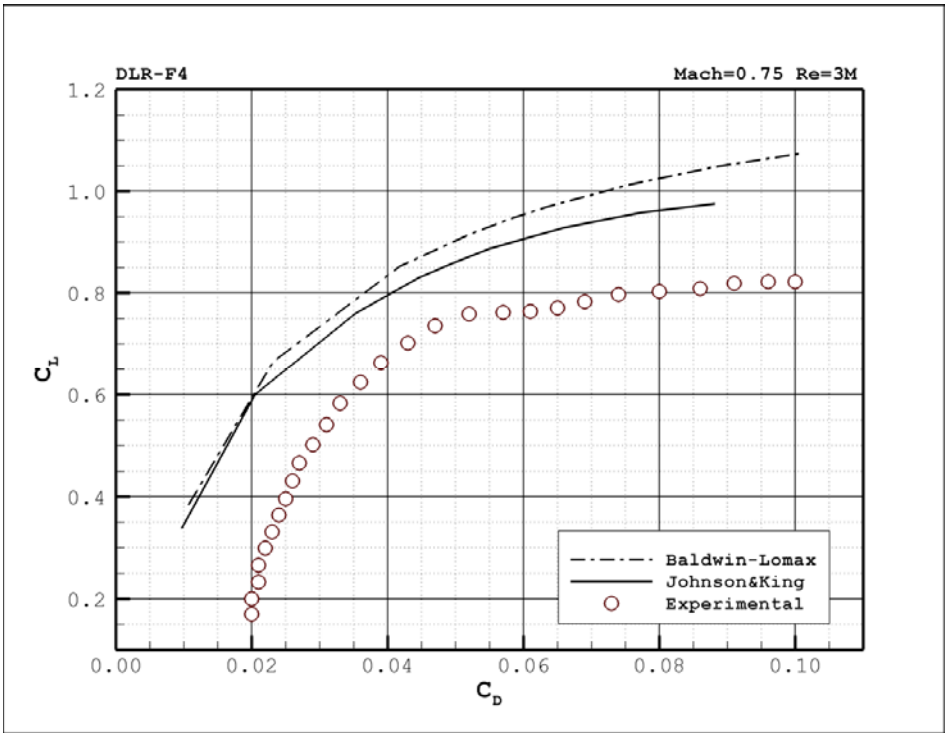

Figure 3-38 Drag Polar (M=0.75)

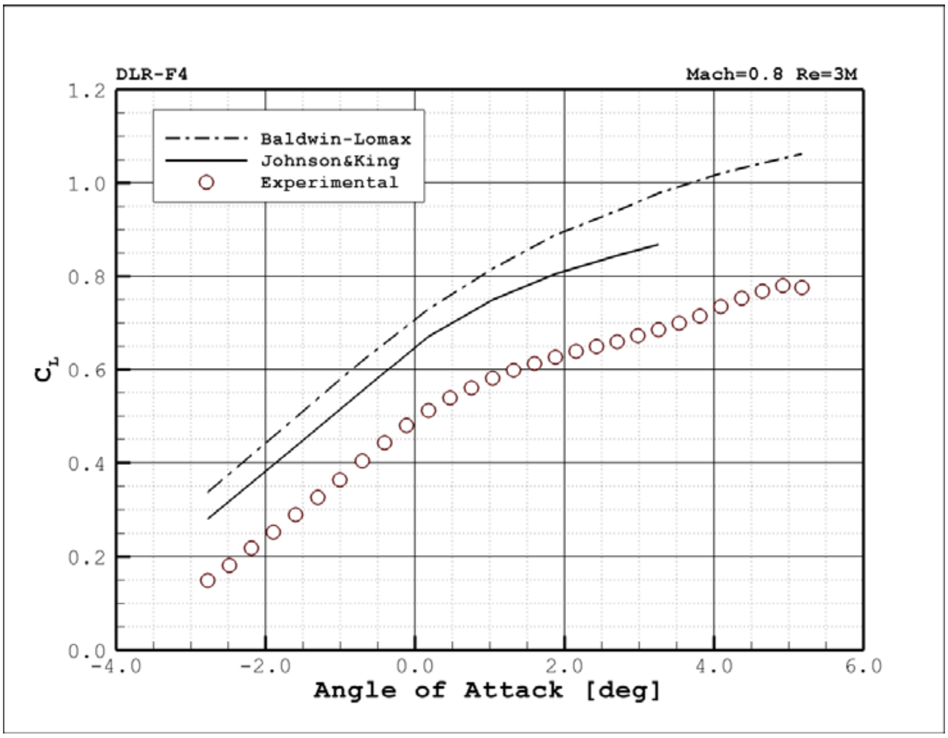

Figure 3-39 Lift Curve (M=0.80)

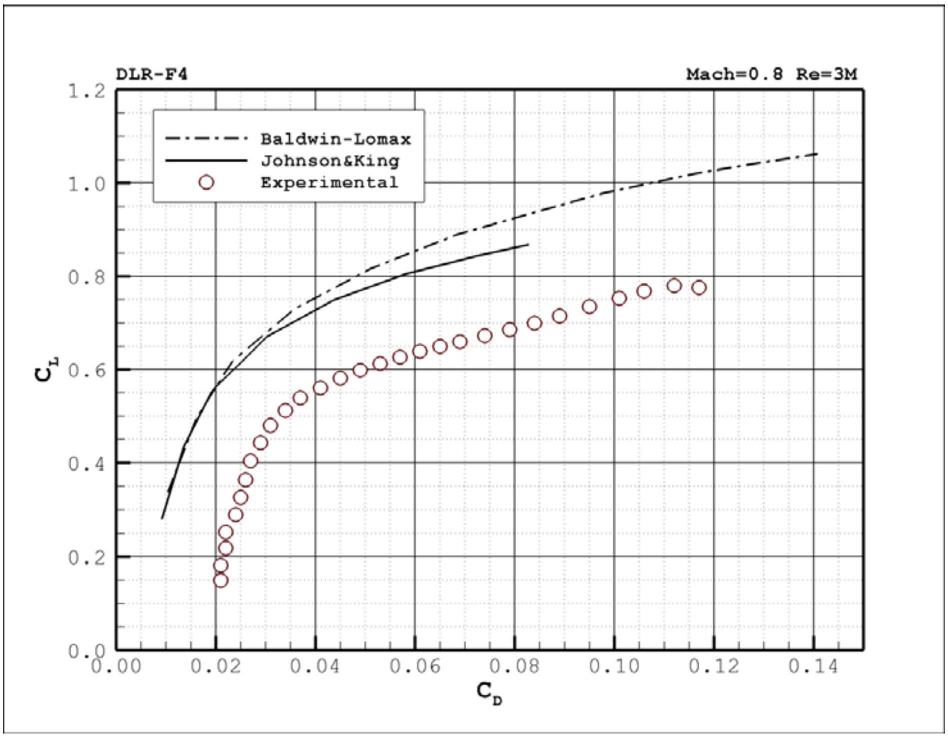

Figure 3-40 Drag Polar (M=0.80)

The numerical surface pressure distribution data obtained at flow conditions of Mach number is equal to 0.60, and the angle of attack is equal to 0.641 degrees are compared with the results obtained from three different wind tunnels (Figure 3-41, 3-42, 3-43, 3-44, 3-45, and 3-46). There are six different spanwise sections, in which the pressure distribution is investigated. The overall correlation between the viscous CFD results and wind-tunnel measurements is reasonable. Inboard of the wing, the suction peak predictions near the leading edge are very good, contrary to outboard of the wing, where the suction peak is slightly missed.

Since the measured surface pressure coefficients are quite good predicted by BL and JK turbulence models, the integrated quantities like lift and drag should be in good agreement with the experimental data. The idea mentioned above about the wing-body interactions, which produce the lower lift coefficient and the higher drag coefficient for the wind tunnel measurement when compared to computational results, can also be supported by obtaining such a good correlation with the experimental data over the wing surface.

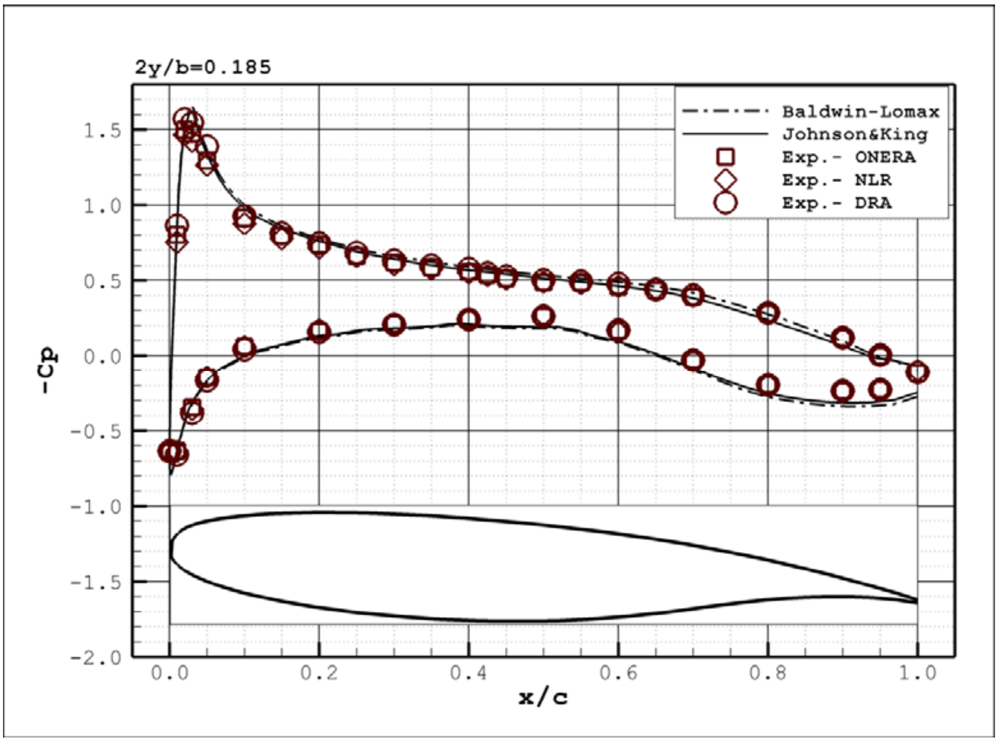

Figure 3-41 C_P distribution at M_∞ = 0.6 and α=1.0^o (at 2y/b=0.185)

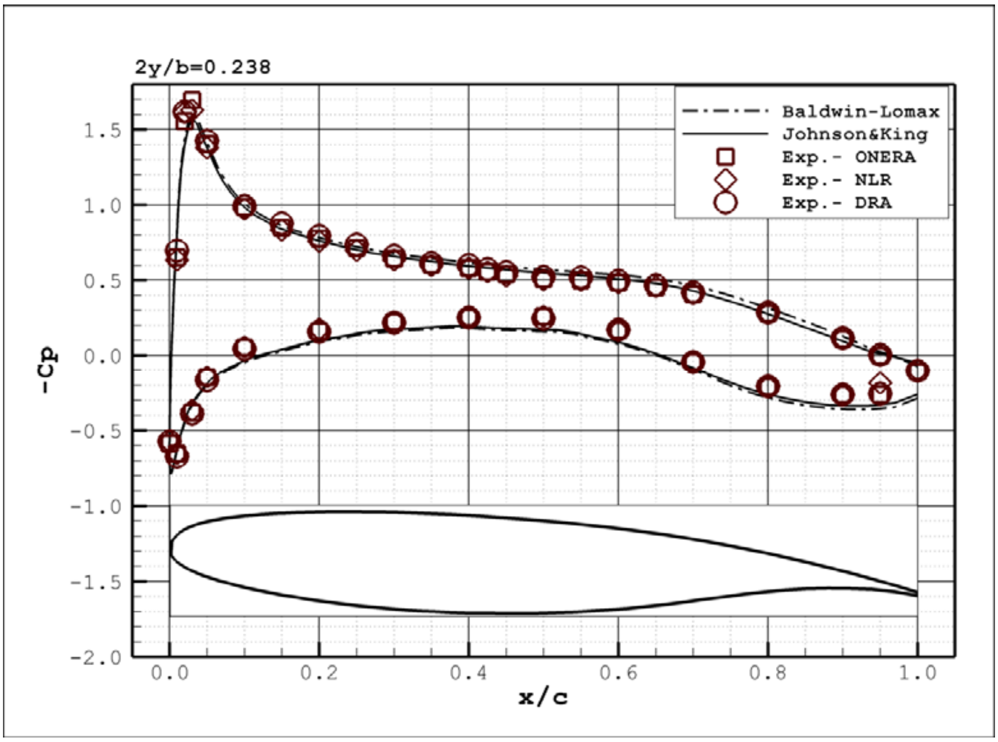

Figure 3-42 C_P distribution at M_∞ = 0.6 and α=1.0^o (at 2y/b=0.238)

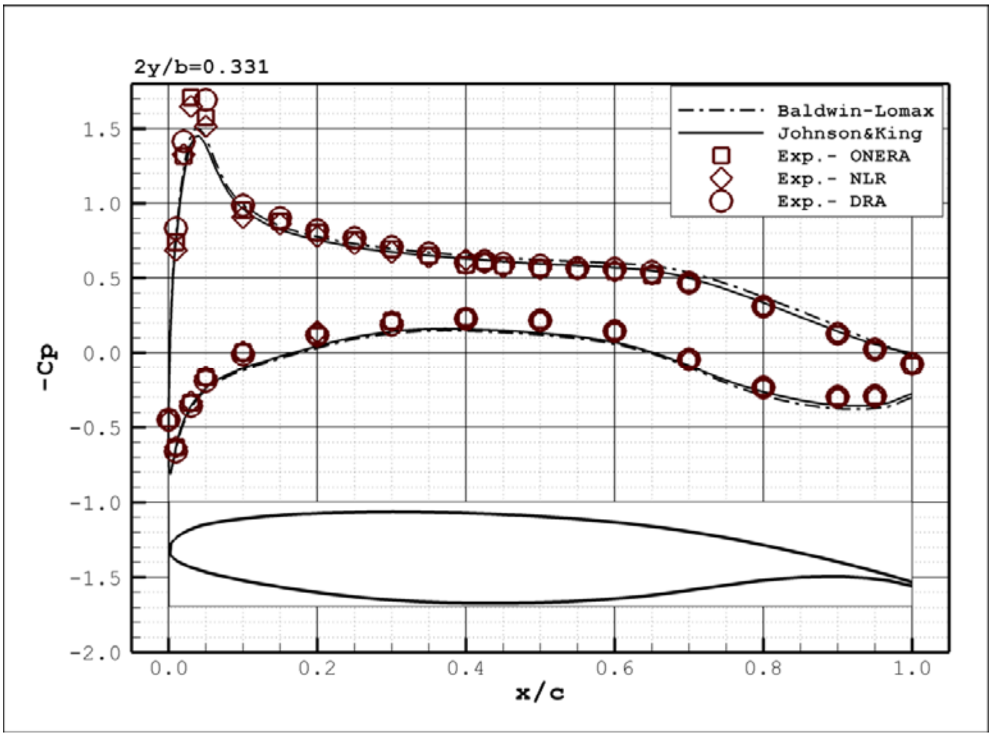

Figure 3-43 C_P distribution at M_∞ = 0.6 and α=1.0^o (at 2y/b=0.331)

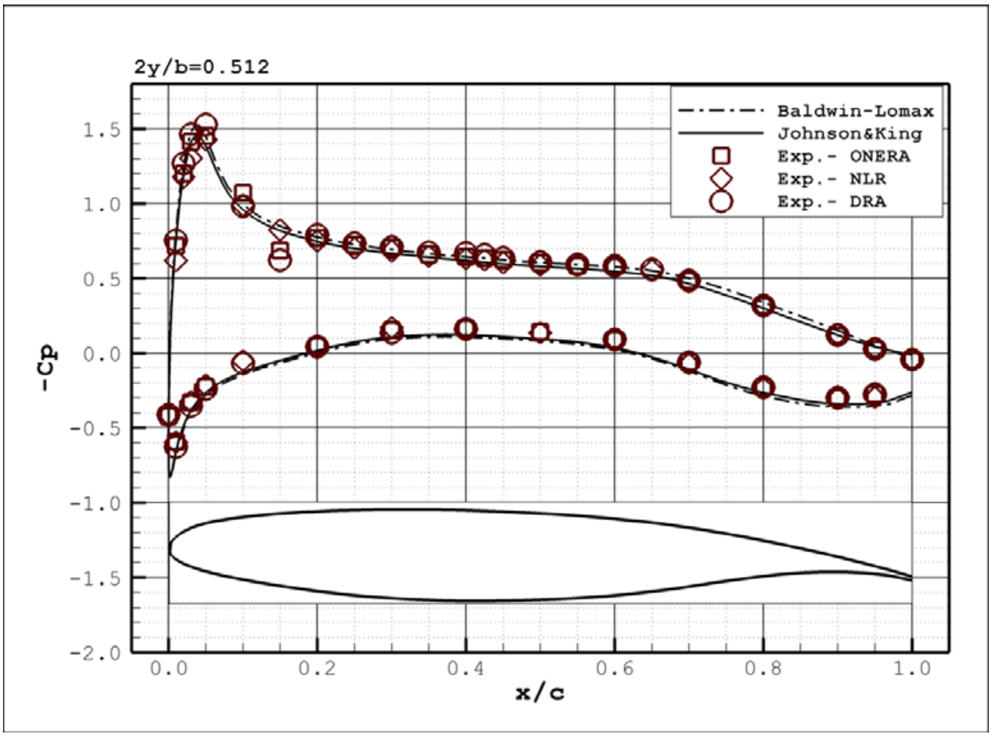

Figure 3-44 C_P distribution at M_∞ = 0.6 and α=1.0^o (at 2y/b=0.512)

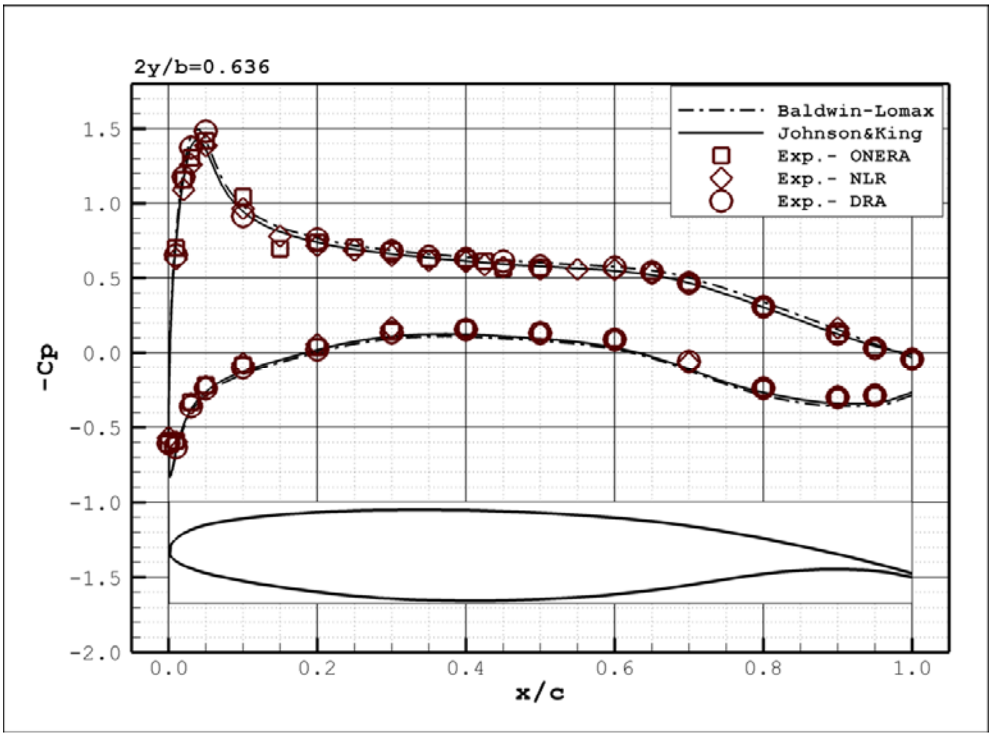

Figure 3-45 C_P distribution at M_∞ = 0.6 and α=1.0^o (at 2y/b=0.636)

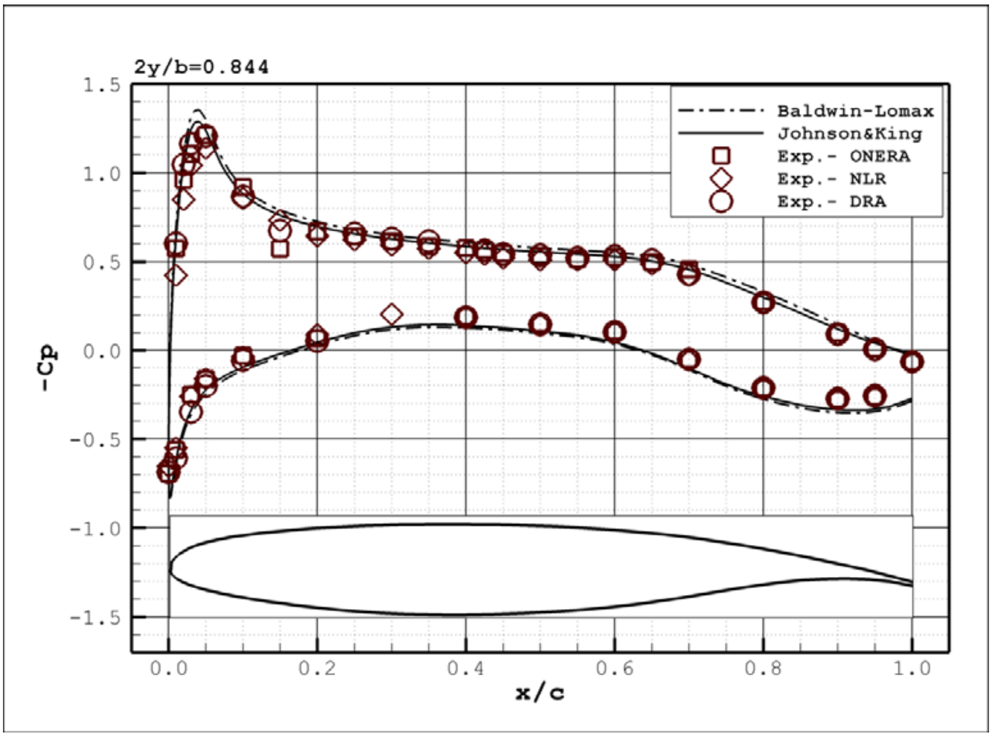

Figure 3-46 C_P distribution at M_∞ = 0.6 and α=1.0^o (at 2y/b=0.844)

The issues of affordability and time to market are driving the industry to greater reliance on computational tools in the design process. Utility of CFD is related to reliability of the solution process. The credibility and confidence in the tool can be provided via the process of verification and validation. Also, this process allows quantifying uncertainty and error. Up to now, computational results are compared against wind tunnel measurements. In the next test case, the results will be compared with well known CFD codes, including CFL3D and OVERFLOW (from Boeing), TAU-FLOWer (from DLR), FUN3D (from NASA), NSU3D (from University of Wyoming, Dimitri Mavriplis) and the commercial code FLUENT.

3.5 Test Case IV: DPW3 – WING 1/WING 2

These test cases were selected from the 3rd AIAA CFD Drag Prediction Workshop [7]. One of the objectives of this workshop is to provide an impartial forum for evaluating the effectiveness of existing Navier-Stokes flow solvers. Since this workshop is on ‘blind’ drag prediction accuracy, there is no prior experimental data for comparison. However, there is an opportunity to compare the results with well-known CFD codes. This test case provides a convenient way to distinguish the differences between the flow solvers.

Wing-1 is the baseline geometry and Wing-2 was created using simple optimization to change camber and twist. CAD models were downloaded from the workshop homepage [7]. DPW – WING 1 and WING 2 have an aspect ratio of 4 and the taper ratio is 0.5. The leading edge sweep angle is 17.2 degrees and the quarter chord sweep is 15 degrees [7]. The eight spanwise stations, in which the surface pressure distribution was investigated, are as shown in Figure 3-47.

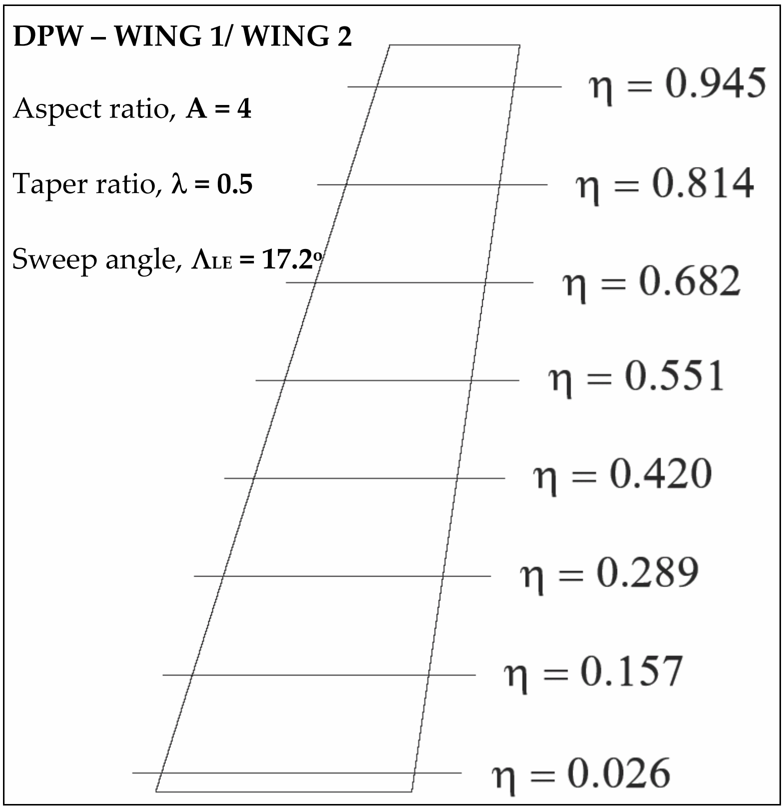

Figure 3-47 Geometric layout of the DPW – WING 1/ WING 2

The computations were performed at the flow conditions of Mach number is equal to 0.76, the range of angle of attack from -1 degrees to +3 degrees by the increment of 0.5 degrees, and the Reynolds number is 5 millions based on reference chord length.

The employed grids are C-H type having 193x65x49 nodes in the stream wise, spanwise and the normal directions respectively. In Figure 3-48, the mesh around the WING-1 is represented. Since the WING-1 and WING-2 are similar in all aspects except the camber and twist, the grid around the WING-2 is not shown.

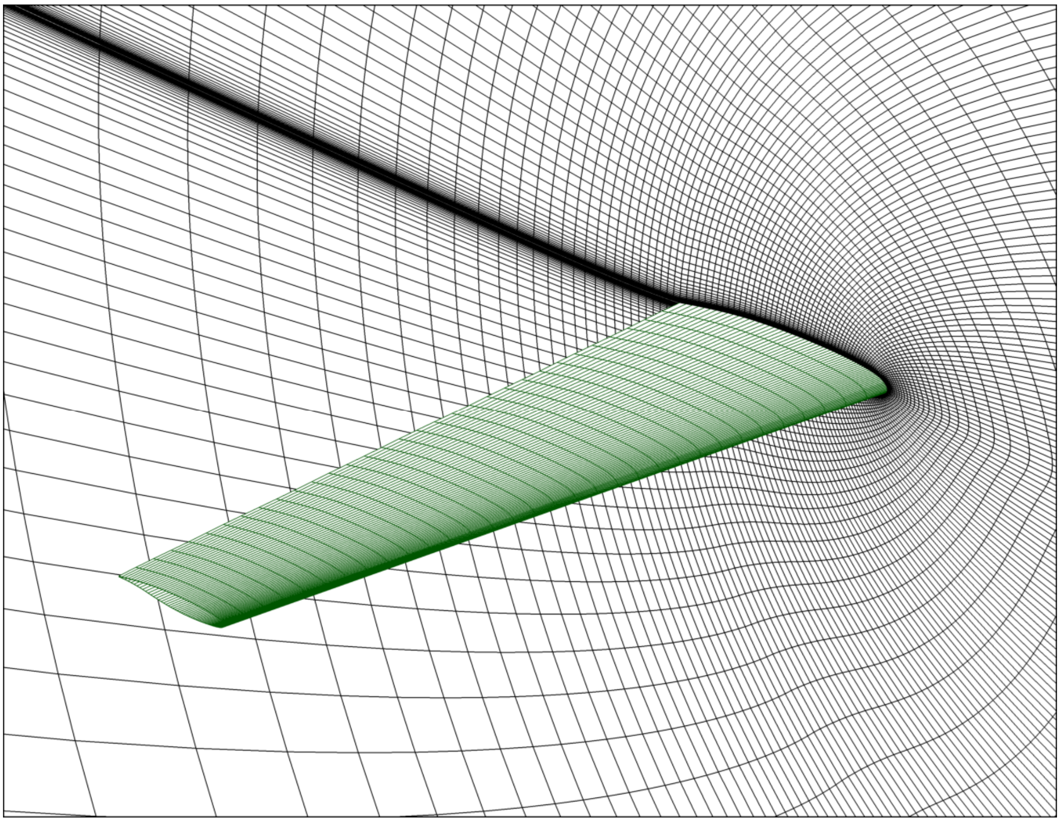

Figure 3-48 Mesh around the DPW – WING 1

The convergence characteristics are as given in Figure 3-49 and Figure 3-50 for the design flow condition (M_∞=0.76 and α=0.5 degrees) with the log of the residual and force coefficients. The 3-levels of multigrid was used and the number of iterations for each sequence is 1000. The residual dropped more than 5 orders of magnitude. Each solution took just about 4.5 hours (wall time) on PC.

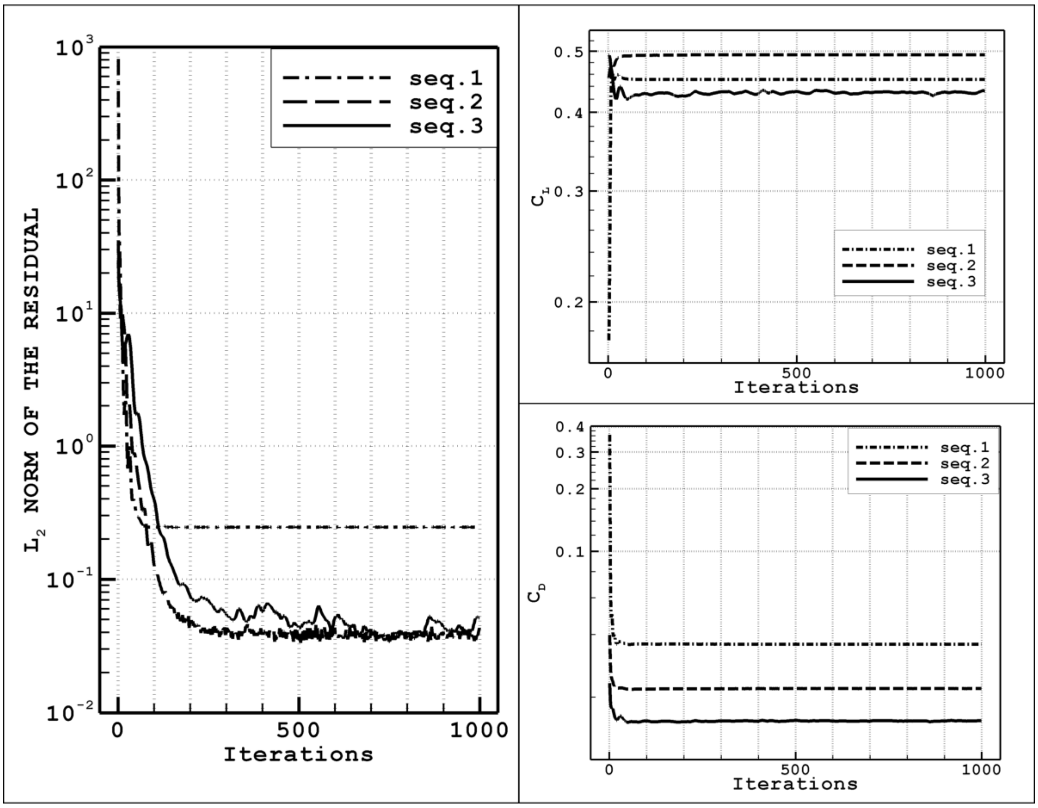

Figure 3-49 Convergence Histories of DPW – WING 1 (M_∞=0.76, α=0.5^o)

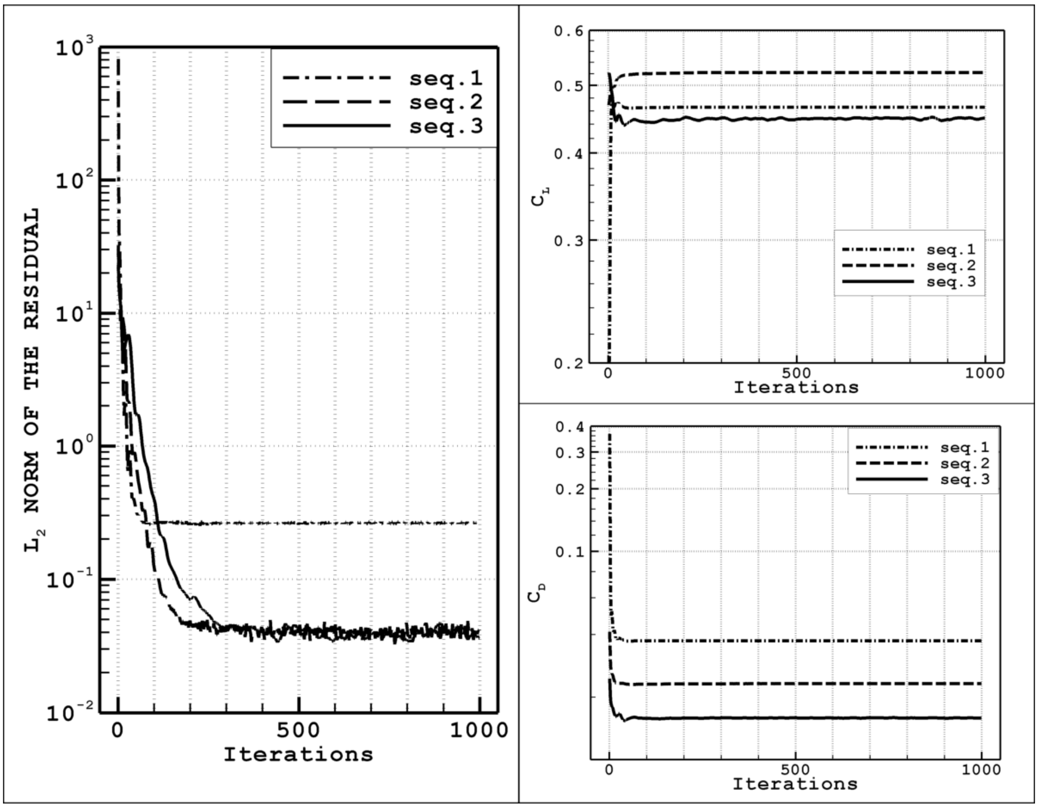

Figure 3-50 Convergence Histories of DPW – WING 2 (M_∞=0.76, α=0.5^o)

Next two figures (Figure 3-51, 3-52) show pressure contours and streamlines on the W1 and W2. The BL results are represented on the left column, while the results of the JK model are on the right column. Hence, these turbulence model solutions can be compared for each angle of attack value. The separation starts at around α=1.5^o. At first glance, WING 2 results seem to be the same for WING 1. However, JK model predicts that the separation is in the middle part of the wing but, this separation occurs close to the outboard for the BL case. At the highest angle of attack (3.0 deg.), BL turbulence model captures a secondary separation close to the wing root. For the same alpha the JK model, predicts slightly wider separation, but there is no other secondary separation. In WING 2 results, the differences between the turbulence models are significant.

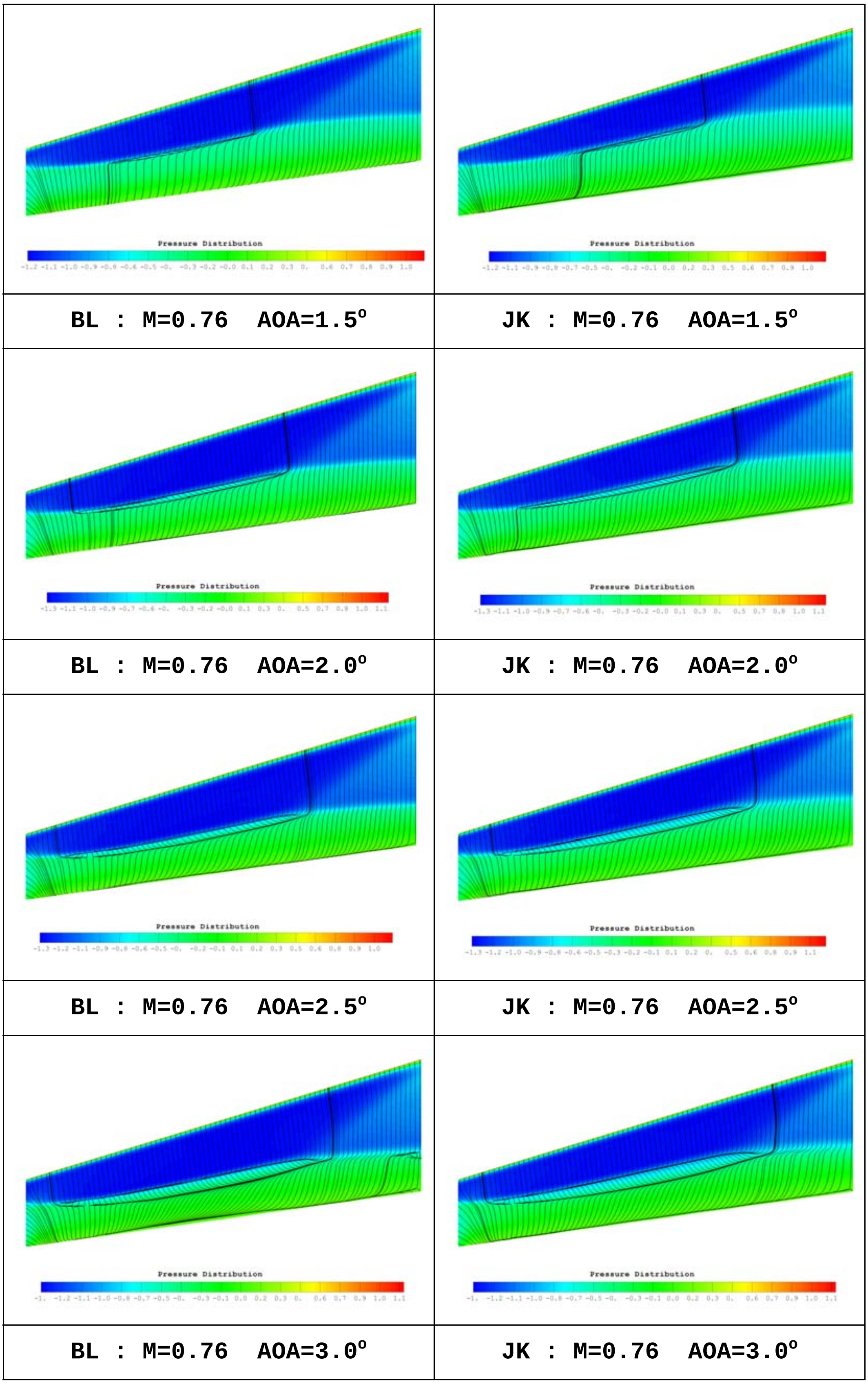

Figure 3-51 “Oilflow” patterns over DPW – WING 1 (BL & JK Solutions)

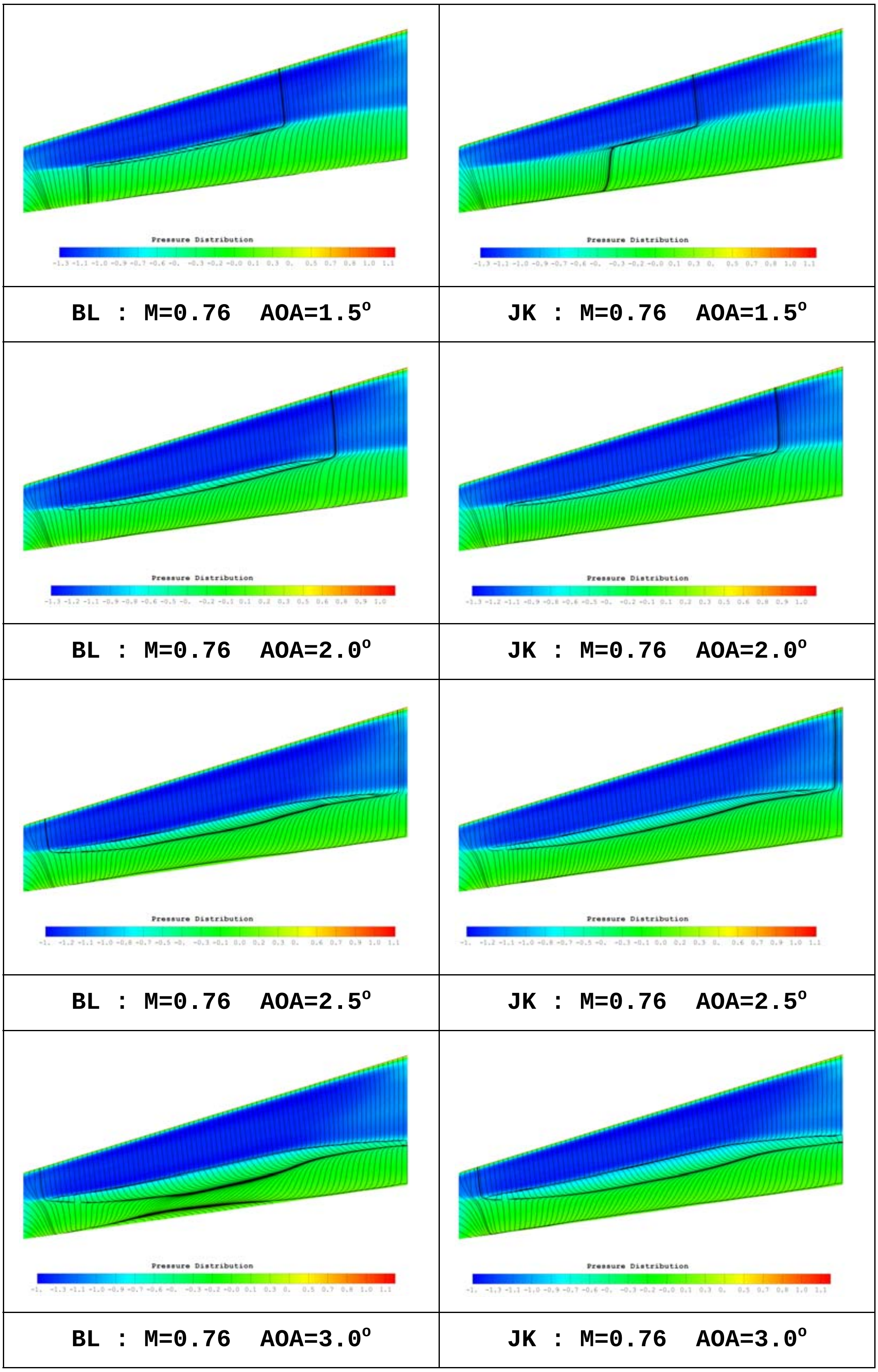

Figure 3-52 “Oilflow” patterns over DPW – WING 2 (BL & JK Solutions)

Since W1 and W2 test cases do not have the measured wind tunnel data, the comparisons will be done using the well known CFD codes. Main information regarding these flow solvers are tabulated in Table 1. OVERFLOW (Boeing) uses structured grid on full Navier Stokes (NS) and the turbulence model is Spalart-Allmaras (SA). CFL3D (Boeing) is a structured thin layer NS code with SA and the Menter's k-ω SST models. TAU (DLR) is unstructured Reynolds Averaged Navier-Stokes (RANS) solver with the Spalart-Allmaras Extended (SAE) Model and the Menter's k-ω SST Model (kw-SST). FLOWer (DLR) is the structured RANS solver and uses the Reynolds stress models: SST and SSG/LLR, in which the SSG is the quasi-nonlinear model of Speciale, Sarkar and Gatski, and LLR model is proposed by Launder, Reece and Rodi. FUN3D (NASA Langley Research Center) is an unstructured full NS code having SA and SST turbulence models. NSU3D is used by Dimitri Mavriplis (University of Wyoming) and it is an unstructured thin-layer RANS solver. For the test cases it uses original SA model. The last one is the FLUENT, which used unstructured grid generated by Boeing. Realizable k-ε (RKE) turbulence model was used by FLUENT. Approximate grid sizes used in these flow solvers are around 10 millions points, which makes 10 times finer mesh than the mesh used in this study.

Table 3-1 Participants of the DPW-W1 & W2

AFFILIATION		CODE	TYPE	TURBULENCE MODEL
	TAI	xFLOW	Structured, Full NS	BL, JK
	THE BOEING COMPANY	OVERFLOW	Structured, Full NS	SA
		CFL3D	Structured, Thin Layer NS	SA & Menter's k-ω SST
	DLR	TAU	Unstructured, RANS	SAE & Menter's k-ω SST
		FLOWer	Structured, RANS	SST & SSG/LLR
	NASA LANGLEY RESEARCH CENTER	FUN3D	Unstructured, Full NS	SA & SST
UNIVERSITY OF WYOMING		NSU3D	Unstructured, Thin Layer NS	SA
	FLUENT INC.	FLUENT 6.3	Unstructured	Relizable k-ε

In the following figures (Figure 3-53, 3-54, 3-55, and 3-56), the aerodynamic characteristics of the wings are compared with the results of the Drag Prediction Workshop. Although it is difficult to judge quality of results without any experimental "guide" solutions, the following lift/drag figures indicate that most of the represented CFD tools are in reasonable agreement with each other.

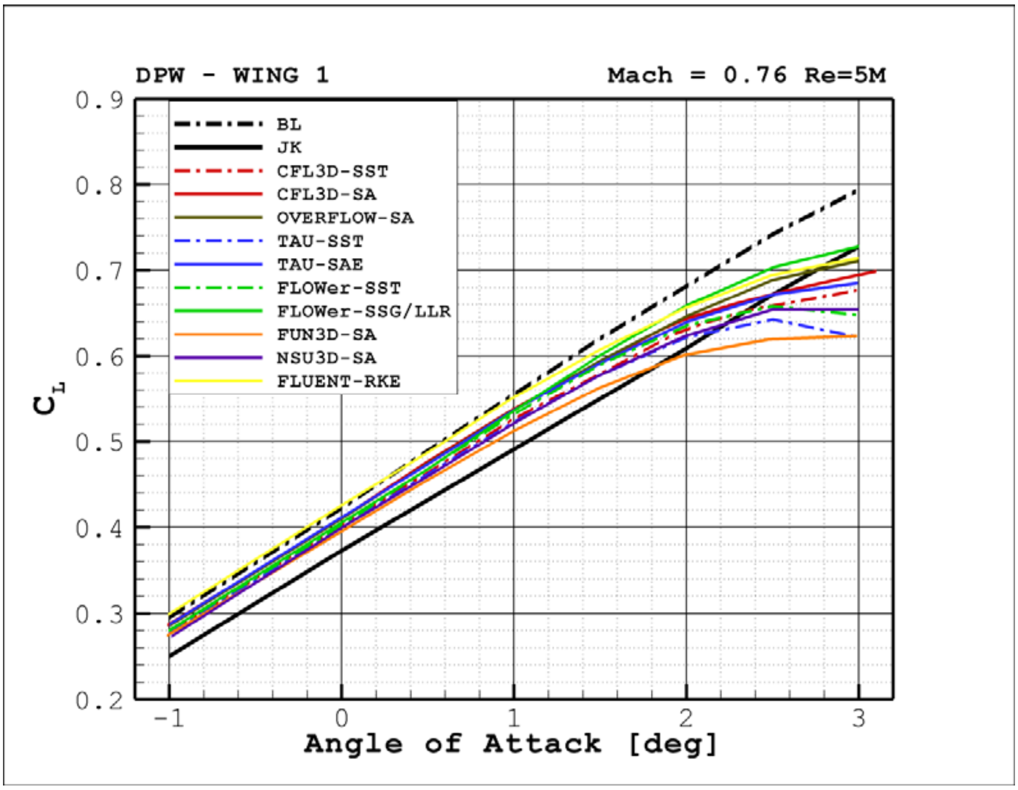

Figure 3-53 Lift Curve for WING 1 (M=0.76, Re=5M)

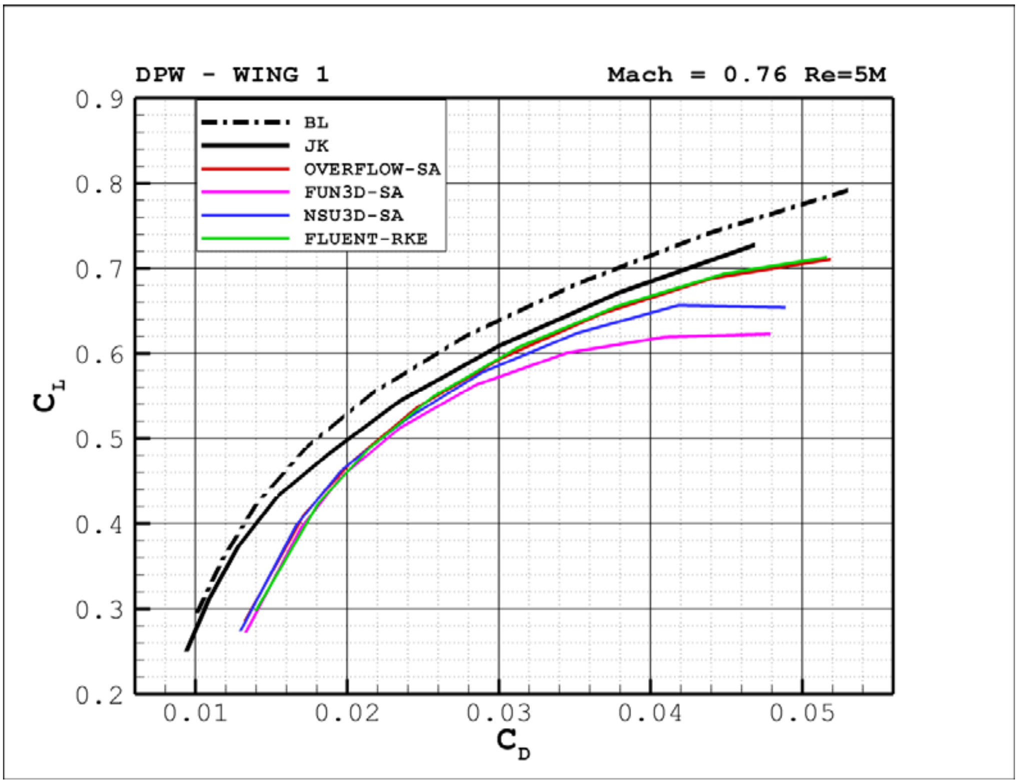

Figure 3-54 Drag Polar for WING 1 (M=0.76, Re=5M)

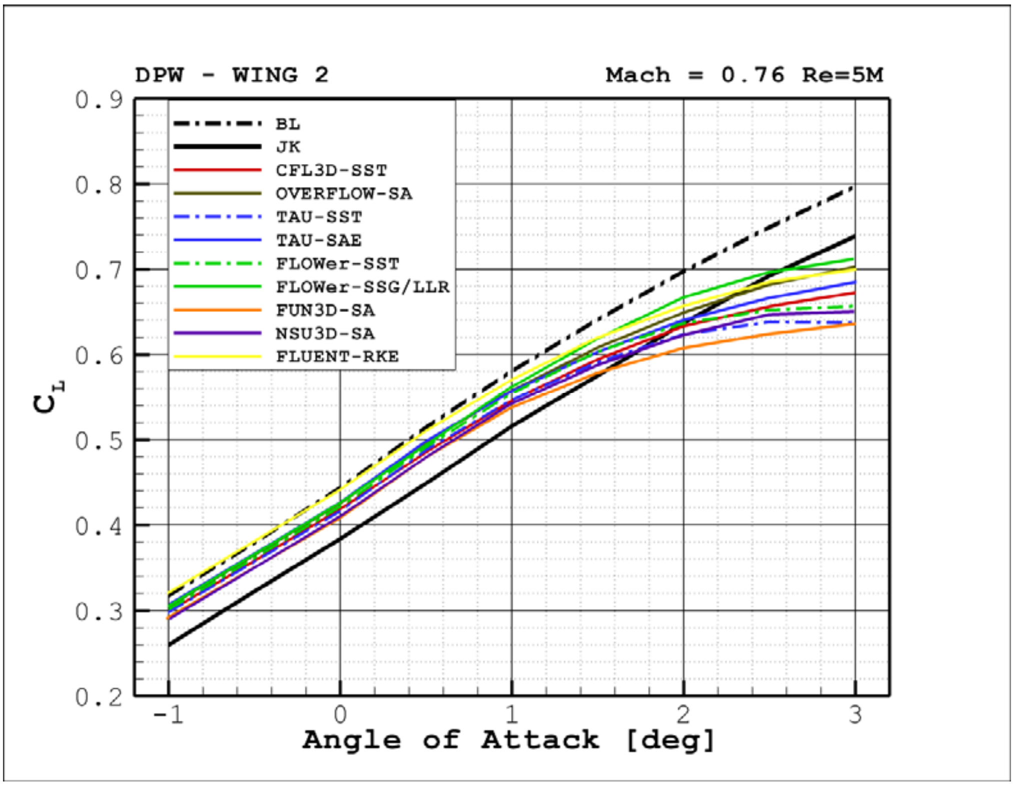

Figure 3-55 Lift Curve for WING 2 (M=0.76, Re=5M)

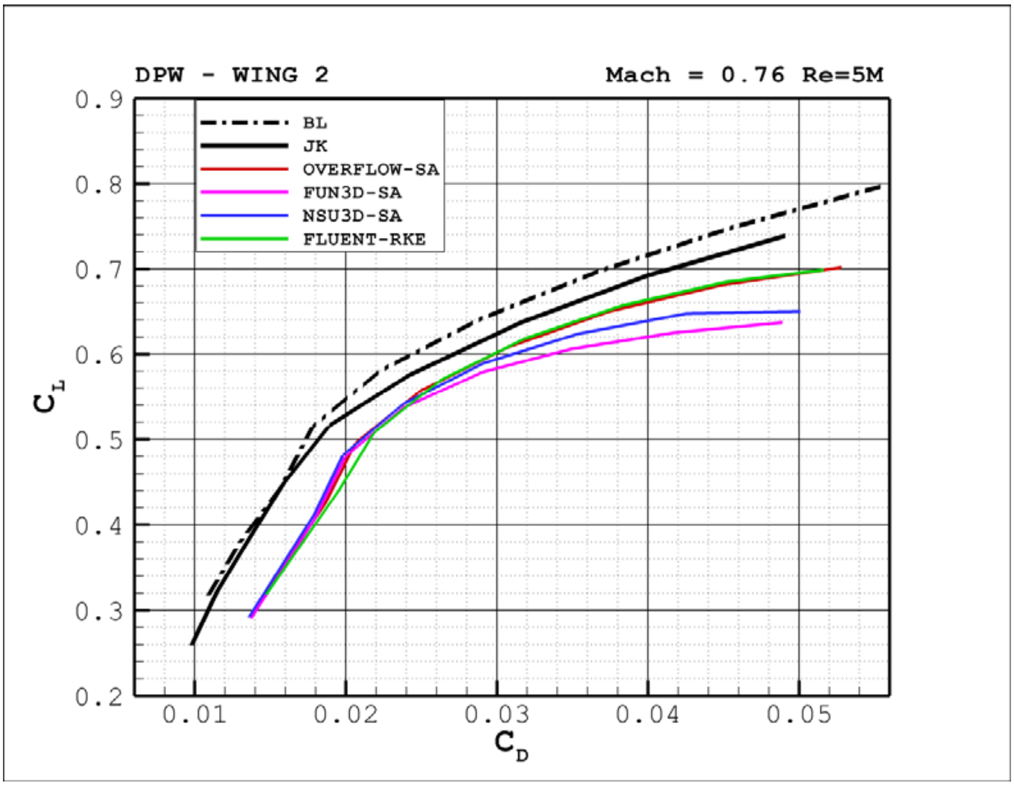

Figure 3-56 Drag Polar for WING 2 (M=0.76, Re=5M)

The BL model exhibits relatively higher lift and lower drag coefficients. On the other hand, the JK model predicts the lowest C_L than any other methods. In general, the lift and drag trends are well presented for these turbulence models, but there is a discrepancy at high angles of attack. This is a blind study and the unavailability of experimental data does not allow commenting on absolute accuracy. But it can be said that, on the basis of comparison with other CFD codes, good accuracy has been presented when considered the relative grid sizes, and computing time.

The surface pressures were investigated at eight different span wise sections. These comparisons were done at the flow condition of Mach number is 0.76, the angle of attack is 0.5 degrees and the Reynolds number is 5 millions. The C_P distribution of WING 1 is given in Figure 3-57 and 3-58.

The results of the BL model are well correlated with the other computational solutions. Especially it is very close to the CFL3D results, which uses the Spalart-Allmaras turbulence model. Furthermore, FUN3D, which is used at the NASA Langley Research Center and these solutions were obtained by using the SA model, captured the shock wave upstream when compared to others (except in the middle station-0.42%). All CFD tools agree reasonable well with regard to the shock placement. There is upstream shift of shock location for the JK model. Only at outer station (94.5%), the JK model shows good agreement. Besides, the JK model shows much more smearing of the shock at the inboard of the wing (from 2.6% to 15.7%).

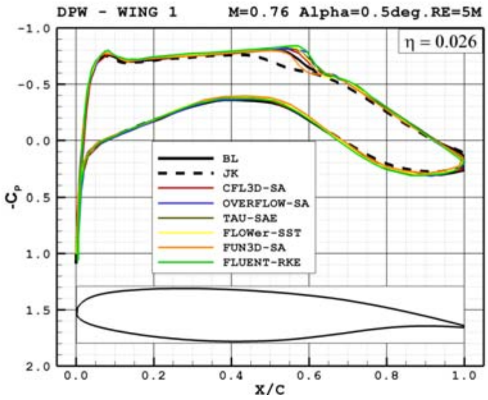

η=0.026

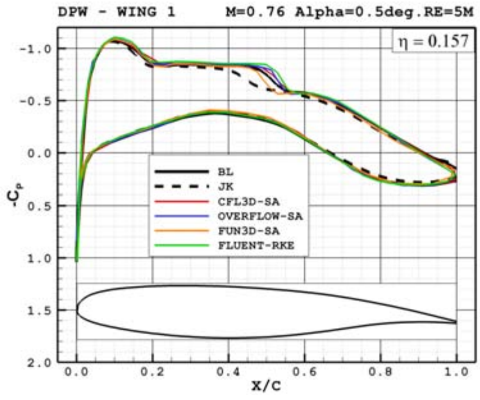

η=0. 157

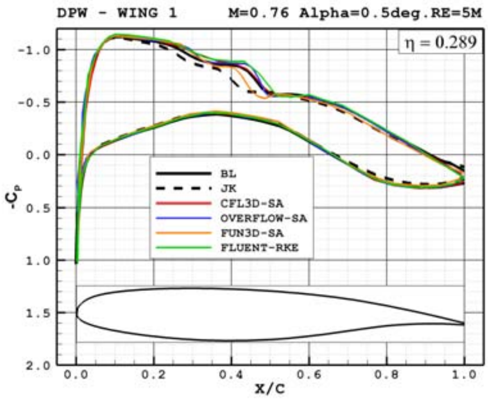

η=0. 289

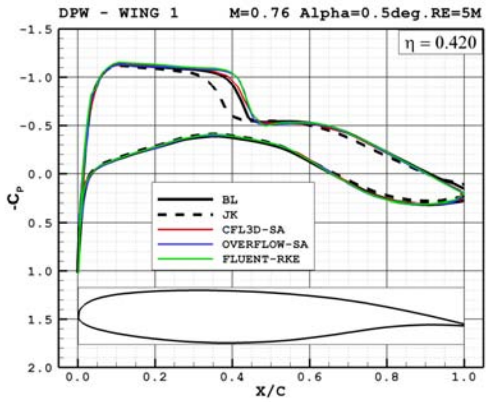

η=0.420

Figure 3-57 C_P distribution of WING 1 (M_∞ = 0.76, α=0.5^o) (continued)

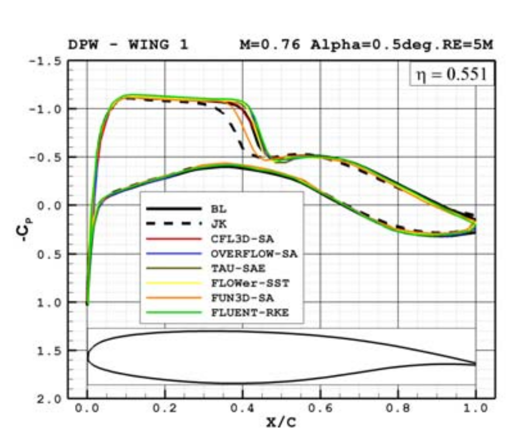	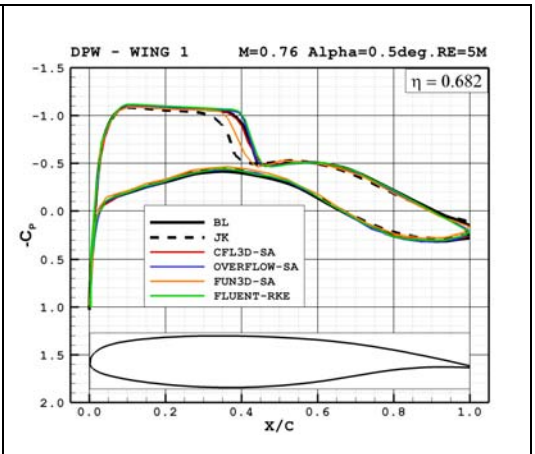
η=0.551	**η=0. 682**
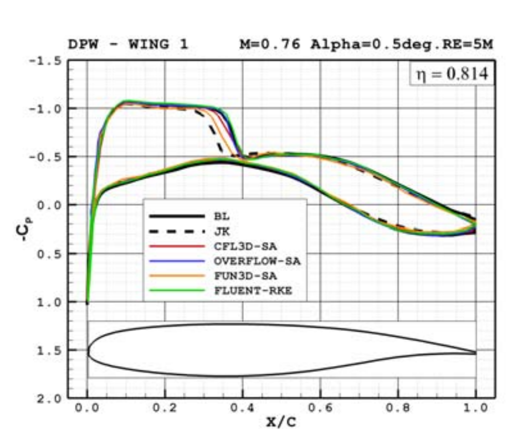	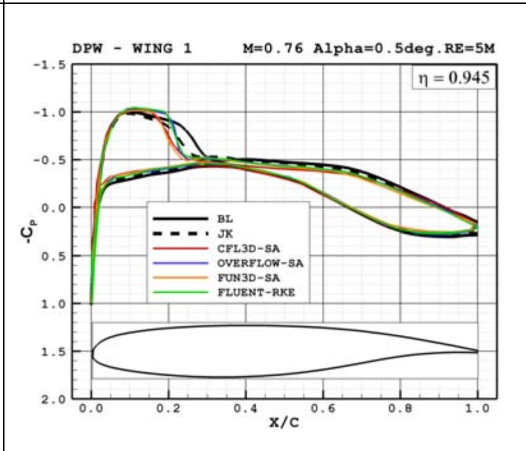
η=0. 814	**η=0.945**

Figure 3-58 C_P distribution of WING 1 (M_∞ = 0.76, α=0.5^o)

As it was mentioned before, WING 1 is the baseline wing, and WING 2 is obtained from this wing via simple optimization. Only the camber and twist parameters were changed. When the results shown in figures from Figure 3-57 to Figure 3-60 are compared, it is observed that there is a strong shock on WING 1, which is started around 42% of the wing. However, there is no strong shock on WING 2. The only weak shock was predicted by the JK model. Besides, at stations 55.1%, 81.4%, and 68.2% FUN3D tend to predict the shock placement in front of the other results.

The comparison of the Baldwin-Lomax turbulence model against these well-known CFD codes is in good agreement at almost every spanwise station except the last one (94.5%).

The results obtained from the Navier-Stokes flow solver with the Baldwin-Lomax turbulence model are robust and gives reasonable results, even if the quality of the grid is questionable.

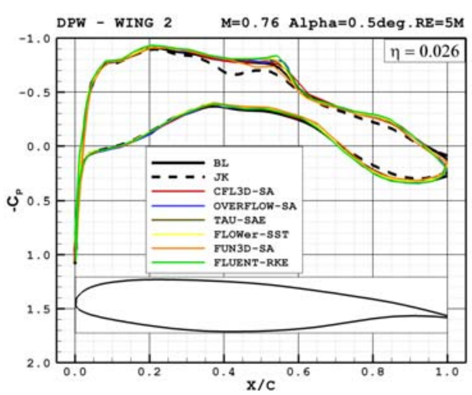

η=0.026

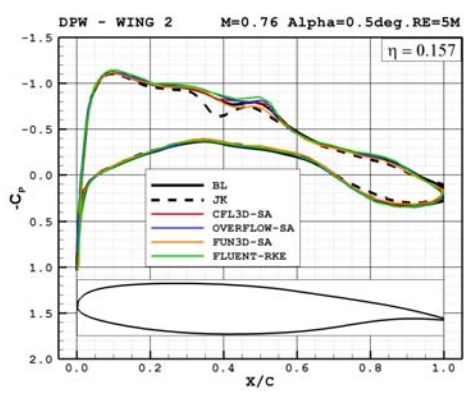

η=0. 157

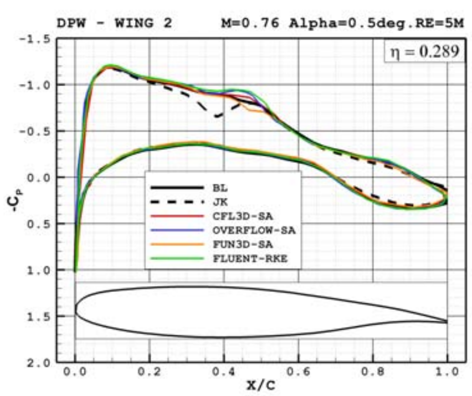

η=0. 289

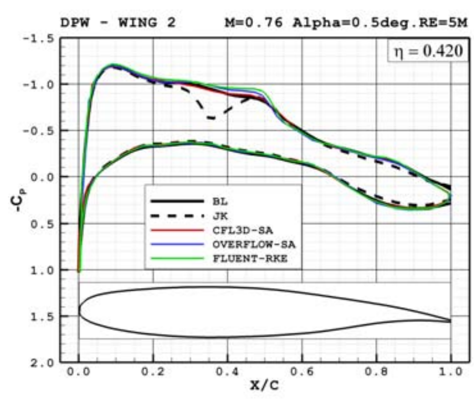

η=0.420

Figure 3-59 C_P distribution of WING 2 (M_∞ = 0.76, α=0.5^o) (continued)

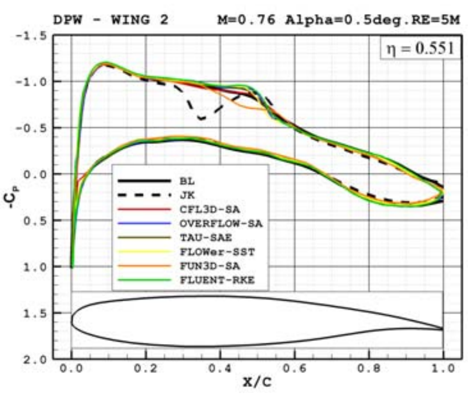

η=0.551

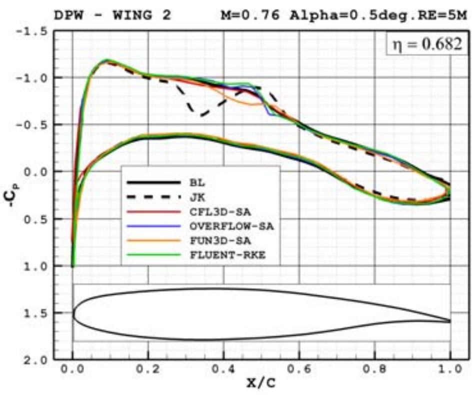

η=0. 682

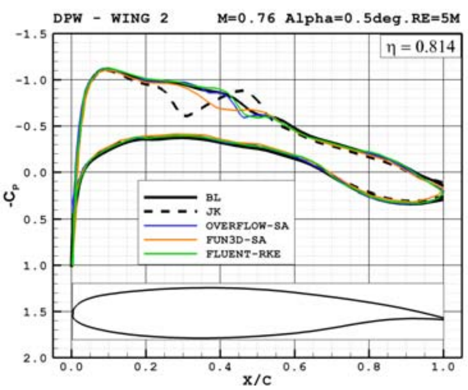

η=0. 814

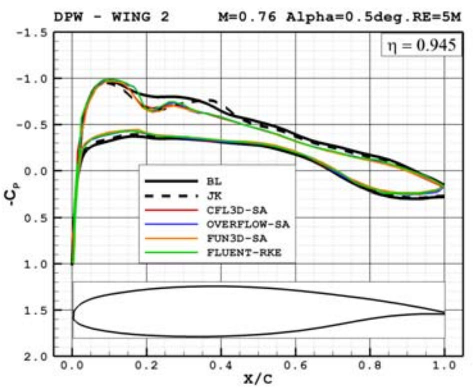

η=0.945

Figure 3-60 C_P distribution of WING 2 (M_∞ = 0.76, α=0.5^o)

CHAPTER 4

CONCLUSION

The purpose of this study is the implementation of the Johnson-King Turbulence model algorithm into Navier-Stokes flow solver and the validation/verification of this CFD tool on swept wings. The Baldwin-Lomax turbulence model was already available in the flow solver, and it was used as a base solver for this newly implemented model. This CFD tool is aimed to be used as a practical analysis tool, in terms of accuracy and robustness.

The validation/verification was carried out using two- and three-dimensional test cases. NACA 0012 airfoil, ONERA M6 wing, DLR-F4 wing and DPW3 – Wing1/Wing2 were selected as test cases. Both of the turbulence models and also Euler solution were compared against experimental and reference data. Initial analysis was performed on simplest test case, which is NACA 0012, at transonic speeds. The flow field was captured very accurately for viscous computations.

This work continued on the flow analysis over swept wings. The flow over ONERA M6 wing with Mach number of 0.84 and angles of attack 5.06/6.06 degrees were computed. In order to investigate how accurately the flow field computation can be performed using viscous and inviscid methods, the surface pressure coefficients were compared against the experimental data at various spanwise stations. The following test case was DLR-F4 wing, which had a higher aspect ratio than the ONERA M6 wing. For this case, the experimental data set includes the aerodynamic performance characteristics and the surface pressure distributions at different sections. The final test cases are named as Wing1 and Wing2, which are taken from the 3rd AIAA Drag Prediction Workshop. This case provides an opportunity to realize the level of our in-house developed code among the other widely known CFD codes.

It is noteworthy to point out that the results of the BL and JK models, which were demonstrated in the previous Chapter, are quite satisfactory. Although meshes were rather coarse, the significant flow features were predicted. On balance, JK model appears to be a useful engineering analysis tool, within its targeted range of applicability, which is flow with mild separation.

The code is being converted to a parallel, multi-block oversetting grid flow solver to run on a network of personal computers, for the analysis of complex geometries in feasible durations acceptable for engineering development schedules.

As a future work, this code can be used as a base flow solver and many more turbulence models can be implemented in it. In this way, these models can also be tested using the same grid on the same flow solver.

REFERENCES

[1] Schmitt, V., Charpin, F., *Pressure Distributions on the ONERA M6 Wing at Transonic Mach Numbers*, AGARD AR-138, Part B1, 1979.

[2] Abid, R., Vatsa, V.N., Johnson, D.A., Wedan, B.W., *Prediction of Separated Transonic Wings*, AIAA 86-1052, Reno, NV, 1986.

[3] Vatsa, V.N., *Accurate Solutions for Transonic Viscous Flow Over Finite Wings*, AIAA-86-1052, Atlanta, GA, 1986.

[4] Marx, Y.P., *A Practical Implementation of Turbulence Models for the Computation of Three-Dimensional Separated Flows*, International Journal for Numerical Methods in Fluids, Vol.13, pp 775-796, 1991.

[5] Harris, C.D., *Two-Dimensional Aerodynamic Characteristics of the NACA 0012 Airfoil in the Langley 8-Foot Pressure Tunnel*, NASA-TM-81927, April 1981.

[6] Redeker, G., *DLR-F4 Wing Body Configuration*, AGARD-AR-303, Vol.II, August 1994.

[7] AIAA, *3rd AIAA CFD Drag Prediction Workshop, http://aaac.larc.nasa.gov/tsab/cfdlarc/aiaa-dpw/index.html*, last access on; 12.09.2006.

[8] Jameson, A., *Analysis and Design of Numerical Schemes for Gas Dynamics 1: Artificial Diffusion, Upwind Biasing, Limiters and Their Effect on Accuracy and Multigrid Convergence*, International Journal of Computational Fluid Dynamics, Vol. 4, pp. 171-218, 1995.

[9] Swanson, R.C., Radespiel, R., Turkel, E., *On Some Numerical Dissipation Schemes*, Journal of Computational Physics, 147:518-544, 1998.

[10] Baldwin, B., Lomax, H., *Thin-Layer Approximation and Algebraic Model for Separated Turbulent Flows*, AIAA 78-257, January 1978.

[11] Abid, R., Vatsa, V.N., Johnson, D.A., Wedan, B.W., *Prediction of Separated Transonic Wing Flows with Nonequilibrium Algebraic Turbulence Model*, AIAA Journal Vol. 28, No. 8, pp. 1426-1431, August 1990.

[12] Hoffmann, K.A., Chiang, S.T., *Computational Fluid Dynamics: Volume III*, Engineering Education System, Fourth Edition, August 1990.

[13] Rumsey, C.L., Vatsa, V.N. *A Comparison of the Predictive Capabilities of Several Turbulence Models Using Upwind and Central Difference Computer Codes*, AIAA 93-0192, Reno, NV, 1993.

[14] Menter, F.R., Rumsey, C.L., *Assessment of Two-Equation Turbulence Models For Transonic Flows*, AIAA 94-2343, Colorado Springs, CO, 1994.

[15] Pope, S.B., *Turbulent Flows*, Cambridge University Press, 2000.

[16] Abid, R., *Extension of the Johnson-King Turbulence Model to the 3-D Flows*, AIAA Paper 87-0223, Jan.1988.